Evaporation of sessile droplets : hydrodynamics and salt deposit patterns

Cécile Lalanne

▶ **To cite this version:**

Cécile Lalanne. Evaporation of sessile droplets : hydrodynamics and salt deposit patterns. Fluid mechanics [physics.class-ph]. Sorbonne Université, 2022. English. NNT : 2022SORUS098 . tel-03771836

HAL Id: tel-03771836
https://theses.hal.science/tel-03771836

Submitted on 7 Sep 2022

HAL is a multi-disciplinary open access archive for the deposit and dissemination of scientific research documents, whether they are published or not. The documents may come from teaching and research institutions in France or abroad, or from public or private research centers.

L'archive ouverte pluridisciplinaire **HAL**, est destinée au dépôt et à la diffusion de documents scientifiques de niveau recherche, publiés ou non, émanant des établissements d'enseignement et de recherche français ou étrangers, des laboratoires publics ou privés.




Sorbonne Université

École doctorale Sciences Mécaniques, Acoustique, Électronique et Robotique

Thèse de doctorat

Spécialité Mécanique des Fluides

Evaporation of sessile droplets: hydrodynamics and salt deposit patterns

---

Par : **Cécile Lalanne**

Sous la direction de José-Maria Fullana, Professeur
Florence Lequien, Ingénieur-chercheur

à l'Institut Jean le Rond ∂'Alembert, Sorbonne Université, CNRS, UMR 7190
et au Laboratoire d'Étude de la Corrosion Non Aqueuse, CEA-Saclay.

Soutenue le 11 Mars 2022

Devant le jury composé de :

Stéphane Dorbolo	Rapporteur
Christophe Poulard	Rapporteur
Laurent Duchemin	Examinateur
Christophe Josserand	Examinateur
Elise Lorenceau	Examinatrice
José-Maria Fullana	Directeur de thèse
Florence Lequien	Co-encadrante de thèse

Abstract

Evaporation of sessile droplets: hydrodynamics and salt deposit patterns

In humid environments, the formation of sessile droplets containing pollutants, such as sodium chloride, on certain materials can lead to atmospheric corrosion phenomena. The prediction and understanding of these corrosion phenomena are closely linked to the dynamics of the droplet, and in particular to its evaporation. Ambient parameters such as relative humidity, temperature, substrate material as well as the composition of the droplet, e.g. its pollutant concentration, modify the evaporation dynamics and influence the characteristic time of corrosion. Salt deposits left after evaporation show complex hydrodynamics and indicate potential corrosion sites. Anticipating corrosion zones is crucial in many industrial applications to limit material degradation.

This study seeks to better understand the evaporation dynamics of sessile droplets, through parametric studies, with numerical simulations and experimental tests.
Pure water droplets are first considered, in order to simplify the studied system and to analyze the different modes.
Droplets of saline solution are studied in a second time. During evaporation, salt concentrates inhomogeneously inside the droplet causing surface tension gradients. These stresses along the interface, called Marangoni stresses, give rise to internal flows. Depending on the initial concentration of pollutant, the relative humidity, and the size of the droplet, the morphology of the resulting salt deposits is analyzed.

Keywords: Sessile droplet, evaporation, triple contact line, surface tension, salt deposit, sodium chloride.

Résumé

Évaporation de gouttes sessiles : hydrodynamique et morphologie des dépôts salins

Dans des environnements humides, la formation de gouttes sessiles contenant des polluants, comme le chlorure de sodium, sur certains matériaux peut conduire à des phénomènes de corrosion atmosphérique. La prédiction et la compréhension de ces phénomènes de corrosion sont étroitement liées à la dynamique de la goutte, et notamment à l'évaporation de celle-ci. Les paramètres ambiants comme l'humidité relative, la température, le matériau du substrat ainsi que la composition de la goutte, par exemple sa concentration en polluant, modifient la dynamique d'évaporation et influencent le temps caractéristique de la corrosion. Les dépôts laissés après évaporation témoignent d'une hydrodynamique complexe et indiquent les potentiels sites de corrosion. Anticiper les zones de corrosion se révèle crucial dans de nombreuses applications industrielles pour limiter la dégradation des matériaux.

Cette étude cherche à mieux comprendre la dynamique d'évaporation des gouttes sessiles, à travers des études paramétriques, avec des simulations numériques et des essais expérimentaux.
Des gouttes d'eau pure sont considérées dans un premier temps, afin de simplifier le système étudié et d'analyser les différents modes.
Des gouttes de solution saline sont étudiées dans un second temps. Lors de l'évaporation le sel se concentre de façon non homogène à l'intérieur de la goutte entraînant des gradients de tension de surface. Ces contraintes le long de l'interface, dites de Marangoni, donnent naissance à des écoulements internes. En fonction de la concentration initiale en polluant, de l'humidité relative, et de la taille de la goutte la morphologie des dépôts salins qui en résulte est analysée.

Keywords: Goutte sessile, évaporation, ligne de contact, tension de surface, dépôt salin, chlorure de sodium.

Remerciements

Tout d'abord, je voudrais remercier les membres de mon jury de thèse qui ont pris le temps de s'intéresser à mon travail. Merci à Elise Lorenceau d'avoir accepté de faire partie de mon jury de thèse. La discussion scientifique lors de la soutenance m'a permis d'analyser mon travail selon un autre point de vue et de pousser plus loin l'analyse chimique. Je tiens à remercier Christophe Josserand et Laurent Duchemin qui m'ont suivie tout au long de la thèse à l'occasion des comités de suivi. Vos conseils et remarques m'ont permis d'améliorer mon travail et d'investiguer différentes pistes de réflexion à propos des jolis problèmes physiques rencontrés pendant ma thèse. Merci à Christophe Poulard et Stéphane Dorbolo d'avoir accepté de rapporter ma thèse. Je vous remercie pour votre lecture attentive et enthousiaste du manuscrit, puis pour vos rapports détaillés.

Tout au long de la thèse, j'ai eu la chance d'être épaulée par deux encadrants Florence Lequien et José-Maria Fullana. Merci Florence de m'avoir fait découvrir la corrosion et l'electrochimie, des domaines que je ne connaissais pas au début de ma thèse : tu m'as permis d'élargir mon champ de connaissances en m'expliquant avec patience ces différents procédés et principes. Tu t'es montrée disponible et tu m'as permis d'améliorer ma communication scientifique en m'aidant à travailler sans relâche conférences et articles. José, dès la licence, tu as éveillé mon intérêt pour la mécanique des fluides et tu m'as ensuite fait confiance pour faire cette thèse avec toi. Tu m'as permis de sortir de ma zone de confort et tu m'as toujours encouragée à prendre des initiatives, à explorer différentes pistes de réflexion. Merci d'avoir été toujours présent pour discuter de science, de culture, de tout. Je suis souvent ressortie de nos réunions avec le sourire et un élan de motivation.

Je voudrais remercier l'ensemble des collègues avec qui j'ai pu interagir lors de ma thèse. Toutes les différentes interactions ont été enrichissantes et bienveillantes. Je tiens tout particulièrement à remercier Anca Belme avec qui j'ai eu le plaisir d'enseigner pendant 3 ans et qui m'a fait confiance pour encadrer avec elle des projets de L2 et L3. Depuis le début de ma thèse je tenais à réaliser une partie expérimentale afin de compléter le travail numérique. Cela a pu être possible notamment grâce à Anaelle Givaudan et Paul Boumendil, qui ont passé presque un an en stage avec moi. Votre bonne humeur et votre enthousiasme ont été une bouffée d'air frais dans la salle Savart et cela a été un vrai plaisir pour moi de vous transmettre mes connaissances en mécanique des fluides. Je vous souhaite le meilleur dans la suite de votre parcours.

Lors de la thèse j'ai eu la chance d'être entourée par de nombreux autres doctorants, post-doctorants et ATER qui ont contribué à créer un climat convivial et soutenant. Je les remercie tous vivement pour les bons moments passés ensemble ! Côté CEA, j'ai une pensée particulière pour Vinicius. Ton sens de l'écoute et ton soutien ont été d'une grande aide. Tu as été pour moi un véritable pilier et je te suis reconnaissante pour toutes les discussions

remotivantes que nous avons eues. A d'Alembert, j'ai eu la chance de me voir attribuer une place dans le bureau 317B où un accueil chaleureux m'a permis de me sentir rapidement à l'aise et inclue parmi les doctorants du labo. Pour toutes les discussions (porte fermée), les conseils Latex, les pyramides de raviers de la cantine, les bonnes adresses de resto, je voudrais remercier mes co-bureaux Alice, Antoine Weber, Clément, Daniele, Franck, Jeanne, Manuel, et Toufik. Je suis heureuse d'avoir partagé tous ces moments de thèse et de vie en votre compagnie ! Un merci tout particulier à Jeanne pour son sourire communicatif (et pour Bredele) : tu m'as accueillie dès mon arrivée et tu n'as cessée d'être une confidente à toutes épreuves tout au long de cette thèse. Dans le bureau voisin, le 317A, j'ai eu le plaisir de rencontrer des personnes avec qui j'ai énormément échangé (pas uniquement car la cloison est fine et que les voisins ont la voix qui porte). Merci à Aidan, Alexis, Antonio et Yann pour tous les cafés, tisanes et bonbons partagés. Un immense merci à Antoine Lagarde dont la gentillesse, la tolérance et la bonne humeur ne sont qu'un extrait de la liste de tes qualités. Si on continue dans le couloir du 3ème étage du laboratoire, j'ai eu la chance de rencontrer Laureline quelques bureaux plus loin. Merci pour toutes les discussions, les longs échanges sur les péripéties de la vie et l'attention dont tu fais preuve envers ceux qui t'entourent. Un grand merci également à toi Mathis, pour tous les bons moments partagés au labo et en dehors, pour ta présence sans faille et ton écoute ! Au 4ème étage, il y a l'incontournable salle café où les rendez-vous quotidiens représentaient des boost d'énergie, grâce à la caféine mais aussi grâce aux personnes avec qui j'ai pu échangé pendant ces moments. Je pense notamment à Hugo, qui illuminait la pièce de son dynamisme et avec qui c'est un vrai bonheur de discuter de tout, sans tabou. Il me faudrait beaucoup plus que quelques lignes pour remercier Antoine Monier, tant il m'a épaulée pendant cette thèse et dans la vie quotidienne. On a surmonté les épreuves ensemble, le confinement, la rédaction et je n'aurais pas pu rêver meilleur partenaire que toi. La suite s'écrira sous le soleil de la Méditerranée puisque tu quittes en même temps que moi le laboratoire, laissant ton bureau à Rodolphe. J'en profite pour te remercier Rodolphe, pour ton sens de l'humour et les multiples discussions scientifiques dans la salle de l'imprimante !

J'ai également une pensée toute particulière pour mes camarades CMI, lancés pour beaucoup à la poursuite d'un doctorat. Adrien, Antoine Monod, Ariane, Aurélien, Bassem, Charlotte, Jean, Léa, Madu, Marie et Natan, on se donne bientôt rendez-vous pour fêter les 10 ans de notre rencontre ! J'en profite pour remercier Hélène Dumontet pour le soin incroyable avec lequel elle accompagne les étudiants et pour tous ses bons conseils. Au cours de mes études, de divers stages j'ai eu la chance de rencontrer de chouettes copains, qui répondent toujours présents bien des années après : Thierry, Hanna, Niels, merci !

Un grand merci à mes amis d'enfance et du lycée, Axel, Julia, Léa, Louise et Robin pour leur soutien, pour tous les week-end à travers la France et pour les soirées partagées qui m'ont permis de garder le moral au beau fixe.

Finalement, je tiens à remercier tous les membres de famille, ma maman, mon Papa, Elisabeth, Juju, Camille, Léna, Céline, Fabien, Tata, Sophie qui m'ont soutenue pendant toutes ces années et qui sont si précieux. Merci à ma grand-mère moderne, Jacqueline, qui m'a suivie en direct sur Youtube depuis sa tablette ! Enfin, je pense bien sûr avec émotion à ma grand-mère Yvonne et mon papi Christian qui sont toujours avec moi, dans mes souvenirs et dans mon cœur.

Contents

Introduction

Droplets are familiar objects that raise a lot of questions from an academic and industrial point of view. There is a wide variety of droplets: spherical droplets constituting an aerosol, pendant droplets suspended downward at the outlet of a tap and droplets sitting on top of a horizontal solid substrate called sessile droplets. Sessile droplets can be found on car windshields, on plant leaves after the morning dew or on the kitchen table when coffee is poured next to the cup. The interaction between the sessile droplet and the substrate is widely studied for its numerous applications in engineering such as medical diagnosis [1–4] and control of coating/printing technology [5–7].
Depending on the atmospheric conditions (temperature, relative humidity), the equilibrium state of these droplets is disturbed and this can lead to a phase transition from the liquid state to the gaseous state: evaporation. Evaporation is an everyday phenomenon but a crucial topic of interest to diverse scientific communities. Evaporation of sessile droplets represents a challenging subject due to the complexity associated with modeling the evaporative mass flux, different modes of evaporation and the dynamics at the triple contact line. The complexity comes from the many physical phenomena that are involved such as internal flow hydrodynamics, phase change transition, wetting, diffusion and convection flows. Environmental parameters (humidity, temperature) and substrate characteristics (material, roughness) play a major role in the dynamics.

Depending on the composition of the liquid forming the droplet, if solutes or suspended particles are present, a deposit is left on the substrate at the end of evaporation. By understanding the evaporation dynamics, one can predict the particle deposition profile on the substrate and explain the various morphologies observed. The effect of non-volatile solutes, such as salts, is of particular interest since they are often found in nature [8–10] and human biofluids [11–13]. The presence of salty sessile droplets is an issue: it can lead to crystallization, which is problematic in the formulation of some drugs [14], or to corrosion of the substrate if it is metallic, which induces an undesirable degradation of materials [15, 16].

In the marine environment, the materials are in contact with a humid environment loaded with salt, particularly sodium chloride which is the main salt dissolved in sea water. They are exposed to sea spray, aerosols blown off the crest of the waves or formed by the surf that let sessile droplets on surrounding infrastructures. Sessile droplets can induce corrosion as they act like an electrolyte. Particular corrosion phenomena that are still little understood are due to this geometrical configuration [17–20]. For instance, atmospheric corrosion of metals which can take place under a droplet is the most common type of corrosion. It has a significant impact on the environment and operational safety in various situations of everyday life [21–23]. Moreover, the diurnal cycles involving the repetition of evaporation and condensation phases affect the corrosion behavior [24, 25]. The prediction of atmospheric corrosion phenomena requires a detailed understanding of the hydrodynamics taking place within the droplet during

evaporation. In order to achieve this, we want to move towards a model that would allow to describe the evaporation dynamics and also the corrosion dynamics. This represents an important challenge since it is a question of treating the interaction between several fields: fluid mechanics, crystallization, electrochemistry and corrosion. This work focuses on the hydrodynamic part keeping in perspective that the corrosion part can be added in future works. The idea is to work step by step, becoming more complex as we go along: this is why we first consider pure water droplets before moving on to saline droplets. We develop a numerical tool with the free-software Basilik to reproduce the evaporation dynamics of sessile droplets for unpinned and pinned evaporation modes, over a wide range of contact angles, initial volumes and relative humidity for pure liquids and binary mixtures containing sodium chloride. To validate this numerical model, an experimental study is set up. It also allows to improve the understanding of the morphology of salt deposits and what happens during evaporation cycles.

The following manuscrit is composed of six chapter which successively explain the theory of sessile droplet evaporation, the numerical tool used in this work, the study on pure water droplets and finally the study on saline droplets.
Chapter 1 presents different physical concepts that will be used throughout the whole work such as surface tension, wetting and pure diffusion model for evaporation.
Chapter 2 introduces the numerical tool used to develop the model and perform numerical simulations, the open-source code Basilisk.
Chapter 3 details the first series of experiments done with pure water sessile droplets. The data will be then useful to validate the numerical results.
Chapter 4 explains the different numerical implementations we developped to simulate the evaporation of a pure sessile droplet. The numerical result about the dynamics of the two evaporation modes are discussed.
Chapter 5 describes the second series of experiments done with saline sessile droplets. The salt patterns are studied depending on the initial salt concentration and the relative humidity. A first experimental approach of evaporation cycles is also presented.
Chapter 6 presents the first numerical results for the simulation of a saline droplet. The calculation method for the Marangoni stresses is detailled.

1 Scientific background

This first chapter presents different physical concepts that will be used throughout this work. The goal is to present the basics of the theory of the evaporation of sessile droplets before presenting the numerical tool in the next chapter.
A droplet may appear to be a simple physical system, but it is in fact complex and mixes several important concepts. The surface tension and the wetting properties are in particular determining for the shape of a droplet on a surface, i.e. a sessile droplet. To recover a geometrically known shape, we make the assumption that the droplets we study are spherical caps. In the first part of this chapter, we discuss this assumption and show that it is justifiable in the range of conditions chosen for the study.
We study a dynamic droplet, which evolves with time as it evaporates. This phase change phenomenon is governed by a vapor concentration gradient. This process is driven by diffusion and convection, but we simplify to a purely diffusive approach that reliably represents the physics. The evaporation dynamics of a pure liquid sessile droplet is presented in a second part.
This study leads to consider droplets of saline solution, which are a mixture between water and sodium chloride. This mixture complicates the evaporation dynamics but also the hydrodynamics within the droplet. The last part of this chapter therefore focuses on the evaporation of the mixtures and the morphologies of the deposits left after complete evaporation.

Contents

1 Physical concepts for the study of drops

In nature, droplets are ubiquitous. The rain is composed of multiple spherical droplets, pendant drops can be observed when a tap leaks and the droplets resting on plants after the morning drew are called **sessile droplets**. This study focuses on droplets and in particular on sessile droplets, which are drops on substrates. Although simple in appearance, the droplet represents a complex physical system where many mechanisms interact: surface tension, wetting, gravity, vapor diffusion, evaporation flux, convection, Stefan currents, capillary flow and Marangoni effect (Fig. 1.1). Depending on the conditions of evaporation, some mechanisms become preponderant, which justifies the assumptions made when modeling the problem. If the droplet is not in equilibrium with the surrounding environment, then the evaporation phenomenon is added and leads to very particular dynamics inside and outside the droplet. The evaporation dynamics will be explained in the next section, we first focus on the physical concepts that govern the shape of the droplet. We therefore introduce some basic notions about **surface tension** and **wetting** in the first two paragraphs in order to discuss in the third paragraph the assumptions we make about the **spherical-cap shape** of the sessile drop.

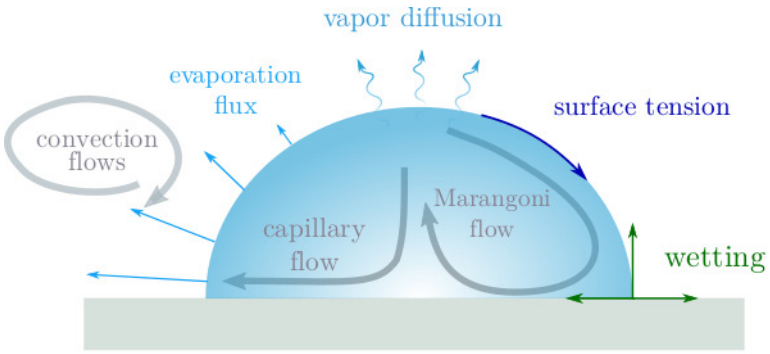

Fig. 1.1 – Mecanisms involved during the evaporation of a sessile droplet.

1.1 Surface tension

An interface can be seen as a thin and stretched membrane characterized by a force per unit length (from a mechanical point of view) or an energy per unit length (from a thermodynamical point of view) called the **surface tension** noted γ (N.m^{-1}) [26].
From a molecular point of view, the surface tension is a physico-chemical phenomenon due to the molecular interactions inside a liquid. Indeed, liquids are condensed phases in which the molecules have strong interactions with their neighbours. But the molecules near the interface of the liquid have less neighbours and then less interactions (Fig. 1.2), which corresponds to an energy deficit. To balance this deficit, the surface tension acts on the liquid interface to minimize the surface exposed to the environnement.

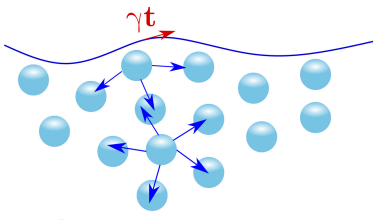

Fig. 1.2 – Molecules interactions in a liquid. The molecules near the interface have less interactions, there is a deficit in energy near the surface. The surface tension γ acts at the interface to compensate where $\mathbf{t}$ is the tangential vector.

The effect of surface tension can be observed in various examples in everyday life. When you open a tap, the water jet evolves spontaneously to droplets (Fig. 1.3a). This is the illustration of the Rayleigh-Plateau instability [27,28] which is linked to a tendency for fluids to minimize their surface area due to surface tension. As the surface tension guarantees the cohesion of liquids, it enables some insects or small animals to walk on water (Fig. 1.3b). It is always a competition between surface forces and volume forces (such as gravity).
The surface tension for water varies depending upon whether there is contact with air, with oil or with a solid. For instance, at 20 C°, the surface tension takes the following values: between water and air $\gamma = 72.8 \times 10^{-3}\,\mathrm{N.m^{-1}}$ whereas between water and oil $\gamma \approx 50.0 \times 10^{-3}\,\mathrm{N.m^{-1}}$ [26]. The surface tension plays an important role in the shape of the water drops and this is why it is a central concept in this study.

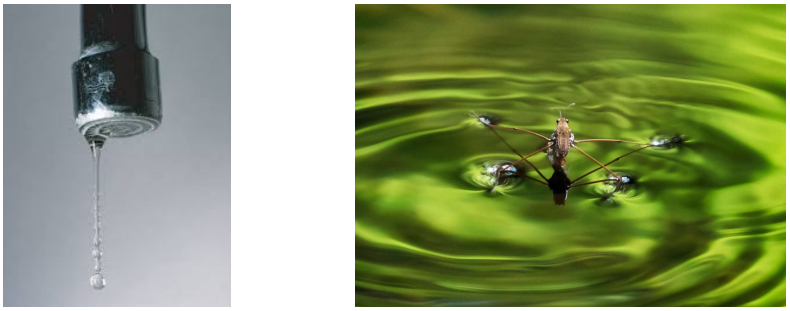

(a) (b)

Fig. 1.3 – Various examples of the effect of surface tension. (a) Rayleigh-Plateau instability (Photo from [29]) and (b) insect walking on water (Photo: Masayatartarus).

Temperature

The surface tension of a liquid varies with the local value of the temperature [30,31]. For most pure liquids, the relation of the surface tension with the temperature T (°C) is quite well-known: it decreases almost in a linear way and reaches zero at T_{crit}

$$\gamma(T) = \gamma_0 - \frac{\delta\gamma}{\delta T}(T - T_0) \quad \text{with} \quad \frac{\partial\gamma}{\partial T} = cste \tag{1.1}$$

where γ_0 is the surface tension at ambiant temperature T_0.
Thus, temperature gradients give rise to surface tension gradients. These gradients induce convective transport flows: this is called the **thermal Marangoni effect** [32,33].
In this study we consider that the temperature does not impact the surface tension. We assume that the temperature stays constant, so the surface tension is not affected by temperature variations. The evaporation cools the surface and induces a temperature gradient in the thickness of the droplet, however this effect remains negligible [34]. Some experiments were done to verify this hypothesis at the beginning of this study with a thermal imaging camera to analyze the temperature field during the evaporation of a sessile droplet of pure water or saline solution. No temperature gradients were observed during the experiments.

Minerals salts

Surface tension can also be modified by compounds called surfactants [35]. The properties of these molecules allow them to position at the interface and thus modify the surface tension locally. In most cases, surfactants lower the surface tension and facilitate the formation of

droplets. In this study, we consider saline droplets composed of a mixture of water and mineral salts. Mineral salts act like surfactants but they increase locally the surface tension. The evolution of the surface tension as function of the salt concentration c (mol.L^{-1}) for aqueous saline solutions can be described by the following law

$$\gamma(c) = \gamma_0[1 + b(c - c_0)] \tag{1.2}$$

where c_0 is the reference concentration in salt for which the surface tension γ_0 has been defined and b is a constante function of the liquid considered.
As an example, we represent the evolution of the surface tension as a function of the salt concentration for two mineral salts, magnesium chloride $MgCl_2$ and sodium chloride NaCl (Fig. 1.4). For both cases, the surface tension increases suddenly with the salt concentration when a certain salt concentration value is exceeded, around 10^{-1} mol.L^{-1}. The surface tension is a local quantity that varies with the local salt concentration: in highly concentrated areas, the surface tension increases. If we consider non-homogeneous concentration fields, it creates to surface tension gradients. These gradients can then lead to convection movements: this is called **Marangoni solutal flow**. This phenomenon is identical to the thermal Marangoni effect but the driving force is here a concentration gradient and not a temperature gradient. In this study, we consider only the sodium chloride as the mineral salt of interest. The solutal Marangoni effect in the case of an evaporating saline droplet will be described in more details in the paragraph 3.1.

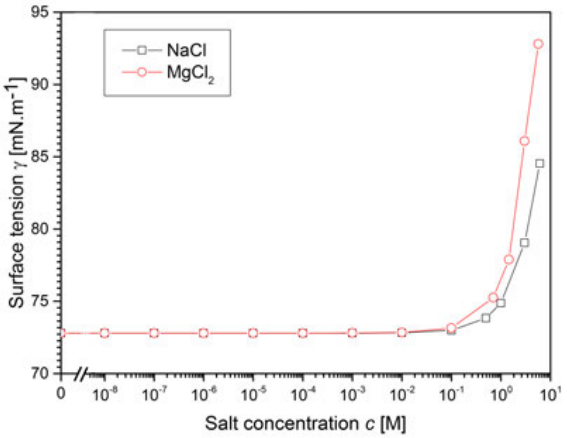

Fig. 1.4 – Evolution of surface tension for two aqueous saline solutions, magnesium chloride $MgCl_2$ and sodium chloride NaCl solutions [36]. For both cases, the surface tension increases with the salt concentration but the surface tension increment is two times bigger for the magnesium chloride solution for a similar salt concentration range. (Figure reproduced from [37])

1.2 Wetting

When a droplet is deposited on a substrate, it spreads out until it reaches an equilibrium position defined by a particular contact angle. This first phase is described by Tanner's law [38–40]. The initial equilibrium phase usually lasts for less than a minute. In this study, we consider that the droplet is already at equilibrium at the initial time. In the numerical simulations is quite easy to respect this hypothesis but we will see that it is much more uncertain for the experiments.

Wetting refers to the study of how a liquid deposited on a solid (or liquid) substrate spreads out [41]. Nowadays, wetting properties are at the center of attention in numerous industrial areas. In agriculture, the deposition of insecticides on plants requires to modify the wetting properties to ensure that the chemical treatment products are well retained by the plants [42, 43]. For inkjet printing, technological issues are solved with new wetting solu-

tions [44]. In the food industry, the use of instant powders implies to control their properties when they are diluted in solutions [45,46]. Wetting is also really important in life sciences [47]: for instance, rise of sap in plants, locomotion of insects on the water surface, adhesion of parasites on wet surface and wetting of the eye.

The degree of wetting (wettability) is determined by a force balance between adhesive and cohesive forces. Wetting deals with the three phases of materials (gas, liquid and solid). When a liquid is deposited on a solid substrate, it can spread in different ways. The contact angle θ formed between the liquid and the substrate is the result of the wetting properties of the liquid-solid couple considered (Fig. 1.5). Depending on the value of this angle, several types of wetting can be distinguished

- **total wetting** where the liquid spreads completely on the substrate. The contact angle is zero. This corresponds to a thin film.
- **partial wetting** where the liquid forms a droplet on the surface: it is called a sessile droplet. A part of the substrate remains dry, the contact angle is non-zero. If the contact angle is smaller than 90°, the liquid has a high wettability (Fig. 1.5a), whereas if the angle is above 90°, the liquid is associated with a low wettability (Fig. 1.5c).

In this study, contact angles between 0 and 90° are observed depending on the wetting properties of the different solid substrates and liquids considered. The case where $\theta = 90°$ is quite particular and is often taken as a reference case as it corresponds to a half sphere (Fig. 1.5b).

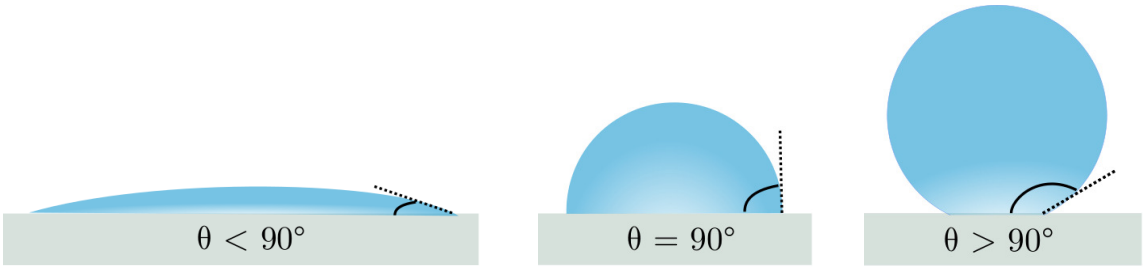

(a) (b) (c)

Fig. 1.5 – Different types of wetting for a sessile droplet depending on the value of the contact angle θ. (a) θ is clearly smaller than 90°, the wetting is almost total, the droplet looks like a thin film. (b) θ is equal to 90° which is a particular case of partial wetting. (c) θ is much greater than 90°, the wetting is limited, the droplet does not spread a lot on the substrate.

1.3 Spherical-cap shaped sessile droplet

The shape of a sessile drop is due to the competition between gravity and surface tension forces (Fig. 1.6). The capillary length L_c (m) allows to compare them

$$L_c = \sqrt{\frac{\gamma}{\rho_l\, g}} \tag{1.3}$$

where ρ_l and g are respectively the density of the fluid (kg.m^{-3}) and the gravity (m.s^{-2}). For water under earth gravity conditions, the capillary length is around 2.7 mm. Thus, if the radius of the droplet is smaller than the capillary length, the droplet has a **spherical-cap**

shape because surface tension is the dominant force (Fig. 1.6b). Otherwise, the droplet is flattened by the gravity (Fig. 1.6a). In this study, we only consider micrometer-sized droplets, thus for this reason, we refer drops as droplets in the following.

Fig. 1.6 – Influence of gravity on the shape of a sessile drop. (a) The drop is flattened by the gravity. (b) The gravity has no influence and the drop adopts a spherical-cap shape.

The **non-dimensional Bond number** Bo can also be used in order to characterize the importance of the gravity effects compared to the capillary effects

$$Bo = \frac{\Delta\rho\, g\, r_0\, h_0}{\gamma} \tag{1.4}$$

where $\Delta\rho = \rho_l - \rho_g$ is the difference of mass volume between air and liquid, g is the gravity, r_0 is the initial drop radius and h_0 is the initial drop height.
If the Bond number is small, the surface tension is bigger than the gravity forces and the droplet has a spherical-cap shape where geometrical relations exist between the radius r, the height h and the contact angle θ (Fig. 1.7). In this study, all sessile droplets have a spherical-cap shape[1]. The gravity does not play a role in the droplet geometry but should still be taken into account, especially in terms of flow fields inside the droplet [48] and sea salt deposit.

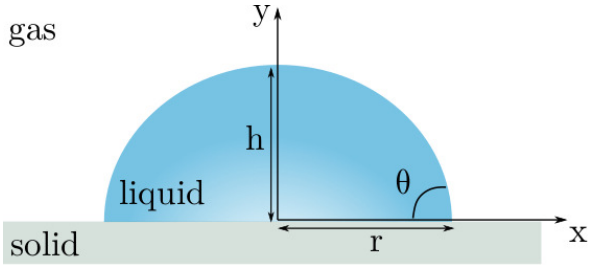

Fig. 1.7 – Representation of a spherical-cap shaped sessile droplet. The radius, the height and the contact angle are linked by geometrical relations which allow to calculate the volume of the droplet.

The spherical cap hypothesis allows to reduce to a simpler form where geometrical relations are known and simplify the calculation of some characteristics of the droplet (Fig. 1.7). For instance the volume of a spherical-cap shaped droplet is calculated as a function of its radius r and its contact angle θ [40]

$$V(r,\theta) = \frac{\pi r^3}{3}\frac{(1-\cos\theta)^2(2+\cos\theta)}{\sin^3\theta} \tag{1.5}$$

1. We consider pure water or saline sessile drops under atmospheric conditions: then, the surface tension is around 72×10^{-3} N.m^{-1}, the difference of mass volume can be approximated by the density of water and the gravity is $g = 9.81$ m.s^{-2}. The typical radius of the considered drops is 2.5 mm which ensures that the droplet can be regarded as a spherical cap.

There is also an equivalent relation involving the height h and the radius r of the droplet

$$V(r,h) = \frac{1}{2}\pi h\,(\frac{h^2}{3} + r^2) \tag{1.6}$$

In the case of a sessile droplet, three different interfaces are involved (Fig. 1.8)

- the interface between liquid and gas which corresponds to the droplet surface, characterized by a surface tension, γ_{LG}
- the interface between solid and liquid which corresponds to the contact area, characterized by a surface tension, γ_{SL}
- the interface between gas and solid which designates the dry part of the solid, exposed to the surrounding atmosphere, characterized by a surface tension, γ_{SG}

The contact angle is determined by the capillary forces acting at the edge of the droplet, at the **triple contact line** (TCL). The relation between the three surface tension forces acting at the contact line is given by Young-Dupré's equation [49]

$$\gamma_{\mathrm{SG}} = \gamma_{\mathrm{SL}} + \gamma_{\mathrm{LG}} \times \cos\theta \tag{1.7}$$

This equation can be interpreted as a force balance for the triple contact line, a simple mechanical equilibrium (Fig. 1.8).

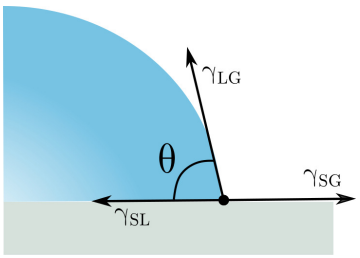

Fig. 1.8 – Force balance at the triple contact line of a sessile droplet. The three surface tensions define the value of the contact angle.

2 Evaporation dynamics for pure liquids

Evaporation of sessile droplets in ambient atmosphere is a well-known yet not completely understood problem of classical physics. It has been the subject of a great deal of interest, due to its increasing use in heat and mass transfer applications, biological systems and industrial applications. Exposed to the air environement, the sessile droplet can evaporate. It is a phase change phenomena from a liquid to its own vapor. The evaporation of a sessile droplet involves various **evaporation modes** which may succeed one another. Moreover, for a sessile droplet evaporating in still air resting on a substrate at the ambient temperature, the principal mechanism responsible of evaporation is **diffusion**. Pure diffusive models are often used to describe the evaporation phenomenon, however **convection** can also plays a role in the evaporation process in some cases.

2.1 Modes of evaporation

This paragraph is based on several articles and reviews of the literature that detail the different modes of evaporation and their characteristics [4, 50–56].
One of the most commun mode is called the **constant contact radius mode** (CCR) or **pinned mode** (Fig. 1.9a): the radius of the droplet remains constant whereas the contact angle decreases. In this way, the contact line is pinned to the substrate. This mode appears for liquids with particles in suspension, surfaces with a high energy or rough surfaces. The constant radius mode is usually the first evaporation mode after deposition (and is often designated as the first evaporation mode) but this mode can be skipped if the substrate surface is really smooth or if the liquid is completely pure.
After the constant radius mode, a second well-known mode called the **constant contact angle mode** (CCA) or **unpinned mode** usually appears (Fig. 1.9b). This mode is characterized by a constant contact angle whereas the contact line is moving as the radius decreases. The constant contact angle mode is often designated as the second evaporation mode. The transition between modes will be explained in the next paragraph. The constant radius mode is often used to describe evaporation of a pure liquid droplet on a smooth surface: this mode is very sensitive we will use it for the first study case of this work which is the evaporation of a pure water droplet.
Finally, at the end of evaporation, it becomes quite complicated to determine the exact evaporation behavior. This last phase is described as a combination of the two first modes : the radius and the contact angle are varying simultaneously (Fig. 1.9c), as a **stick and slide mode** [52]. The stick and slide mode is usually quite short, therefore it is often neglected.

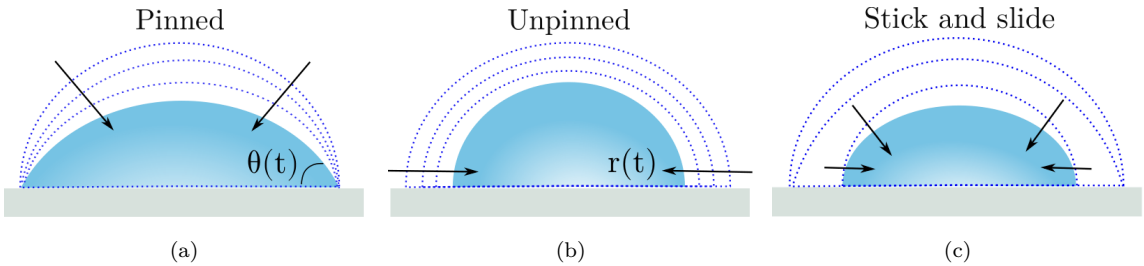

Fig. 1.9 – The different evaporation modes: the constant radius mode or pinned mode (a), the constant contact angle mode or unpinned mode (b) and the stick and slide mode (c).

The transition between the constant radius mode and the constant contact angle mode has been studied by some authors [**?**, 57] in particular Stauber [52] who characterized this

transition with a receding angle θ^* which is the critical angle for switching. θ_0 is the initial equilibrium angle after deposition

- if $\theta_0 > \theta^*$, the droplet first evaporates with a constant radius mode.
- if $\theta_0 < \theta^*$, the droplet first evaporates with a constant contact angle mode.

As explained previously, the behavior of the triple contact line is characterized by the relation between the different surface tensions (Eq. 1.7). In this way, a pinning force per unit length, $F_{\mathrm{p(t)}}$, can be derived as

$$F_{\mathrm{p(t)}} = \gamma_{\mathrm{lv}} \times \cos\theta(t) + \gamma_{\mathrm{sl}} - \gamma_{\mathrm{sv}} \tag{1.8}$$

When the droplet evaporates according to a constant radius mode, this relation implies that when $\theta(t)$ decreases, $F_{\mathrm{p(t)}}$ increases until a maximum, $F_{\mathrm{p_{max}}}$, which corresponds to $\theta(t) = \theta^*$. At this point, the transition between the two modes occurs as the forces at the contact line are too high and, finally, the triple contact line detaches and starts to recede. The contact line is then designated as unpinned and the second evaporation mode, the constant contact angle mode, begins. Stauber [52] derived a relation between θ_0 and θ^* in order to predict the value of the receding angle θ^* in fonction of the initial angle θ_0

$$\theta^* = \max\left(0, \arccos\left(f_{\mathrm{p}} + \cos\theta_0\right)\right) \tag{1.9}$$

where f_{p} varies with the surface tension. In this study, we assume that the droplet evaporates according to a single mode during the whole evaporation. There is no transition to simplify the dynamics.

2.2 Diffusive model for a pure evaporating droplet

We present the basic diffusive model for evaporation, for a **spherical droplet** and then for a **sessile droplet**. Other supplementary heat and mass transfer mechanisms can appear, such as convections (thermo-gravitational, thermo-capillary, and thermo-solutal) or radiation. The convection mechanism is discussed in the following section 2.3.

Spherical droplet

Evaporation is a **phase change** transition from a liquid to its own vapor. From the molecular scale point of view, it is a transfer of molecules from the liquid to the surrounding gas, while from a macroscopic scale point of view, it is a mass flux crossing the liquid/vapor interface. Evaporation occurs as soon as the vapor partial pressure in the gas is lower than the saturation pressure.

When a spherical droplet evaporates into air, the vapor concentration field c is uniform along the droplet interface, but it is not uniform through the gas phase. The vapor concentration at the droplet surface equals to its equilibrium or saturation condition c_{s}, whereas, far from the droplet, the vapor concentration reaches the boundary value $c_\infty \approx RHc_{\mathrm{s}}$, where RH is the relative humidity of the environment. The assumption of thermodynamic equilibrium of the vapor with its liquid at the interface is consistent [58]. Indeed, the distance of establishment of the vapor gradients is much greater than the length of diffusion of the vapor molecules so the equilibrium of the vapor with its liquid can be considered as immediate. The value of c_s depends on the temperature and the liquid composition, with the Raoult's law [59]. The vapor concentration difference in the surrounding gas phase creates a concentration gradient which drives the evaporation process. Thus, the transport of the vapor in the gas phase is

described by a convection-diffusion equation

$$\partial_t c + \overline{\nabla} \cdot (c\mathbf{u}) = \overline{\nabla} \cdot (D_\mathrm{v} \overline{\nabla} c) \tag{1.10}$$

where $\mathbf{u}$ is the velocity and D_v is the diffusion coefficient of the vapor in the gas phase. In a first approximation, a droplet of water evaporating into air at room temperature can be described as a **diffusive mechanism** where water vapor is only diffused into the gas phase (Fig. 1.10). We consider that the ambient air is at rest at the inital time and that the convection flows (second term on the left side of Eq. 1.10) that emerge because of the phase-change are negligible in the vapor transport. Thus, reduces to a simple **diffusion equation**

$$\partial_t c = \overline{\nabla} \cdot (D_v \overline{\nabla} c) \tag{1.11}$$

This hypothesis is justified by the value of the **non-dimensional Peclet number Pe** which compares convection and diffusion phenomena [40]

$$Pe = \frac{r_0 v_e}{D_v} \approx 10^{-5} \tag{1.12}$$

where r_0 is a typical distance of the system, the initial droplet radius and v_e is the evaporation velocity which scales as $v_e \approx D_v c_s / \rho_l r_0$.
By replacing v_e in Eq. 1.12, the Peclet number can be scaled as Pe_s

$$Pe_s \sim \frac{c_s}{\rho_l} \tag{1.13}$$

In the following, we will refer to this scale as the Peclet number. For a water droplet evaporating in air, $\mathrm{Pe_s}$ is of the order of 10^{-5}, thus evaporation can be seen as a **quasi-steady process**. This means that the vapor concentration adjusts rapidly compared to the time required for the entire droplet evaporation, t_F. The time ratio for water evaporation in air is between 10^{-6} and 10^{-9}, depending on the surrounding air humidity [40], which means that the quasi-steady hypothesis is consistent. Indeed, if we write the time ratio between the diffusive time $t_\mathrm{D} = r_0^2 / D_\mathrm{v}$ and the final time of evaporation t_F

$$\frac{t_\mathrm{D}}{t_\mathrm{F}} = \frac{r_0^2}{D_\mathrm{v}\, t_\mathrm{F}} \approx \frac{c_\mathrm{s} - c_\infty}{\rho_\mathrm{l}} \approx \frac{c_\mathrm{s}\,(1-H)}{\rho_\mathrm{l}} \ll 1 \tag{1.14}$$

Considering, the pure diffusion and the quasi-steady assumptions, Eq. 1.10 simplifies into the Laplace equation, $\Delta c = 0$. The vapor concentration field is thus the solution of a Laplace equation and the vapor transport is only a mass diffusion. From the Laplace equation, the concentration profiles are calculated.

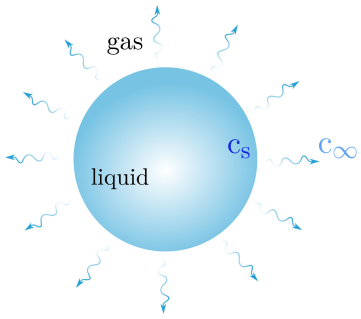

Fig. 1.10 – Spherical droplet evaporating in still air where the evaporation flux is uniform along the droplet interface. The evaporation is a diffusive process driven by the vapor concentration gradient, between the saturation condition is equal to c_s at the interface and the condition far from the droplet c_∞.

In order to describe the outward evaporation mass flux along the interface, **J**, the Fick's law [60] is used

$$\mathbf{J} = -D_v \overline{\nabla} c \tag{1.15}$$

As the vapor field is uniform around the droplet, the **evaporation flux is uniform** along the interface for a spherical droplet in still air. In order to calculate the evaporation mass rate dm/dt, Maxwell used an analogy with electrostatics in 1877 [61] and then in 1918, Langmuir solved the same problem with a heat conduction analogy [62]. The expression for the evaporation mass rate for a spherical droplet is expressed as

$$\frac{\mathrm{d}m}{\mathrm{d}t} = -4\pi r D_{\mathrm{v}}(c_{\mathrm{s}} - c_{\infty}) \tag{1.16}$$

An important and somewhat counter-intuitive remark here is that the evaporation mass flux is not proportional to the droplet surface area, but to the droplet radius. From this, we can find that the drop radius evolves as $r(t) \propto \sqrt{t_{\mathrm{F}} - t}$ which is equivalent to the well-known d^2 law [61]. This means that the droplet surface varies linearly with time. We will use the d^2 law to validate the numerical model in the Chapter 4.

Sessile droplet

In the case of a sessile droplet, the substrate has an influence on the evaporation mass flux. As the droplet is in contact with a solid substrate, there is a **loss of symmetry** and the problem becomes more complicated as a triple contact line zone appears. For small droplets forming a spherical-cap shape, with the **electrostatics analogy**, Maxwell [61] was able to propose a model (Fig. 1.11). This analogy helps to understand the effect of the solid substrate on the local evaporation flux. The analogue of a sessile droplet in electrostatics is a conductive biconvex lens, brought to a constant potential. The evaporation rate can then be calculated as integrals of Legendre functions by passing in toroidal coordinates. The vapor concentration field lines around the droplet converge to the triple point identically to the lines of an electrostatic field.

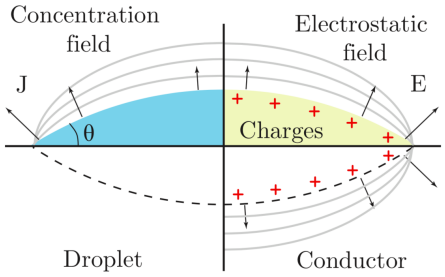

Fig. 1.11 – Electrostatics analogy first proposed by Maxwell [61] to solve the problem of the evaporation flux in the case of a sessile droplet. The evaporation mass flux J and the vapor concentration c are, respectively, the electrical field E and the electrical potential V. (Figure reproduced from [63])

For a sessile droplet, the **evaporation flux is not uniform** anymore along the interface because of the presence of the substrate, except for the particular case where $\theta = 90°$ due to the symetry. For contact angles between 0 and 180 °, there are three different situations

- for $0\,° < \theta < 90\,°$, the local evaporation mass flux is minimum at the apex of the droplet and maximum at the triple contact line (Fig. 1.12a). It increases along the interface when $r \to r_0$.
- for $\theta = 90\,°$, the evaporation flux is uniform as in the case of a spherical droplet (Fig. 1.12b).
- for $90\,° < \theta < 180\,°$, the local evaporation mass flux is maximum at the apex of the droplet and minimum at the triple contact line (Fig. 1.12c). It increases along the interface when $r \to 0$.

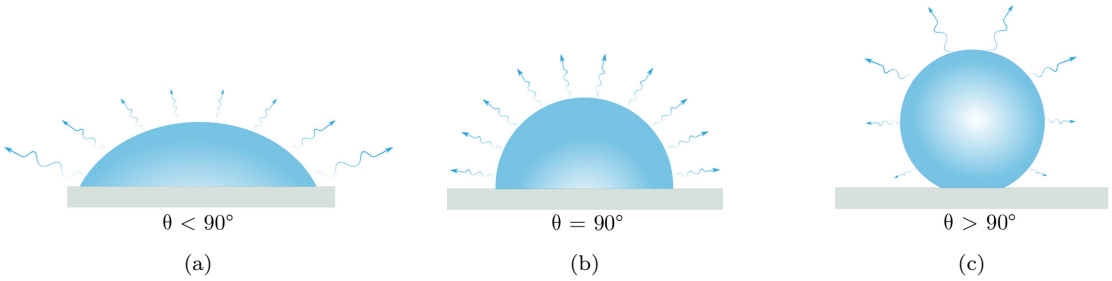

Fig. 1.12 – Different situations for the evaporation flux along the interface of a sessile droplet depending on the contact angle θ. (a) The flux is maximum at the edge of the droplet, (b) the flux is uniform and (c) the flux is maximum at the apex of the droplet.

An approximation of the evaporation rate for sessile droplet was derived based on Eq. 1.16.

$$\frac{\mathrm{d}m}{\mathrm{d}t} = -\pi r D_v (c_s - c_\infty) f(\theta) \tag{1.17}$$

where $f(\theta)$ is a function of the contact angle. Multiple analytical expressions have been derived for $f(\theta)$ [53].

In this study, the contact angles are between 0 and 90°, as a consequence the evaporation flux is non uniform along the droplet interface. The flux is more important at the triple contact line. In order to maintain the spherical-cal shape of the sessile droplet, this important mass loss at the edge of the droplet needs to be compensate. A **capillary flow** starts from the bulk of the droplet to the triple contact line to replenishe the area, as illustrated on Fig. 1.13. This sets the liquid in motion. The capillary flow is really slow but transports the fluid to the droplet edge [64, 65]. If some pollutant is present inside the droplet, it is carried by the capillary flow. This will be discussed in more details in the section 3.

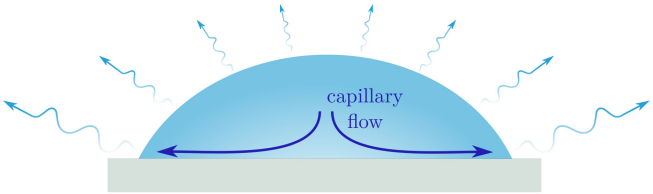

Fig. 1.13 – Capillary flow inside an evaporating sessile droplet to compensate the non uniform evaporation flux.

2.3 Convection

In the purely diffusive model, the transport of the vapor in the gas phase is done only by diffusion. This approximation is valid under the conditions considered in this study. However, there are convective models which take into account the convection for the transport of the vapor. We can quote for example the Spalding model [66]. This model is particularly useful in the combustion community. Indeed, the vapor can also be transported because of convective flows [40]. The vapor density is lower than the liquid density, which means that the volume of liquid that evaporates is smaller than the volume of the same amount of vapor. After the phase change, a bigger volume of vapor is created which generates a flow outward from the droplet. This flow is called the **Stefan flow**.

3 Evaporation of saline sessile droplets

Considering the evaporation of a mixture leads to a more complex system. In the following, we focus on binary mixtures, mainly composed of water to which a given concentration of pollutant is added. We are particularly interested in saline solutions containing sodium chloride: in this case, water evaporates while the salt dissolved in solution remains in the droplet and ends up crystallizing when its concentration exceeds a critical value.
The presence of different chemical species, in particular salt, influences the properties of the base solvent, such as surface tension or density. We will see in the first paragraph that a local modification of the surface tension leads to **Marangoni flows**.
Whether we study a volatile solution with particles in suspension or a binary mixture with a volatile solvent and a non-volatile solute, a **deposit** on the rest surface of the droplet is obtained at the end of the evaporation. This deposit can form different patterns depending on the hydrodynamics inside the droplet which are described in the second paragraph.

3.1 Marangoni effect

The evaporation of mixtures often leads to concentration gradients inside the droplet, especially if the different species present do not have the same volatility properties. In the case of a **saline droplet**, with a certain initial concentration of sodium chloride ($NaCl$[2]), the water evaporates whereas the sodium chloride stays inside the droplet and precipitates to form salt crystals. This has an impact on the local value of the surface tension. For a sessile droplet of pure liquid, the surface tension is uniform along the interface and constant through the whole evaporation: it is not the case for a saline droplet that evaporates in contact with a solid substrate.

As explained previously, the evaporation flux is not uniform along the droplet interface. The flux is stronger near the triple contact line, which causes an internal capillar flow from the droplet bulk to the edge (Fig. 1.13). In the presence of the NaCl (represented by the small red particles inside the droplet), this flow drives the NaCl to the triple contact line, which becomes an area highly concentrated in salt as the water evaporates (Fig. 1.14a). As evaporation progresses, the edge of the droplet becomes more and more concentrated in NaCl whereas the rest of the droplet becomes less and less concentrated (Fig. 1.14b). This creates a **concentration gradient** along the interface of the droplet which leads to a surface tension gradient. Indeed, the surface tension depends on the local salt concentration: the surface tension increases with the salt concentration according to Eq. 1.2 as shown on Fig. 1.4. This **surface tension gradient** is responsible for the **Marangoni flow**, which goes from the areas with a low surface tension to areas with a high surface tension, as illustrated on Fig. 1.14c.

The Marangoni flow which goes from the apex of the droplet to the edge of the droplet replenishes even more the area of the triple contact line: it enhances the salt intake even more which renforces the concentration gradient and therefore the Marangoni flow itself. It is a self-sustaining system.
The Marangoni flow changes the hydrodynamics inside the droplet. This new flow brings fluid to the triple contact line which compensates the evaporation loss. It participates to maintain the spherical-cap shape of the droplet as the capillary flow. But the Marangoni flow is much

2. When sodium chloride (NaCl) is dissolved in a solution it forms sodium ions Na^+ and chloride ions Cl^-. By abuse of language we often refer to the concentration of sodium chloride in the solution. In the specific case considered here, the evaporating sessile droplet, the two different ions are transported to the same areas and salt crystals eventually appear as evaporation proceeds.

stronger than the capillary flow already induced by the evaporation mass loss. This means that at one point the Marangoni brings more fluid than necessary to the edge of the droplet. To maintain the correct balance at the triple contact line, a flow from the droplet edge to the bulk of the droplet appears, in the opposite direction of the capillar flow. At one point, convection cells due to the Marangoni flow are created inside the droplet (Fig. 1.14d).
The hydrodynamics inside the droplet depends on the initial salt concentration as the Marangoni flow increases with the concentration gradient. The hydrodynamics has an impact on the salt repartition inside the droplet and therefore on the salt deposit patterns observed after complete evaporation. The different patterns are presented in the next paragraph.

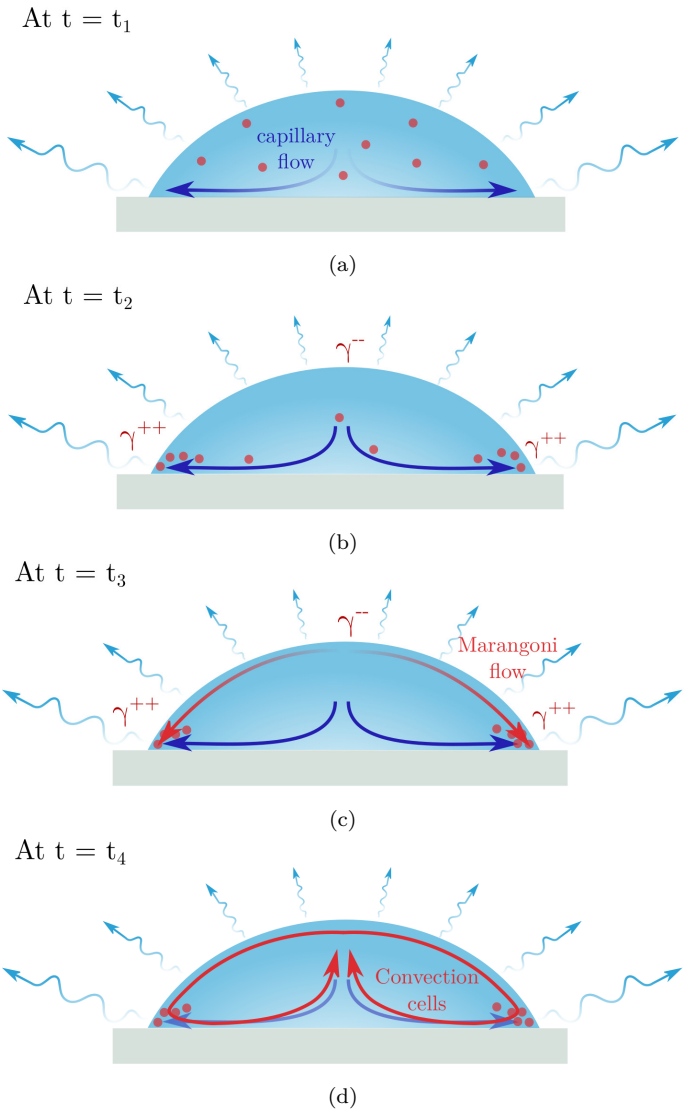

Fig. 1.14 – Formation of concentration gradients in an evaporating saline sessile droplet. The capillary flow transports the salt (represented by the red particles) to the triple contact line (a, b) and finally a Marangoni flow emerges because of the surface tension gradient due to the high salt concentration at the droplet edge (c). Convection are created when the Marangoni flow becomes strong (d).

3.2 Salt deposit patterns

After the complete evaporation of micrometer-sized saline droplets, a salt deposit rests on the solid surface [4, 67]. These deposits are an important issue for many applications. Their morphology depends on the hydrodynamics taking place within the droplet during evaporation. Predicting the deposits requires an understanding of the dynamics of the internal flows. The salt patterns observed depend on different parameters, but the most important is the **initial salt concentration**.

For a low initial concentration, $c_0 < 10^{-3}$ mol.L^{-1}, the concentration gradients inside the droplet stay very small and thus the Marangoni flow is really slow. The capillar flow is present to compensate the evaporative flux which brings the salt at the triple contact line. The slow Marangoni flow also helps to bring salt at the contact line (Fig. 1.15). At the end of the evaporation, all the salt contained in the droplet is distributed along the edge of the droplet. This forms a ring of salt after complete evaporation, which is called a **coffee-ring pattern** (Fig. 1.17a) after the famous experiment of Deegan [68]. He deposited a coffee droplet onto a solid substrate and after evaporation he observed that the coffee-particles were deposited along the perimeter of the coffee spill.

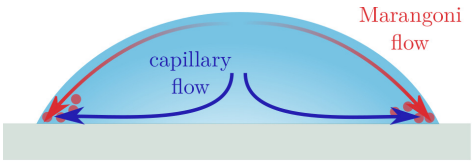

Fig. 1.15 – Hydrodynamics inside the droplet leading to a coffee-ring pattern for the salt deposit.

When the initial salt concentration increases, c_0 between 10^{-3} and 10^{-2} mol.L^{-1}, the deposit changes. This is due to a change in the hydrodynamics inside the droplet. An increase of the initial concentration leads to a stronger Marangoni flow which drives some flow from the droplet apex to the edge. When the amount of liquid supplied jointly by the Marangoni flow and the capillary flow exceeds the amount of liquid evaporating at the triple line, a new flow is created from the edge of the droplet to the bulk in order to maintain an equilibrium and the spherical-cap shape of the droplet (Fig. 1.16). This results in a new repartition of the salt, the salt does not only accumulate at the droplet triple contact line, it is distributed over all the contact surface between the droplet and the substrate. This pattern is called the **uniform pattern** (Fig. 1.17b).

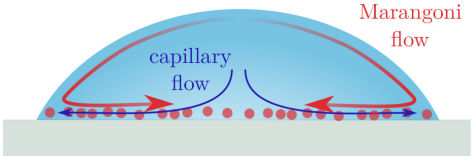

Fig. 1.16 – Hydrodynamics inside the droplet leading to a uniform pattern for the salt deposit.

If the initial salt concentration increases a little bit more, $c_0 > 10^{-2}$ mol.L^{-1}, some salt crystals are formed on the substrate. For this range of salt concentration, the surface tension varies and increases as shown on Fig. 1.4. This leads to strong flows that carry quickly the salt to the triple contact line. Salt crystals form when the **supersaturation limit**, also called the metastable limit, is exceeded. This limit S is defined as the ratio between the concentration inside the droplet at the time of nucleation c and the saturation concentration c_{sat}

$$S \sim \frac{c}{c_{sat}} \tag{1.18}$$

where $c_{sat} = 6.1$ mol.L^{-1} for NaCl. This limit remains very dependent on the experimental

conditions, between 1.8 and 1.03 [69, 70]. Because of the flows inside the droplet, locally the saturation condition may be reached. A deposit with crystals is called a **crystal pattern** (Fig. 1.17c).

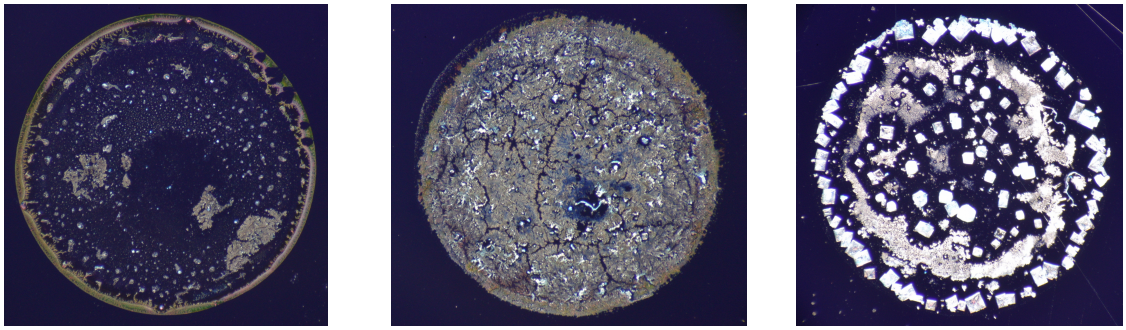

(a) (b) (c)

Fig. 1.17 – Different morphologies of salt deposits obtained after complete evaporation of saline sessile droplet during the experiments. The initial salt concentration c_0 varies for each case: (a) coffee-ring pattern with $c_0 = 10^{-3}\,\text{mol.L}^{-1}$, (b) uniform pattern with $c_0 = 10^{-2}\,\text{mol.L}^{-1}$ and (c) crystal pattern with $c_0 = 2.5 \times 10^{-1}\,\text{mol.L}^{-1}$. ($V_0 = 10\,\mu\text{L}$ and $RH = 50\%$)

What to remember ?

Sessile droplets, i.e. droplets placed on a substrate, are the object of study in this work. The shape adopted by the droplet results from a competition between gravity and tension, which is characterized by the dimensionless Bond number. In this study, the Bond number is lower than 1, which means that gravity has no influence on the droplet shape. The sessile droplets can then be seen as spherical caps, which allows to establish simple geometrical relations between the contact radius, the height, the contact angle and the volume.
Depending on the atmospheric conditions to which the droplet is subjected, it can evaporate. An imbalance at the interface of the droplet leads the liquid to transform into its own vapor. The transport of the vapor in the gas phase is considered as purely diffusive and quasi-stationary.
The interaction between the substrate and the droplet is globally expressed by the value of the contact angle. However, the surface state of the substrate as well as the composition of the liquid (pure or mixture) determine the evaporation mode that the droplet will follow: unpinned mode, where the radius decreases while the contact angle remains constant, or pinned mode, where the radius remains constant while the contact angle decreases.
The presence of the substrate leads to an inhomogeneous evaporation flow along the droplet interface, which is more important at the triple line when the contact angle is less than 90°. In the pinned evaporation mode, this non-homogeneity of the evaporation flow induces a flow within the droplet from the top of the droplet to the triple line to compensate for the large liquid loss at this point. This flow is called the capillary flow and therefore carries liquid as well as any particles present in the liquid to the edge of the droplet. In the case of the saline droplets that will be studied in this work, this results in particular morphologies of saline deposits once evaporation is complete.

2 Numerical tool

To study the evaporation of sessile droplets, numerical simulations and experiments are performed. In this chapter, we present the free-software Basilisk which is used to build the numerical model. This tool is particularly adapted to the study of two-phase flows with a moving interface. Several numerical implementations need be added to the already developed code. This will allow to faithfully reproduce the physical phenomena involved in the evaporation of a sessile droplet and it will be explained in a following chapter.
In the first section, the philosophy and advantages of the Basilisk code are presented such as the already developped solvers, the staggered grid and the Adaptative Mesh Refinement. In the second section, we detail the continuous equations that control the physical problem of an evaporating sessile droplet. We consider the diffusion equation for the vapor around the droplet and the Navier-Stokes equations for the flows inside and outside the droplet. Explanations are given on how to take into account the phase change in the conservation equations. Indeed this is a complex step in numerical models and an approach has been developed in this study. We also discuss some assumptions made to build the numerical model. The numerical methods used to solve the equations are presented. The last section explains the non-dimensionnalization of the equations: we present the scales of the problem and the dimensionless numbers that control the evaporation dynamics. This leads to explain the choice of the numerical parameters of the code.

Contents

1 Basilisk, a solver for two-phase flows

1.1 Philosophy

Basilisk is a **free software** (Fig. 2.1) developped at Jean Le Rond D'Alembert Institute by Stéphane Popinet and collaborators. Basilisk is the successor of Gerris, another free software program developped by the same authors a few years ago [71]. It implements numerical methods of finite volumes [72] for **partial differential equations**, such as the Navier-Stokes equations and the diffusion equation. Basilisk is written in its own language, Basilisk C, based on the C language of which it remains really close. Basilisk allows to perform Direct Numerical Simulations (DNS).

Fig. 2.1 – The Basilisk logo. The software is named after a specie of lizards, the common Basilisk. This animal is famous for its ability to run on the surface of water and illustrates the competition between gravity and surface tension.

As Basilisk is a free software, every user has access to the source code and can modify it. The development of the code is then based on user contributions.
Several pre-defined **solvers** are already implemented and available such as the ones for the diffusion equation or the Navier-Stokes equations [73] and thus we can easily use them to treat the evaporation problem.

1.2 The one-fluid formulation

We consider fluid flows with interfaces. For two immiscible fluids in a domain, the domain can be decomposed into **two separated phases**, each containing one of the two fluids. There are two ways to formulate this to build a numerical model with two phases [74]. Here we briefly describe the two approaches in order to highlight the differences and to justify the choice of formulation that is adopted in the Basilisk software.

The first aproach, also known as the classical formulation or the **two-fluid formulation**, seems to be the most intuitive and the closest to the theoretical writing of a model. Each phase is defined by its own set of equations and thus the equations are managed separately in each of the two phases (Fig. 2.2a). In order to link the two phases at the interface, we need to define jump conditions that guarantee the continuity of the motion as well as the conservation of the mass across the interface. For instance, the software COMSOL Multiphysics is based on the two-fluid formulation [75].
A second approch, called the **one-fluid formulation**, exists to describe fluid flows with interfaces. In this formulation, the governing equations are written for the whole flow domain, there is **only one set of equations** for the two different phases (Fig. 2.2b). The two phases are treated as one unique fluid with material properties that vary abruptly at the interface. Thus, the jump conditions are not needed anymore but we need to add singular terms (with Dirac functions) to the equations, to take into account the "extra" forces at the interface, like the surface tension for instance. The singular terms are the counterpart of the jump conditions of the preceding method.

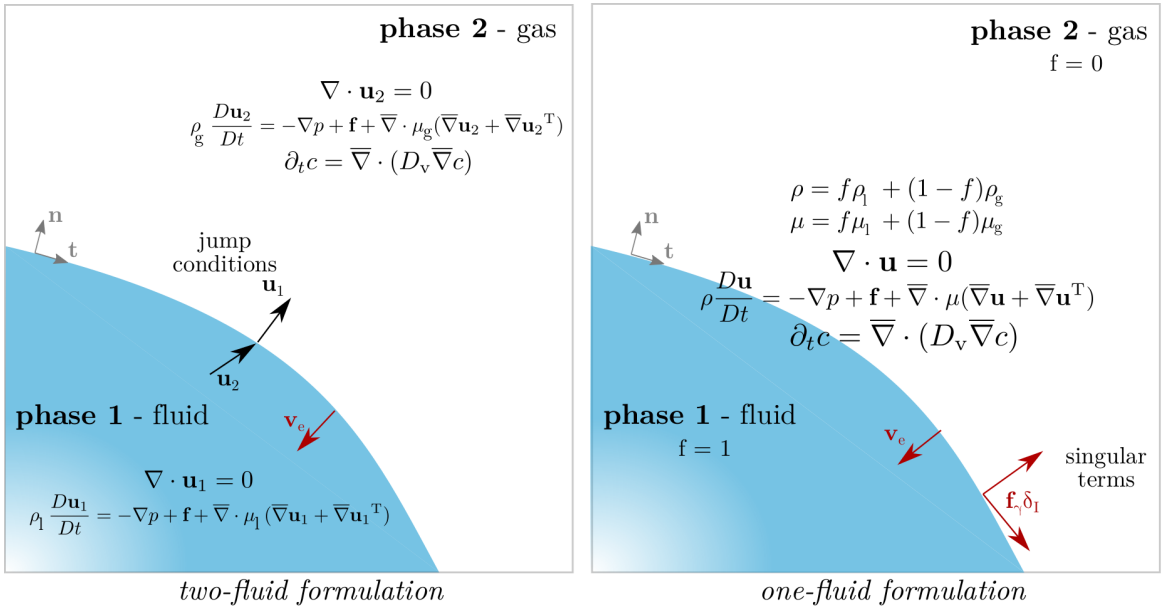

Fig. 2.2 – Comparison of the two approaches to treat two-phase flows in numerics. (a) The classical two-fluid formulation is presented with a set of equations in each of the two phases and jump conditions at the interface. (b) The one-fluid formulation used in Basilisk is introduced with a unique set of equations for both phases and singular terms at the interface.

To identify the different phases in the one-fluid formulation, we use a **marker function** that changes abruptly at the interface between the phases. The role of the marker function is to identify each phase as the marker takes various values in the different phases. In Basilisk, the marker function is the **volume fraction**, f. In the case of a droplet evaporating in air, the volume fraction describes the proportion of the liquid (by convention) in a cell: if f equals to 1, the cell is full with liquid and it belongs to the liquid phase, if f equals to 0, the cell belongs to the gas phase. Cells having intermediate values contain both liquid and gas: then, those cells are called "mixed cells" as they contain the interface. In this way, the interface can be localized and then reconstructed piece by piece, as illustrated on Fig. 2.3. We use the volume fraction to determine the properties of each phase, such as the density ρ and the viscosity μ. As we consider a one-fluid formulation, the fluid properties are described with continuous equations through the whole domain and we need to adapt their values in each phase where the index 1 denotes the fluid phase and 2 the gas phase

$$\begin{cases} \rho = f\rho_l + (1-f)\rho_g \\ \mu = f\mu_l + (1-f)\mu_g \end{cases} \tag{2.1}$$

The marker function has to be updated as the fluids move: in fact, advecting the marker function f is a key step which may be complex. To overcome this difficulty, in the frame of the one-fluid formulation, several numerical methods exist to study the interface: we will discuss them later in the section dedicated to the advection of the interface.
The one-fluid formulation is equivalent to the classic "two-fluid" formulation, but it is the starting point for several numerical methods based on fixed grids, as the ones implemented in Basilisk.

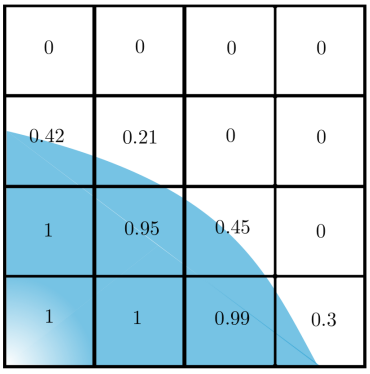

Fig. 2.3 – Schematic representation of a simulated droplet in Basilisk. Volume fraction attached to each cell around an interface: the liquid phase is located in blue in the bottom left corner of the domain and the gas phase is all around.

1.3 Reconstruction and advection of the interface

In the one-fluid formulation for the two-phase flows, the interface is identified thanks to the marker function, the volume fraction f in Basilisk. As the flow evolves, the interface moves and the marker needs to be updated. The advection step can be quite challenging but there exist two mains methods [74]

- Level Set is a function of level line where the level 0 corresponds to the interface [76]. It is a really powerful method which allows to reconstruct the interface with a good accuracy. The major disadvantage is that the mass conservation is not always perfectly verified.
- **Volume-Of-Fluid (VOF)** considers a unique phase characterized by a volume fraction f. It allows to track the interface which will be reconstructed piece by piece with an affine function. This method enables a satisfactory reconstruction of the interface and guarantees the mass conservation. The VOF method is the oldest and most common used [77]. However, the interface reconstruction is less accurate with the VOF method [78].

Basilisk uses the VOF method as there are some advantages such as the mass conservation. The first step of the VOF method is the reconstruction of the interface based on the volume fraction, f. From the value of f in the neighbouring cells, Basilisk reconstructs the interface piece by piece. This method solves rapidly the interface position by using only the 8 cells around the cell of interest. Then, the second step consists in advecting the reconstructed interface with a given velocity field. For this, we need to determine the fluid quantity going from one cell to another using the volume fraction in the cell of interest, the interface position and the velocity between this cell i and the cell $i+1$. The velocity is noted $u^{\mathrm{i+1/2,j}}$. In the cell i, we define a rectangle of length Δ, which is the length of the cell, and of width $u^{\mathrm{i+1/2,j}}\Delta t$. The volume fraction contained in this rectangle is transported to the cell $i+1$ as illustrated on Fig. 2.4.

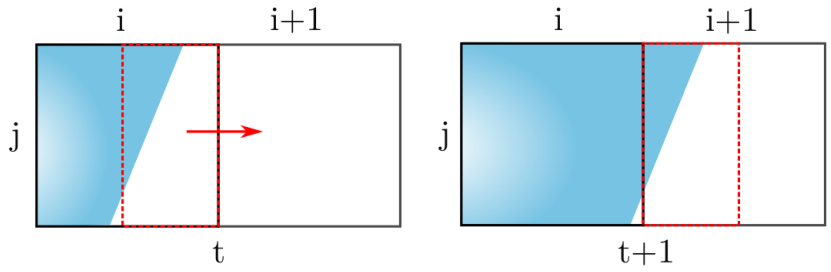

Fig. 2.4 – Advection of the interface with the Volume-Of-Fluid (VOF) method.

1.4 Adaptative Mesh Refinement

Basilisk provides a Cartesian fixed grid and guarantees consistent field values in a 5x5 neighbourhood (in 2D). Discretisation schemes often rely on special arrangements of discretisation variables relative to the underlying grid. This is called variable **staggering**: all the flow variables are not defined at the same locations in constrast with collocated grids where all variables are defined at the same points of the grid. Basilisk provides support for the three most common types of staggering: centered (the default), face and vertex staggering. For instance, the pressure p is defined as a centered variable, in the center of each cell, the velocity u is defined as a face variable and the vorticity ω is defined as a vertex variable (Fig. 2.5). There are some advantages to use a staggered grid instead of a collocated grid:

- the calculation of the pressure gradient is more accurate,
- it provides conservative methods,
- the coupling between variables is stronger.

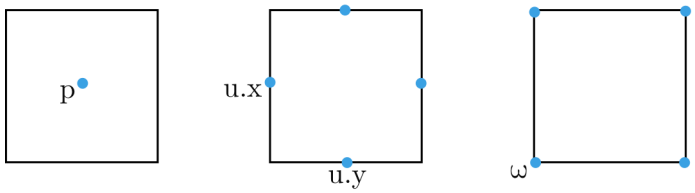

Fig. 2.5 – Example of centered, face and vertex staggering in Basilisk

One of the key strengths of Basilisk is his **Adaptative Mesh Refinement** (AMR): each cell adapts its size during the simulation in order to refine the mesh only in particular areas of the calculation domain. For example, it is useful for two-phase flows as most of the physics happens near the interface: the mesh is refined around the interface to capture all the phenomena and the rest of the domain is less refined to save some calculation time. As the mesh is adapted at each time step, the AMR allows to describe precisely a moving interface. For instance, the AMR is really useful to study a bubble bursting at the surface of a liquid, as it creates a jet that may break up and produce jet droplets [79]. In this case, the AMR allows to follow the ejected droplets precisely, as illustrated on Fig. 2.6. The interface between the liquid and the gas phase is refined with a high mesh level to capture the cavity collapse and the associated capillary waves. In our case, considering a sessile droplet evaporation, we need quite a big calculation domain regarding the actual size of the droplet: the domain has to be ten times bigger than the characteristic size of the droplet to avoid confinement effects. In this way, only a small part of our domain is interesting and the AMR offers a significant advantage.

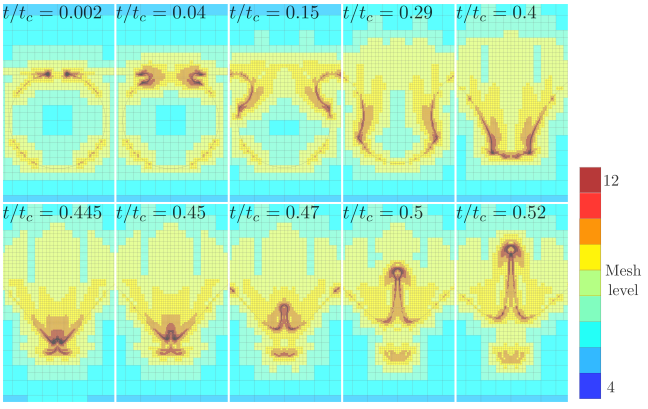

Fig. 2.6 – Example of the Adaptative Mesh Refinement in Basilisk for the case of a bursting bubble. At the initial time, the cavity formed by the bubble collapses and then a droplet is ejected. The AMR allows to use different mesh levels in each part of the computational domain, the most refined areas appear in red here. t_c is the capillary timescale. [79]

The AMR method is described in more details in the remainder of this paragraph. As each cell represents a volume control in the finite volume method of discretisation, these volumes have to be organized: they follow a **tree structure** called quatree in 2D (octree in 3D). Each cell of the mesh can be the parent of up to four other cells in 2D (eight in 3D). The level of a cell is defined by starting from zero for the root cell and by adding one every time a group of four descendant children is added (Fig. 2.7). As an input in Basilisk, the user can indicate three different levels for the mesh: the minimum level, the medium level and the maximum level that the cells can adopt during the simulation.
In order to simplify the calculation, some rules are established regarding the level of refinement for neighbouring cells. The direct neighbours and diagonally cells of a cell can not have more than one level difference with this cell. Besides, all the neighbouring cells of a mixed cell (a cell containing the interface) has to be at the same level. This is done to simplify the gradient and flux calculations. A refinement criteria has to be defined by the user (note that various refinement criteria can be implemented simultaneously). For example, the mesh can be refined near the interface, depending on a variable gradient or where the fluid velocity is important. The values of the variables have to be recalculated after refinement: for old cells, the values are calculated with the mean of the volume mass of smaller cells; for new cells, the values are calculated with a linear interpolation from the value of the parent cell.

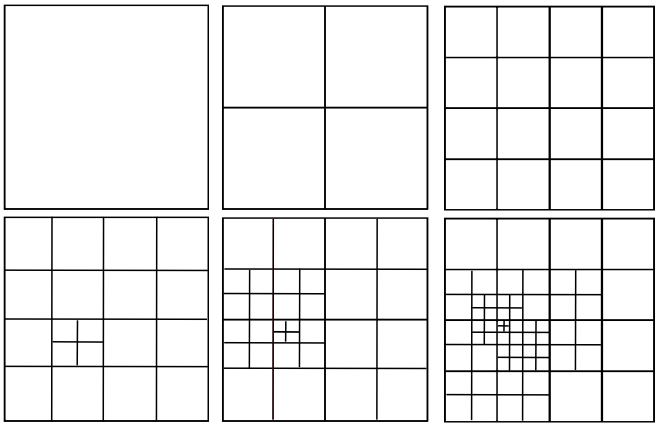

Fig. 2.7 – Example of the Adaptative Mesh Refinement in Basilisk. At first stage, only one cell is used to discretize to domain. Then, this cell is divided in 4 cells and again each cell is divided in 4 other cells according to the AMR method. Then, only a part of the domain is refined more precisely : neighbouring cells adapt their level of refinement to respect the rules of the AMR method.

2 Equations for the physical system

A droplet can be composed of a pure liquid or a mixture, as it is the case for a saline droplet. During the phase change, the liquid is transformed into vapor at the interface and then the vapor is diffused in the ambient air. In the whole domain, the flows are governed by the Navier-Stokes equations. Those are obtained according to the basic principles of mass and momentum conservation. Then, the convection-diffusion equation drives the transport of the vapor solvant in the gaseous environment and the transport of the solute inside the droplet. Finally, the evaporation, and thus the interface's retreat, are modelled with the Fick's law that corresponds to the outward evaporation mass flux along the interface .
The governing equations are presented in their integral form and their differential form as they can be both useful: the integral formulation is not very convenient for analytical work, but it is important for the finite-volume numerical methods that we use in this work. We consider only Newtonian and incompressible fluids.

2.1 Mass and momentum conservation

Mass conservation

It is a well-known fact that mass cannot be created or cannot vanished, it is the principle of mass conservation [74]. Therefore, if we consider a control volume V, fixed in space with a boundary noted S (Fig. 2.8), the mass inside this volume does not change in time, except if mass flows in or out through the volume boundary.

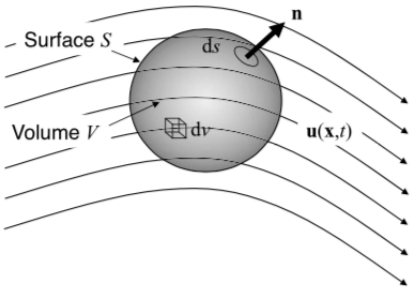

Fig. 2.8 – Example of a stationary control volume V. Figure reproduced from [74]

We can then define flows going in or out of V. For example, the flow out of V, through a surface element ds, is $\rho\mathbf{u}.\mathbf{n}ds$ with ρ the fluid density, $\mathbf{u}$ the velocity and $\mathbf{n}$ the outward normal to the surface S. Finally, we can write the principle of mass conservation, in integral form, as

$$\frac{\mathrm{d}}{\mathrm{d}t}\int_V \rho dv = -\oint_S \rho\mathbf{u}\cdot\mathbf{n}ds \tag{2.2}$$

where t is the time and dv is a volume element.
The left-hand side of the equation represents the rate of mass change in the volume and the right-hand side is the net flow through the boundary. From this, we can derive the local form for the **mass conservation**[1]

$$\frac{\partial\rho}{\partial t} + \overline{\nabla}\cdot(\rho\mathbf{u}) = 0 \tag{2.3}$$

1. We recall that $\overline{\nabla}$ is an operator used to express the gradient, the divergence and the rotationnal of a quantity. In three-dimensional Cartesian coordinate system, $\overline{\nabla} = (\frac{\partial}{\partial x}, \frac{\partial}{\partial y}, \frac{\partial}{\partial z})$

Momentum conservation

The principle of momentum conservation states that the rate of change of fluid momentum in the control volume V results of the difference in momentum across the boundary S and the net forces acting on the volume [74]. We write it in an integral form as

$$\frac{\mathrm{d}}{\mathrm{d}t}\int_V \rho\mathbf{u}dv = \oint_S \rho\mathbf{u}(\mathbf{u}\cdot\mathbf{n})ds + \int_V \mathbf{f}dv + \oint_S \mathbf{n}\cdot\mathbf{T}ds \tag{2.4}$$

where $\mathbf{f}$ is the force per unit volume, regularly the gravitationnal force or the surface tension and $\mathbf{T}$ is a symmetric stress tensor, representing the total surface force. The local form of the **momentum conservation** can also be derived

$$\frac{\partial\rho\mathbf{u}}{\partial t} = -\overline{\nabla}\cdot(\rho\mathbf{u}\mathbf{u}) + \mathbf{f} + \overline{\nabla}\cdot\mathbf{T} \tag{2.5}$$

The nonlinear advection term is equivalent to

$$\overline{\nabla}\cdot(\rho\mathbf{u}\mathbf{u}) = \rho\mathbf{u}\cdot\overline{\nabla}\mathbf{u} + \mathbf{u}\overline{\nabla}\cdot(\rho\mathbf{u}) \tag{2.6}$$

By using the definition of the substantial derivative and the continuity equation previously established, we rewrite Eq. 2.5 as the Cauchy's equation of motion

$$\rho\frac{D\mathbf{u}}{Dt} = \mathbf{f} + \overline{\nabla}\cdot\mathbf{T} \tag{2.7}$$

This relation is valid for any continuous medium. For Newtonian fluids, the stress $\mathbf{T}$ can be considered as a linear function of the rate of strain

$$\mathbf{T} = (-p + \lambda\overline{\nabla}\cdot\mathbf{u})\mathbf{I} + 2\mu\mathbf{S} \tag{2.8}$$

where p is the pressure, λ is the second coefficient of viscosity, $\mathbf{I}$ is the unit tensor, μ is the viscosity and $\mathbf{S}$ is the rate of strain (or deformation tensor). If we substitute the stress tensor relation (Eq. 2.8) into the Cauchy's equation (Eq. 2.7), we end up with the **Navier-Stokes equation** for the fluid flow

$$\rho\frac{D\mathbf{u}}{Dt} = \mathbf{f} - \overline{\nabla}p + \overline{\nabla}(\lambda\overline{\nabla}\cdot\mathbf{u}) + \overline{\nabla}\cdot(2\mu\mathbf{S}) \tag{2.9}$$

Incompressible flow

In fluid mechanics, incompressible flow refers to a flow in which the density of each fluid particle does not change as it moves. Therefore, the evolution of the density is

$$\frac{D\rho}{Dt} = \frac{\partial\rho}{\partial t} + \mathbf{u}\cdot\overline{\nabla}\rho = 0 \tag{2.10}$$

This reduces the mass conservation (Eq. 2.3) to

$$\overline{\nabla}\cdot\mathbf{u} = 0 \tag{2.11}$$

This equivalent statement implies that for an incompressible flow, **the divergence of the flow velocity is zero**. Another important point for incompressible flows is the role of the pressure. The pressure is determined by the velocity field and takes on any specific value needed to ensure the flow divergence free. That is the starting point for the numerical solutions

of the Navier-Stokes equations that we will detail later.
In addition for incompressible flows the energy equation does not need to be solved to find the velocity and the pressure, unless the properties are functions of temperature of course. Thus, we do not consider the energy conservation here.
Finally, **S**, the deformation tensor, can be expressed as

$$\mathbf{S} = \frac{1}{2}(\overline{\nabla}\mathbf{u} + \overline{\nabla}\mathbf{u}^T) \tag{2.12}$$

Thus, considering the incompressibility, and this expression of **S**, we rewrite the Navier-Stokes equation (Eq. 2.9) as

$$\rho\frac{D\mathbf{u}}{Dt} = -\overline{\nabla}p + \mathbf{f} + \overline{\nabla}\cdot\mu(\overline{\nabla}\mathbf{u} + \overline{\nabla}\mathbf{u}^{\mathrm{T}}) \tag{2.13}$$

In the following, we refer to the "Navier-Stokes equations" considering this equation and the mass conservation equation (Eq. 2.11).

Gravity

The term **f** in the Navier-Stokes equation (Eq. 2.13) usually includes the gravitationnal force $\rho\mathbf{g}$, where **g** is the gravitational acceleration. For the sessile problem, as explained in the previous Chapter 1, the gravity does not influence the shape of the droplet because the Bond number is small ($\mathrm{Bo} < 1$). So the gravitationnal forces are negligible compared to the surface tension forces. The gravity can affect the flows inside the droplet during evaporation. However, for pure liquids, like pure water that we consider in the first part of this study, there are no density gradient so the gravity has no impact on the flow dynamics. For saline droplet, there are density gradients because some areas are concentrated more than others in salt. But in these cases, the influence of the gravity is negligible compared to the Marangoni effect. The concentration and the surface tension gradients play a dominant role in the dynamics inside the droplet. Therefore, in the equations and then in the simulations **we neglect the gravity**.

Surface tension

We consider small sessile droplets where the surface tension dominates the gravity to determine the shape of the droplet. We deal with two phases separated by an interface. In this way, the surface tension is an important force in the problem and needs to be implemented in the model.
Intermolecular forces, such as van der Waals forces, cannot be calculated directly in the numerical model because of obvious high calculation costs. As they play a really important role at the interface, they are modelled with the surface tension γ (Fig. 2.9)

$$\mathbf{f}_\gamma\delta_I = \gamma\kappa\mathbf{n}\delta_I + \overline{\nabla}_S\gamma\delta_I \tag{2.14}$$

where δ_I is a dirac distribution at the interface, κ is the interface curvature and ∇_S, the surface gradient.
When we consider a curved interface, the surface tension induces a pressure jump across the interface, thus a stress normal to the interface. This corresponds to the first term of Eq. 2.14, called the **Laplace pressure** [26]. Changes in composition or temperature along the liquid interface also influence the surface tension. A composition or temperature gradient leads to a surface tension gradient, which constitutes a tangential stress at the interface called the **Marangoni contribution** [80]. This is the second term in Eq. 2.14.

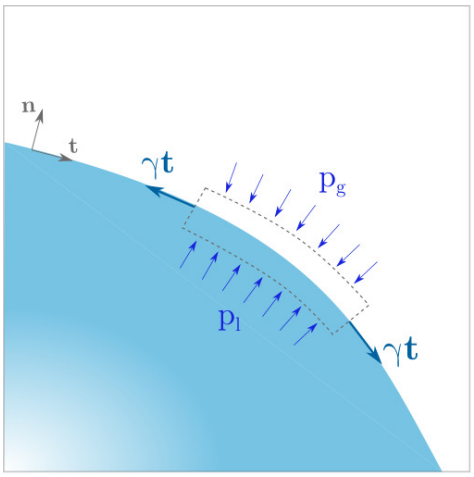

Fig. 2.9 – Surface tension balance on an element of a curved and heterogeneous interface. A normal stress called the displacement pressure (denoted p_g in gas and p_l in liquid) is generated by the curvature. A tangential stress called Marangoni stress applies due to gradients of surface tension related to variations in composition or temperature along the interface.

In the case of a pure droplet, there are no gradient of composition or temperature, so the surface tension is constant along the interface and the Marangoni stress term is equal to zero. We can then use the implementation already proposed in Basilisk for the surface tension that reduces to the Laplace pressure. For the evaporation of mixtures, such as saline droplet, the surface tension becomes non uniform along the interface as the salt concentration can be heterogeneous along the interface and thus the implementation of the surface tension needs to be modified in the code, the Marangoni contributation has to be taken into account.
We can replace **f** in Eq. 2.13. Finally, the **Navier-Stokes equation** is

$$\partial_t \mathbf{u} + \overline{\nabla}.(\mathbf{u} \otimes \mathbf{u}) = -\frac{1}{\rho}\overline{\nabla} p + \frac{\mu}{\rho}\overline{\nabla}.(\overline{\nabla}\mathbf{u} + (\overline{\nabla}\mathbf{u})^T) + \frac{1}{\rho}\left(\gamma\kappa\mathbf{n} + \overline{\nabla}_S\gamma\right)\delta_I \tag{2.15}$$

2.2 Equations for evaporation

Convection-diffusion equation

Evaporation is a process driven by a convection-diffusion equation. If there is a solute inside the droplet, its transport is also described by the same equation. The mass fraction of water vapor is transported in the gas phase and the mass fraction of solute, if there is one, is transported in the liquid phase

$$\partial_t c + \overline{\nabla} \cdot (c\mathbf{u}) = \overline{\nabla} \cdot (D_\mathrm{v}\overline{\nabla} c) \tag{2.16}$$

where c is the quantity to diffuse (either vapor concentration in air or solute concentration in liquid) and D_v is the diffusion coefficient specific to each specie to diffuse.
At first, we consider a pure liquid. There is no solute to transport in the droplet. The convection diffusion equation is only used to treat water vapor in the air. As explained before, we make the assumption that the evaporation is a **pure diffusive phenomena**. Therefore, we neglect the convection term in the previous equation and the following **diffusion equation** is used

$$\partial_t c = \overline{\nabla} \cdot (D_\mathrm{v}\overline{\nabla} c) \tag{2.17}$$

As the evaporation phenomenon is a **quasi-steady** process (see Chapter 1), the term on the left-hand side is negligible.

Evaporation flux and phase change

As evaporation is essentially determined by the diffusion of the solvent vapor in the gaseous phase [61, 62], the outward evaporation mass flux **J** is described by the first **Fick's law** [60]

$$\mathbf{J} = -D_{\mathrm{v}}\overline{\nabla}c \tag{2.18}$$

The evaporation rate is given by a mass balance at the interface and corresponds to the quantity of solvent that diffuses away.
We neglect convection in the transport of the vapor in the gas phase, therefore a pure diffusive evaporation velocity v_e which is the receding velocity of the interface is defined (Fig. 2.10). It is not a flow velocity, it is just the displacement of the interface due to the diffusion of the vapor away from the interface

$$\mathbf{v}_e \sim -\frac{1}{\rho_l}\mathbf{J} \tag{2.19}$$

We can rewrite the evaporation velocity in terms of relative humidity RH

$$\mathbf{v}_e \approx \mathrm{Pe_s D_v}\overline{\nabla}\mathrm{RH} \qquad \text{where} \quad \mathrm{RH} \approx \frac{\mathrm{c}_\infty}{\mathrm{c_s}} \quad \text{and} \quad \mathrm{Pe_s} \approx \frac{\mathrm{c_s}}{\rho_\mathrm{l}} \tag{2.20}$$

The scale of the **Peclet number** $\mathrm{Pe_s}$ is introduced here to compare the interface's retreat and the vapor diffusion (Eq. 1.13). This expression of the phase change velocity is calculated and used in the numerical code.

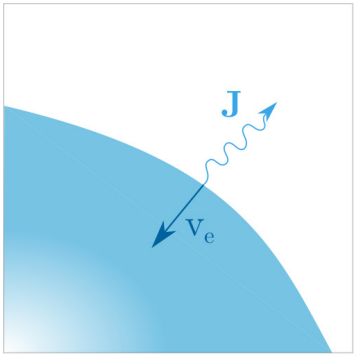

Fig. 2.10 – Evaporation flux **J** and the induced receding velocity of the interface v_e. The outward mass flux is determined by the diffusion, the convection is neglected.

In this balance, we assume a purely diffusive transport for the vapor and neglect convection. However, evaporation constitutes a **phase change**, the liquid is transformed into its own vapor. This induces a **velocity jump** at the interface and a **convective flux** in the gas phase, called the **Stefan flow** [40, 81].
The convection flux is due to the great variation of density between the liquid and its vapor: the liquid density is much greater than the vapor density. For instance, the density of water in liquid form ρ_l is about 1000 kg.m^{-3} while the density of water vapor ρ_v is about 1.6 kg.m^{-3}. The mass of liquid that evaporates is the same than the mass of vapor created (noted m), but because of the important density difference, the vapor volume V_{vapor} has to be bigger than the liquid volume V_{liquid}

$$\rho_\mathrm{v} = \frac{m}{V_\mathrm{vapor}} << \rho_\mathrm{l} = \frac{m}{V_\mathrm{liquid}} \tag{2.21}$$

This significant gaseous release creates an outward flow in the air surrounding the droplet, which is called the Stefan flow. This flow helps to transport the vapor away from the interface and therefore induces convection in the gas phase. In the range of parameters considered, the

contribution of Stefan currents for vapor transport is negligible [40]. Thus, the pure diffusion equation is a relevant choice for vapor transport in the gas phase. However, it is interesting to take into account the Stefan currents in the global calculation of the flows in the domain and thus during the calculation of the velocity field $\mathbf{u}$. The generation of an additional vapor volume due to the phase change results in a source term to be added in the basic conservation equations.

Mass transfert

There is a mass transfer at the interface as a portion of the liquid turns into vapor. A source term needs to be added in the equations. This transfer imposes a difference in velocity between the interface velocity and the velocity of the fluids in each phase (2.11). There is therefore a velocity jump at the interface which implies that the velocity field is not continuous.
The following calculation of velocity jump expression is detailled in the work of Malan [82]. We note $\mathbf{u}_I$ the velocity of the interface which differs from the liquid or gas velocities, $\mathbf{u}_l$ and $\mathbf{u}_g$ (and from the diffusive evaporation velocity $\mathbf{v}_e$ introduced before). The mass conservation writes in each separate phase volumes V_l and V_g (respectively of surfaces S_l and S_g)

$$\frac{\mathrm{d}}{\mathrm{d}t}\left(\int_{V_l}\rho_l\,dV\right)+\int_{S_l}\rho_l\left(\mathbf{u}_l\cdot\mathbf{n}\right)dS+\int_I\rho_l\left(\mathbf{u}_l-\mathbf{u}_I\right)\cdot\mathbf{n}_I\,dS=0 \tag{2.22}$$

$$\frac{\mathrm{d}}{\mathrm{d}t}\left(\int_{V_g}\rho_g\,dV\right)+\int_{S_g}\rho_g\left(\mathbf{u}_g\cdot\mathbf{n}\right)dS-\int_I\rho_g\left(\mathbf{u}_g-\mathbf{u}_I\right)\cdot\mathbf{n}_I\,dS=0 \tag{2.23}$$

where $\mathbf{n}$ is the external normal and $\mathbf{n}_I$ is the interface normal.
By summing the two previous equations, we can apply the mass conservation and we end up with a mass balance at the interface

$$\int_I\rho_l\left(\mathbf{u}_l-\mathbf{u}_I\right)\cdot\mathbf{n}_I\,dS=\int_I\rho_g\left(\mathbf{u}_g-\mathbf{u}_I\right)\cdot\mathbf{n}_I\,dS \tag{2.24}$$

The physical interpretation is that the total amount of mass traversing the interface from one phase equals the mass gained by the other. The mass transfer per unit area of interface is defined as

$$\dot{m}" = \rho_l(\mathbf{u}_l-\mathbf{u}_I)\cdot\mathbf{n}_I=\rho_g(\mathbf{u}_g-\mathbf{u}_I)\cdot\mathbf{n}_I \tag{2.25}$$

By eliminating $\mathbf{u}_I$, we obtain the velocity jump condition across the interface due to mass transfer

$$(\mathbf{u}_l-\mathbf{u}_g)\cdot\mathbf{n}_I=\dot{m}"\left(\frac{1}{\rho_l}-\frac{1}{\rho_g}\right) \tag{2.26}$$

This velocity jump corresponds to a source term that needs to be added when solving the Navier-Stokes equations in order to take into account the phase change. This way the Stefan currents are considered in the gas phase. This term remains very small and negligible under the considered evaporation conditions but can become preponderant under other conditions. Its calculation and implementation will be carried out in the numerical code which will allow to consider new applications where the Stefan currents are not negligible.

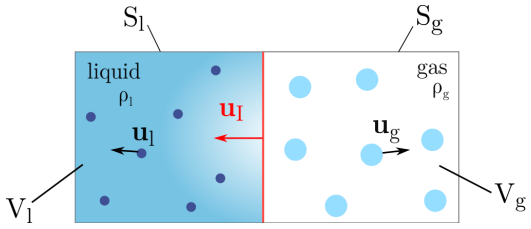

Fig. 2.11 – Mass conservation for a 1D case with phase change. It induces a velocity jump at the interface: the velocities of the liquid, gas and interface are different.

2.3 Boundary conditions

At the substrate

A critical point in numerical simulations of fluid flows is the correct implementation of the boundary conditions. For an incompressible and viscous flow, the fluid sticks to the wall boundary and thus the fluid velocity along this boundary is equal to the wall velocity

$$\mathbf{u} = \mathbf{U}_{\text{wall}} \tag{2.27}$$

This includes both the normal and the tangential components of the velocity. In a lot of cases, the wall boundary of the numerical domain are fixed so the fluid velocity at the wall is zero. For an inviscid flow, the fluid will slip on the wall as there are no viscous stresses: thus, only the normal component of the fluid velocity is equal to the wall normal velocity.
During the sessile droplet evaporation, the boundary conditions on the substrate depend on the evaporation mode

- for the unpinned mode, the triple contact line slips on the substrate. Therefore, only the normal component of the velocity is zero

$$\mathbf{u} \cdot \mathbf{n} = 0 \tag{2.28}$$

- for the pinned mode, the triple contact line is fixed on the substrate. Therefore, both the normal and the tangential components of the velocity are zero

$$\mathbf{u} = 0 \tag{2.29}$$

At the interface

We assume that the vapor is at equilibrium with the liquid. This is equivalent to a Dirichlet condition at the interface for the water vapor. The evaporation flux is only normal to the interface of the droplet. This adds a new boundary condition

$$c = c_s \tag{2.30}$$

where c is the concentration and c_s is the saturation concentration condition.

Far from the droplet

Far from the droplet, the vapor concentration equals the vapor condition for the relative humidity imposed by the user

$$c = c_\infty \tag{2.31}$$

where $c_\infty \approx RHc_s$ where RH is the relative humidity of the environment.
Besides, symmetrical conditions are imposed for the calculation domain walls. The length of the domain is ten times the droplet radius to make sure that there are no confinement effects.

All the equations

Mass conservation

$$\overline{\nabla} \cdot \mathbf{u} = 0$$

Momentum conservation

$$\partial_t \mathbf{u} + \overline{\nabla}.(\mathbf{u} \otimes \mathbf{u}) = -\frac{1}{\rho}\overline{\nabla} p + \frac{\mu}{\rho}\overline{\nabla}.(\overline{\nabla}\mathbf{u} + (\overline{\nabla}\mathbf{u})^T) + \frac{1}{\rho}\left(\gamma\kappa\mathbf{n} + \overline{\nabla}_S\gamma\right)\delta_I$$

Diffusion equation

$$\partial_t c = \overline{\nabla} \cdot (D_\mathrm{v}\overline{\nabla} c)$$

Evaporation flux

$$\mathbf{J} = -D_\mathrm{v}\overline{\nabla} c$$

Boundary conditions

- unpinned mode

$$\mathbf{u} \cdot \mathbf{n} = 0$$

- pinned mode

$$\mathbf{u} = 0$$

- at the interface

$$c = c_s$$

- far from the droplet

$$c = c_\infty$$

2.4 Numerical solutions for the equations

The continuous equations that govern the physical problem have to be transformed into discrete equations. This is a necessary approximation step for the future numerical resolution with Basilisk. We explain successively the spatial discretization and the integration in time of the Navier-Stokes and diffusion equations.

2.4.1 Spatial discretization

The discretization in space of the equations is done following the **finite volume approach** which provides conservative numerical schemes [72]. Thus the precision of the transport only depends on the scheme order and the mesh refinement. The finite volume method is used to numerically solve partial differential equations, such as the finite difference method and the finite element method. The partial differential equation is solved in an approximate way using a mesh of finite volumes which are small disjoint volumes in 3D (surfaces in 2D, segments in 1D) whose union constitutes the study domain. An example of control volume is illustrated on Fig. 2.12. We recall that a staggered grid is used in Basilisk so the variables are located at different points of the control volume. For instance, the pressure is defined at the center of the control volume whereas the velocity is defined on the faces. The finite volume and finite element methods use approximations of integrals. However, the finite volume method is based directly on the integral form of the equations presented in the previous paragraph (the so-called strong form of the equations) to be solved, while the finite element method is based on a variational formulation of the equation (also called weak formulation). We do not detail here the discretization of the Navier-Stokes equations or the diffusion equation since it is only a matter of following the classical finite volume method and writing the operators in a discrete way on the grid. More explanations can be found in [74].

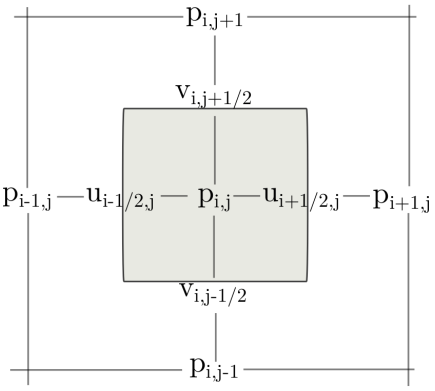

Fig. 2.12 – Example of a staggered grid where the pressure is defined at the center of each control volume. Each variable (pressure p, horizontal velocity components u and vertical velocity components v) are located on a separate grid.

2.4.2 Time integration

Navier-Stokes equations

We use the solver provided by Basilisk, based on a **CFL-limited timestep**, the **Bell-Collela-Glaz advection scheme**, and the **implicit viscosity solver**.
The time integration of the Navier-Stokes equations is detailled here as it is particular for incrompressible flows. For incompressible flows, the velocity field must have zero divergence according to the conservation of mass (Eq. 2.11). For incompressible flows, pressure plays a particular role since it is not considered as a thermodynamic function. The pressure is determined by the velocity field and takes any value allowing to satisfy the condition of a velocity field with zero divergence.

Thus two steps are followed

- prediction of the velocity field from the conservation equation by forgetting the pressure
- then, correction of this velocity field with the help of the pressure in order to make it divergence free.

This method of solving the Navier-Stokes equations is called the **projection method**. It was initially introduced by Chorin in 1968 [83]. Basilisk uses a second-order projection method based on the Bell-Collela-Glaz scheme [84] to discretize the non-linear advection term. However, to explain simply the principle of a projection method, we take here the example of a first-order method. The detailed implementation of the Bell-Collela-Glaz scheme can be found on the Basilisk website [85]. We now present the different steps of the projection method.

Using a first-order discretization, the momentum equation (Eq. 2.13) becomes

$$\frac{\mathbf{u}^{\mathrm{n}+1}-\mathbf{u}^{\mathrm{n}}}{\Delta t}+\mathbf{A}^{\mathrm{n}}=\frac{1}{\rho^{\mathrm{n}}}\left(-\overline{\nabla}p+\mathbf{D}^{\mathrm{n}}+\mathbf{f}^{\mathrm{n}}\right) \tag{2.32}$$

where p is the pressure, $\mathbf{A}=\overline{\nabla}\cdot(\mathbf{uu})$ is the advection term, $\mathbf{D}=\overline{\nabla}\cdot\mu(\overline{\nabla}\mathbf{u}+\overline{\nabla}\mathbf{u}^{\mathrm{T}})$ is the diffusion term and $\mathbf{f}$ denotes all other forces, such as gravity and surface tension. The superscript n denotes a quantity evaluated at the beginning of the time step and $n+1$ stands for the end of the time step.
According to the mass conservation (Eq. 2.11), the velocity at the end of the time step has to be divergence free

$$\overline{\nabla}\cdot\mathbf{u}^{\mathrm{n}+1}=0 \tag{2.33}$$

The **first predictor step** computes an intermediate velocity field $\boldsymbol{u}^*$ without taking into account the pressure term

$$\mathbf{u}^*=\mathbf{u}^{\mathrm{n}}+\Delta t\left(-\mathbf{A}^{\mathrm{n}}+\frac{1}{\rho^{\mathrm{n}}}\left(\mathbf{D}^{\mathrm{n}}+\mathbf{f}^{\mathrm{n}}\right)\right) \tag{2.34}$$

The non-linear advection term $\mathbf{A}$ is estimated with the Bell-Collela-Glaz scheme. Then, the **second correction step** uses the pressure gradient to find the velocity at the time step $n+1$

$$\frac{\mathbf{u}^{\mathrm{n}+1}-\mathbf{u}^*}{\Delta t}=-\frac{1}{\rho^n}\overline{\nabla}p \tag{2.35}$$

As there is no explicit equation for the pressure, we need to calculate the pressure such that the velocity at $n+1$ time step is divergence free. To do so, we take the divergence of Eq. 2.35

$$\overline{\nabla}\cdot\left(\frac{1}{\rho^{\mathrm{n}}}\overline{\nabla}p\right)=\frac{1}{\Delta t}(\overline{\nabla}\cdot\mathbf{u}^*-\overline{\nabla}\cdot\mathbf{u}^{\mathrm{n}+1}) \tag{2.36}$$

We want the divergence of $\overline{\nabla}\cdot\mathbf{u}$ to be zero so we end up with a **Poisson equation** for the pressure. Once the pressure is calculated, we can use it in Eq. 2.35 to find the projected velocity at time $n+1$

$$\boldsymbol{u}^{\mathrm{n}+1}=\boldsymbol{u}^*-\Delta t\frac{1}{\rho^{\mathrm{n}}}\overline{\nabla}p \tag{2.37}$$

This is first order projection method, which is adapted in Basilisk to make it a second-order predictor corrector method.
The source term corresponding to the contribution of the phase change modifies the mass

conservation equation as follows

$$\overline{\nabla} \cdot \mathbf{u} = \dot{m}" \left(\frac{1}{\rho_l} - \frac{1}{\rho_g} \right) \delta_I \tag{2.38}$$

where δ_I is the Dirac function used to indicate that the source term is localized at the interface. Thus there is an additionnal term in the following Poisson equation

$$\overline{\nabla} \cdot \left(\frac{1}{\rho^{\mathrm{n}}} \overline{\nabla} p \right) = \frac{1}{\Delta t} \left(\overline{\nabla} \cdot \mathbf{u}^* - \dot{m}" \left(\frac{1}{\rho_l} - \frac{1}{\rho_g} \right) \delta_I \right) \tag{2.39}$$

The technical implementation of this additionnal term linked to the phase change is detailled in the Chapter 3.

Diffusion equation

For the interface advection, we have to solve in a first time the diffusion equation given by Eq. (2.17). A **time-implicit backward Euler discretisation** is used, then the vapor concentration c at the time step $n+1$ is expressed as

$$c^{\mathrm{n}+1} = c^{\mathrm{n}} + \Delta t \overline{\nabla} \cdot (D_{\mathrm{v}} \overline{\nabla} c^{\mathrm{n}+1}) \tag{2.40}$$

This leads to a **Poisson-Helmholtz problem** for $c^{\mathrm{n}+1}$ with the following boundary conditions: the saturation vapor c_{s} at the interface and the vapor value at the computational domain limits at given relative humitidy H, $c_\infty = H c_{\mathrm{s}}$. The system of equations resulting is solved using a multigrid solver, already implemented in Basilisk.

Stability conditions

Explicit schemes for the transport of interfaces have to respect the following standard CFL condition [78]

$$\Delta t < \frac{\Delta}{|\mathbf{u}_{\max}|} \tag{2.41}$$

where Δ is the size of the cell.
The integration time step also has to respect the capillary timestep restriction [78]

$$\Delta t < \sqrt{\frac{\rho \Delta^3}{\gamma}} \tag{2.42}$$

3 Numerical model for evaporation

3.1 Scaling of the equations

In order to simplify the physical problem to solve, to highlight the dominant mechanisms and to fix the values of the input parameters in the numerical code, we must **scale the equations** that describe the dynamics of the system. Scaling means writing the system in a new set of variables in order to obtain a simpler representation of it. This allows to highlight characteristic properties of the system. The Basilisk code solves dimensionless equations which means that we have to enter dimensionless numerical parameters in the code. To find those numerical parameters, we need to scale the equations. The scaling emphasizes the **dimensionless numbers** that govern the physical problem and those numbers are used to define the dimensionless parameters of the code.
There are several methods and several steps to scale a problem. The most important is to find and explain the quantities that allow to pass the variables of the dimensioned system in the scaled system (and conversely). These quantities are called here the **scales of the problem** and are essential to compare the numerical results in the scaled system with the experimental results in the original system of units. The scales of the problem are used to write the dimensionless equations of the problem.

Scales

The parameters for the evaporation problem are the initial droplet radius r_0, the diffusion coefficient for water vapor in air D_v, the densities for water and air, respectively ρ_l and ρ_a, the viscosities for water and air, respectively μ_l and μ_a, the surface tension between water and air γ, the vapor saturation condition at the interface c_s, and the vapor condition far from the droplet c_∞.
The natural and obvious **length scale** d_c of this system is the initial radius of the droplet, as it is the only length parameter, thus

$$d_\mathrm{c} = r_0 \tag{2.43}$$

For the **time scale** t_c, as evaporation is considered a pure diffusive problem, we build a diffusive time with the initial radius of the droplet and the diffusive coefficient. The time scale is defined as

$$t_\mathrm{c} = r_0^2/D_\mathrm{v} \tag{2.44}$$

From these two scales, we deduce the **velocity scale** v_c

$$v_\mathrm{c} = D_\mathrm{v}/r_0 \tag{2.45}$$

Evaporation is driven by the vapor concentration gradient $c_\mathrm{s} - c_\infty$. Thus, we decide to non-dimensionnalize the vapor concentration conditions by c_s, as only the gradient between them is important. We end up with $c_\mathrm{s} = 1$ at the droplet interface and $c_\infty \in [0; 1]$, depending on the relative humidity considered. By convention, the notation is $a = a_\mathrm{c}\overline{a}$ where a is the variable in the original system of units, a_c is the scale corresponding to a and $\overline{a}$ is the variable in the scaled system. In order to obtain the non-dimensionnalized equations, each variable is replaced with the corresponding scale.

Diffusion equation

The pure diffusion equation is

$$\partial_t c = D_\mathrm{v} \overline{\nabla}^2 c \tag{2.46}$$

To write the non-dimensionalization in the classic system of unities of the experiments, we use the scales derived before to obtain

$$\frac{c_\mathrm{s}}{t_\mathrm{c}} \partial_{\overline{t}} \overline{c} = \frac{D_\mathrm{v} c_\mathrm{s}}{r_0^2} \overline{\nabla}^2 \overline{c} \tag{2.47}$$

By multiplying by $t_\mathrm{c}/c_\mathrm{s}$, the equation becomes

$$\partial_{\overline{t}} \overline{c} = \frac{D_\mathrm{v} t_\mathrm{c}}{r_0^2} \overline{\nabla}^2 \overline{c} \tag{2.48}$$

If we replace t_c, we obtain the non-dimensionnalized diffusion equation

$$\partial_{\overline{t}} \overline{c} = \overline{\nabla}^2 \overline{c} \tag{2.49}$$

Navier-Stokes equations

The Navier-Stokes equation is

$$\partial_t \mathbf{u} + \overline{\nabla}.(\mathbf{u} \otimes \mathbf{u}) = -\frac{1}{\rho} \overline{\nabla} p + \frac{\mu}{\rho} \overline{\nabla}.(\overline{\nabla}\mathbf{u} + (\overline{\nabla}\mathbf{u})^T) + \frac{1}{\rho} \gamma \kappa \delta_I \mathbf{n} + \frac{1}{\rho} \overline{\nabla}_S \gamma \delta_I \tag{2.50}$$

We introduce a typical pressure p_c and write the non-dimensionalization

$$\frac{v_\mathrm{c}}{t_\mathrm{c}} \partial_t \overline{\mathbf{u}} + \frac{v_\mathrm{c}^2}{r_0} \overline{\nabla}.(\overline{\mathbf{u}} \otimes \overline{\mathbf{u}}) = -\frac{p_\mathrm{c}}{\rho r_0} \overline{\nabla} \overline{p} + \frac{\mu v_\mathrm{c}}{\rho r_0^2} \overline{\nabla}.(\overline{\nabla}\overline{\mathbf{u}} + (\overline{\nabla}\overline{\mathbf{u}})^T) + \frac{1}{\rho r_0^2} \left[\gamma \overline{\kappa} \mathbf{n} + \overline{\nabla}_S \gamma\right] \overline{\delta_I} \tag{2.51}$$

Multiplying by $t_\mathrm{c}/v_\mathrm{c}$ gives

$$\partial_t \overline{\mathbf{u}} + \overline{\nabla}.(\overline{\mathbf{u}} \otimes \overline{\mathbf{u}}) = -\frac{p_\mathrm{c} t_\mathrm{c}}{\rho r_0 v_\mathrm{c}} \overline{\nabla} \overline{p} + \frac{\mu t_\mathrm{c}}{\rho r_0^2} \overline{\nabla}.(\overline{\nabla}\overline{\mathbf{u}} + (\overline{\nabla}\overline{\mathbf{u}})^T) + \frac{t_\mathrm{c}}{\rho r_0^2 v_\mathrm{c}} \left[\gamma \overline{\kappa} \mathbf{n} + \overline{\nabla}_S \gamma\right] \overline{\delta_I} \tag{2.52}$$

t_c is replaced to obtain

$$\partial_t \overline{\mathbf{u}} + \overline{\nabla}.(\overline{\mathbf{u}} \otimes \overline{\mathbf{u}}) = -\frac{p_\mathrm{c}}{\rho v_\mathrm{c}^2} \overline{\nabla} \overline{p} + \frac{\mu}{\rho r_0 v_\mathrm{c}} \overline{\nabla}.(\overline{\nabla}\overline{\mathbf{u}} + (\overline{\nabla}\overline{\mathbf{u}})^T) + \frac{\gamma}{\rho r_0 v_\mathrm{c}^2} \left[\gamma \overline{\kappa} \mathbf{n} + \overline{\nabla}_S \gamma\right] \overline{\delta_I} \tag{2.53}$$

Two dimensionless numbers can be identified, the Reynolds number Re, and the capillary number Ca, calculated here with the density and the viscosity of the liquid

$$Re = \frac{\rho_l r_0 v_\mathrm{c}}{\nu} \qquad Ca = \frac{v_\mathrm{c} \mu}{\gamma} \tag{2.54}$$

For the pressure term, we choose the typical pressure $p_\mathrm{c} = \rho v_\mathrm{c}^2$ which leads to

$$\partial_t \overline{\mathbf{u}} + \overline{\nabla}.(\overline{\mathbf{u}} \otimes \overline{\mathbf{u}}) = -\overline{\nabla} \overline{p} + \frac{1}{Re} \overline{\nabla}.(\overline{\nabla}\overline{\mathbf{u}} + (\overline{\nabla}\overline{\mathbf{u}})^T) + \frac{1}{Re} \frac{1}{Ca} \left[\gamma \overline{\kappa} \mathbf{n} + \overline{\nabla}_S \gamma\right] \overline{\delta_I} \tag{2.55}$$

The scaling of the equations highlights that the evaporation problem depends on two dimensionless numbers, the **Reynolds number** and the **capillary number**. The Reynolds number Re represents the ratio of inertial forces to viscous forces. In water, $Re \approx 20$ which

allows us to conclude that the inertial forces slightly dominate the viscous forces. The capillary number Ca represents the ratio of the viscous forces to the surface tension. We have $Ca \approx 10^{-4}$ which clearly shows that the surface tension dominates the viscosity in the problem.

To complete the scaling, according to the Π theorem we need to identify additional dimensionless numbers [86]. As nine physical parameters govern the problem (r_0, D_v, ρ_l, ρ_g, μ_l, μ_g, γ, c_s, c_∞) $9 - 3 = 6$ dimensionless numbers are needed. The Reynolds number, the capillar number and the scale of the Peclet number have already been introduced and are relevant to describe the physics of the problem. Quite naturally, the **viscosity ratio** μ_g/μ_l and the **density ratio** ρ_g/ρ_l impose themselves as dimensionless numbers. Finally, the last dimensionless number is formed with the vapor conditions of the problem, to obtain a **vapor ratio** c_∞/c_s.
These six dimensionless numbers govern the evaporation problem (Fig. 2.13) and allow to fix the numerical parameters of the computational code. The dimensionless numbers put forward allow to describe the physics of the problem in a simplified way, taking into account the dominant phenomena. These numbers are calculated with the dimensioned parameters of the problem. They must have the same value in the numerical code (or if they were calculated with the dimensionless parameters) and in reality: this ensures that the code correctly reproduces the physics of the problem. For this purpose, dimensionless numbers are used to fix the values of several scaled parameters of the numerical code.

Dimensionless numbers			
Reynolds number	$Re = \dfrac{\rho\, v_\mathrm{c}\, r_0}{\mu}$	Viscosity ratio	$\dfrac{\rho_\mathrm{g}}{\rho_\mathrm{l}}$
Capillary number	$Ca = \dfrac{\mu_\mathrm{l}\, v_\mathrm{c}}{\gamma}$	Density ratio	$\dfrac{\mu_\mathrm{g}}{\mu_\mathrm{l}}$
Peclet number	$Pe_\mathrm{s} \approx \dfrac{c_\mathrm{s}}{\rho_\mathrm{l}}$	Vapor ratio	$\dfrac{c_\infty}{c_\mathrm{s}}$

Fig. 2.13 – Sum-up of the dimensionless numbers that describe the evaporation problem. These numbers are used to define the numerical parameters.

3.2 Numerical parameters for evaporation

To define the numerical parameters, we proceed by term by term identification between the dimensionless equation (Eq. 2.55) and the classical Navier-Stokes equation (Eq. 2.15). The dimensionless numbers and scales of the problem established and calculated previously are used. The numerical parameters are therefore scaled but they check the correct values of the dimensionless numbers which ensures the physical consistency of the code.
According to the Π theorem [86], three parameters can be fixed to 1 according to the dimensionless numbers previously calculated. We choose to impose

$$r_0 = 1 \qquad D_v = 1 \qquad c_s = 1 \tag{2.56}$$

This is also coherent with the scales of the problem defined earlier.

Density and viscosity

By identification, the factor in front of the pressure term is equal to 1 which means that the density of the liquid can be taken equal to 1 in the numerical code. The density of the gas is then determined with the density ratio.

$$\rho_l = 1 \qquad \text{and} \qquad \rho_\mathrm{g} = 1 \times \frac{\rho_\mathrm{g}}{\rho_\mathrm{l}} \tag{2.57}$$

The viscous term in the non-dimensionnal Navier-Stokes equation has the factor $1/Re$, which means that the viscous term is of the order of 10^{-1}. This term is identified with the factor in front of the viscous term in the Navier-Stokes equation (Eq. 2.15).

$$\frac{\mu_l}{\rho_l} \approx \frac{1}{Re} \tag{2.58}$$

As $\rho_l = 1$, the viscosities in the code are

$$\mu_l = \frac{1}{Re} \qquad \text{and} \qquad \mu_\mathrm{g} = \frac{1}{\mathrm{Re}} \times \frac{\mu_\mathrm{g}}{\mu_\mathrm{l}} \tag{2.59}$$

Surface tension

In the range of the parameters considered, the Reynolds number is of the order of 10^1 and the Capillary number is of the order of 10^{-4}. This implies that the surface tension has to be of the order of the coefficient in front of the surface tension term in the dimensionless equation

$$\gamma \approx \frac{1}{Re}\frac{1}{Ca} \approx 10^{-3} \tag{2.60}$$

This is a very small value for the numerical code as it imposes a very small timestep to satisfy the capillary timestep restriction (Eq. 2.42). This leads to huge calculation costs. But **the surface tension does not play a role in the flow** or in the displacement velocity of the interface. The surface tension only allows to maintain the interface in the spherical-cap shape. We can show that if we relax the surface tension in the code to 1, or even 10^{-2} for some cases, there is no significant impact on the evaporation dynamics[2]. This allows a less restrictive condition for the capillary timestep, and thus faster numerical calculations. In the following simulations, we thus take 1 for the surface tension without losses of physical insights.

Vapor condition

The last numerical parameter to fix is the vapor condition far from the droplet c_∞. The vapor ratio and the numerical value of $c_s = 1$ are used to determine

$$c_\infty = 1 \times \frac{c_\infty}{c_s} \tag{2.61}$$

The vapor ratio has to be calculated and adaptated depending on the value of the relative humidity chosen for the simulation. For instance, if the relative humidity $RH = 20\%$ then

2. For a numerical test case of a sessile droplet evaporating in the unpinned mode with $\theta = 90°$ and $RH = 0\%$, the mean squared error between two reconstructed interfaces with $\gamma = 10$ or $\gamma = 1$ is of the order of 10^{-12}, with a maximum error of 10^{-5} in the region of the contact angle. This is coherent as it is a sensible zone for the reconstruction of the interface.

the vapor ratio is equal to 0.2, which means that $c_\infty = 0.2$ in the numerical code.

Peclet number

In the code, we decide to fix the Peclet number to 10^{-3} and not to 10^{-5} which is the theoretical value. This allows to increase the dynamics of the evaporation phenomenon. This is physically coherent with the evaporation dynamics as it ensures that the diffusion dominates the convection. This increases the evaporation phenomenon by a factor of the order of 10^2 that we have to take into account when comparing the experimental and the numerical results. The numerical time has to be multiplied by this Peclet factor in addition of the time scale of the problem to recover the physical time.

What to remember ?

This chapter introduces the numerical tool that will be used in this work, the open source software Basilisk. Its numerous advantages for the study of two phase flows make it relevant for the study of the evaporation of sessile droplets. The solvers already implemented for the Navier-Stokes and diffusion equations can be used to solve the flows involved in evaporation. Consideration of the phase change taking place at the interface has been added to accurately describe the mass transfer between the liquid and the gas phase. An evaporation velocity is calculated in the code thanks to the Peclet number, the diffusion coefficient of the vapor and the concentration gradient of water vapor. This velocity defines the interface's retreat.
The study of the parameters has brought to the fore the dimensionless numbers that govern the physical problem. This allows to make the link between the continuous equations of the problem and the discrete and scaled equations of the numerical model. The time, space and velocity scales that will allow the comparison of the numerical results with the experimental results have been established.
The action of gravity and viscous forces are negligible compared to the surface tension. The surface tension plays an important role in maintaining the spherical cap shape of the droplet but does not play any role in the hydrodynamics and the internal or external flows.

3 Experimental study for the evaporation of pure water sessile droplets

A series of experiments on the evaporation of pure water droplets is performed in order to validate and compare the results of the numerical model built with Basilisk,. This first set of experiments also allows to test the set-up and to improve it for the second experimental study which will follow on the evaporation of saline droplets. This chapter presents a description of the experimental set-up, an explanation of the data processing methods employed and an analysis of the results obtained.
The experimental setup is designed to study the evolution of the geometrical features of the droplet over time, such as the radius, the height or the contact angle. The experiments take place in a humidity reduced box which allows to control the ambient relative humidity during the evaporation. The material and the surface state of the substrate are selected to ensure that the droplet evaporates in a single mode for the entire duration of the experiment, the pinned mode. the initial volume of the drop is also controlled by using a micropipette to deposit it. The experimental protocol and the method used to analyze the data are described respectively in the first and second sections.
Parametric studies are performed by varying one by one these control parameters to study their relative influence. The experimental results are presented and discussed in the third section.

The experimental results presented in this chapter were obtained as part of the internship of Anaelle Givaudan and Paul Boumendil, undergraduate students at Sorbonne University in 2020/2021.

Contents

1 Experimental set-up and protocol

The experiment consists in evaporating a pure water sessile drop in a controlled environment. Fig. 3.1 shows a schematic illustration of the experimental setup for observing the evaporation process of sessile droplets.
A sessile droplet evaporates inside a laboratory **glove box** of 250 L under **controlled humidity** provided by W-Tech, illustrated on Fig. 3.2. Two adjustable dryer-humidifier modules are present in the box. The box is airtight and made of 100 % PMMA. The relative humidity RH ranges from 5% to 50%, and the temperature inside the box is the ambient temperature of the room, $T \approx 25.0°C$. The relative humidity and the temperature are continuously measured with a probe integrated in the glove box to verify that they remain constant throughout each experiment. We also assume that the air surrounding the droplet is at rest as long as the typical size of the glove box, around 1 m, is much larger than the droplet typical length, the radius, around 10^{-3} m. We can then neglect the convective flows effects on the evaporation behavior of the sessile droplet.

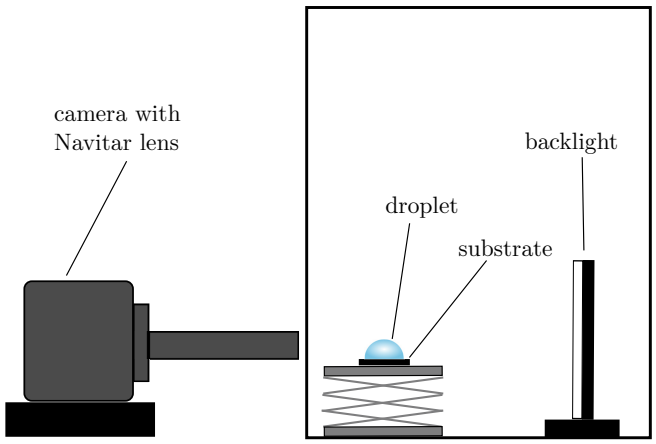

Fig. 3.1 – Schematic illustration of the experimental set-up for the study of the evaporation of pure water sessile droplets. The droplet is deposited onto a substrate made of copper inside a glove box under controlled humidity. A camera records side view photos from outside the box.

The sessile droplet is deposited onto a solid substrate with a **single channel micropipette** (model VE100, VWR Signature Ergonomic High-Performance Pipettor, volumes from 10 μL to 100 μL). The pipette is used with disposable polypropylene tips to be added at the end of the pipette. The liquid is taken in these tips. It is thus necessary to change the tips regularly, between each experiment, and in particular when the liquid is modified.
Different substrates were tested: aluminum, copper and silicon wafer. They have different surface states, which led the droplet to evaporate in different evaporation modes. We aim to have the droplets evaporate in a single evaporation mode for the entire duration of the experiment, for simplicity in analyzing the results and for comparison with numerical simulations. For the experiments, it appears that the unpinned mode is complicated to obtain with pure water droplets: indeed, the slightest surface irregularity or dust would modify the dynamics of the triple line and change the evaporation mode. For the pinned mode, it is enough to take a relatively rough substrate so that the triple line is trapped from the beginning of the experiment and this until complete evaporation. For these reasons, we choose to evaporate the pure water droplets on a **copper substrate**, which presents a sufficiently rough surface condition to guarantee evaporation only in the pinned mode. The copper substrate is 6 cm

long, 6.5 cm large and 3 cm thick. It is at room temperature. The same substrate is used for all the experiments, the surface is cleaned between the experiments with acetone to avoid the contamination by dust.
The liquid studied here is pure water, distilled water from the lab. We choose distilled water to ensure a simple study case with an uniform surface tension along the interface.

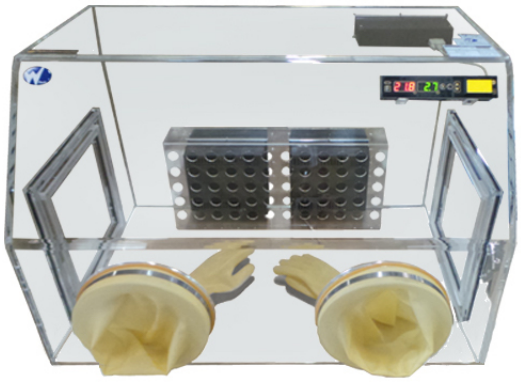

Fig. 3.2 – Laboratory glove box from W-Tech, with humidity controlled. Source: W-Tech website [87]

The evaporation dynamics is recorded from the side with a **Nikon D810 camera** equipped with Navitar lens recording images every 15 or 30 seconds (Fig. 3.3a). As the evaporation is a slow process, we do not need to reduce more the time interval between the pictures to capture all the dynamics: only at the very end of evaporation, it could be interesting to investigate more precisely the behavior as it remains largely misunderstood. In order to obtain high quality photos, the set-up is illuminated from the side with a back light. This also creates some light reflections on the droplet surface, which appear as white spots on the following photos. This has no influence on the quality of the photos. To ensure the focalisation of the camera, we placed the camera outside the box. Thus, the PMMA wall of the box can alter the quality of the images. Another disadvantage is the fact that the side view does not enable to verify precisely if the droplet is spherical: for this, we need a top view. This will be improve for the second experimental set-up, that will be introduced later for the experiments with saline droplets.

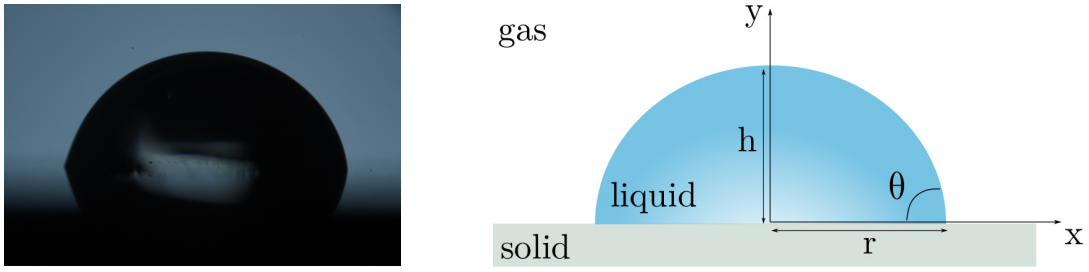

(a) (b)

Fig. 3.3 – (a) Example of a side view of an evaporating pure water sessile droplet on a copper substrate ($V_0 = 10\,\mu$L and $RH = 10\%$). (b) The scheme presents the variables r, h and θ that are measured during the evaporation of the droplet.

This set-up, with a side view, allows to measure the contact radius, r, the contact angle, θ and the height of the droplet, h, through the experiment (Fig. 3.3b). This way the evaporation dynamics of the droplet as function of the initial volume and the relative humidity can be analyzed. The experimental results will be used to validate the numerical model.

2 Data analysis

The experiments allow to collect a certain amount of photos that then has to be analyzed. Experimental data must be post-processed in order to get the interesting observable quantities to qualify the evaporation dynamics, namely the radius r, the height h and the contact angle θ of the drop over time. The post-processing of the photos is done in two steps with two tools, **ImageJ** and **Python**. In the following, we detail each of these steps.
The experimental data are affected by uncertainties that must be taken into account when analyzing the data and in particular if we want to compare these data with theoretical results or other data from the literature.

2.1 Images post-processing

ImageJ

First, ImageJ allows to process the raw photos (Fig. 3.4). Thanks to the lighting of the experimental set-up and in particular to the backlight placed behind the droplet, the droplet appears clearly in black on the photos. The copper substrate also appears in black at the bottom of the photo.

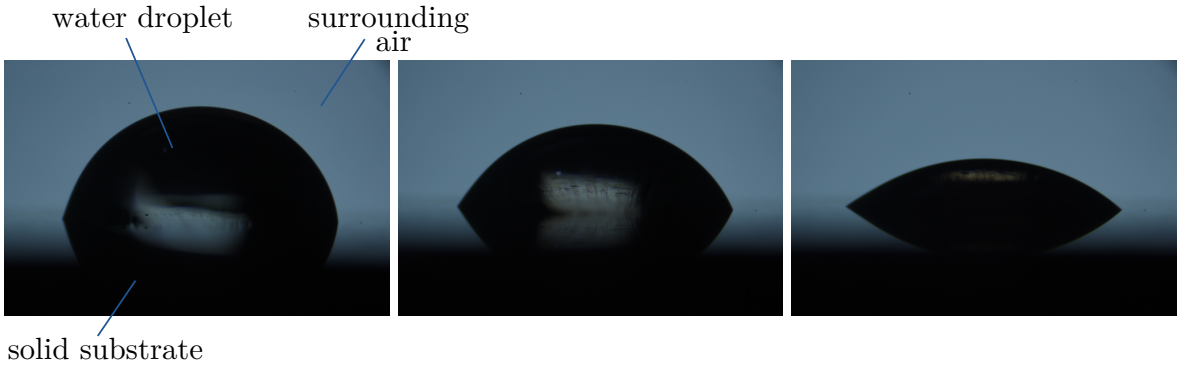

Fig. 3.4 – Example of raw photos of a pinned pure water droplet at different times of the evaporation ($V_0 = 10\,\mu$L and $RH = 10\%$). The droplet and the solid substrate appear in black and the surrounding air in grey.

The droplet is reflected in the substrate, which requires a careful analysis of the photos to replace the surface line of the substrate on the images. The photos are cropped with ImageJ in order to keep only the droplet and not to make the substrate appear on the photos.
The contrast on the images between the droplet and the background allows to detect the interface of the drop and thus to follow it over time. By adjusting the contrast of the pictures, the detection of the interface is facilitated since at the interface a very sudden jump appears in the color scale. Finally, we obtain a photo in black and white only, where the liquid appears in black and the external air in white (Fig. 3.5a). Each pixel of the photo is then equal to 0 (white) or 255 (black). The interface is located between the last black pixel and the first white pixel, as presented on Fig. 3.5b. This allows an efficient detection of the interface, but with an uncertainty that will be quantified in the next section. The photos are then converted into csv files with a subroutine.

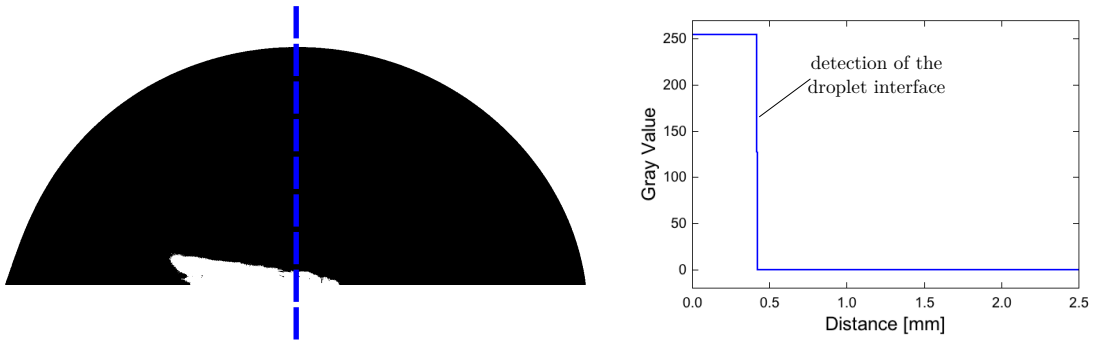

(a) (b)

Fig. 3.5 – Interface detection with ImageJ. (a) Photo of a droplet after the post-processing step with ImageJ. The droplet appears in black and the surrounding air in white ($V_0 = 10\,\mu$L and $RH = 10\%$). The white spot at the bottom of the droplet is a light reflection which has no impact on the interface detection. (b) Gray value as function of the distance along the blue axis showed in (a). The significant jump in the gray value allows to detect the position of the droplet interface.

Python

In order to analyze the experimental results, we developped a Python code to efficiently and reliably analyze the side-view photos. ImageJ creates a series of csv files. Each file corresponds to a photo and contains the value of each pixel of the photo. Python and the Matplotlib library are used to convert these csv files into matrices of 0 and 255. A matrix corresponds to a photo and therefore to a given time of the experiment.
The matrices are then exploited with a Python image processing routine. This code adapted to pinned sessile droplets gives the evolution of the geometric features of the droplet over time.
The interface of the droplet is detected by identifying the passage from 0 to 255 in the matrix and this over time, to have the evolution of the interface over time. By identifying the highest point of the interface, the height of the droplet is determined and the position of the triple contact line is recovered. Since we only consider evaporation cases in the pinned mode, the position of the triple line does not change over time. Once the interface is detected, it is reconstructed and compared to the experimental pictures in order to check the good accuracy. As illustrated on Fig. 3.6, the reconstructed interface by Python fits perfectly with the experimental photos.
To follow the evolution of the contact angle over time, the reconstructed interface is approximated by a line equation.

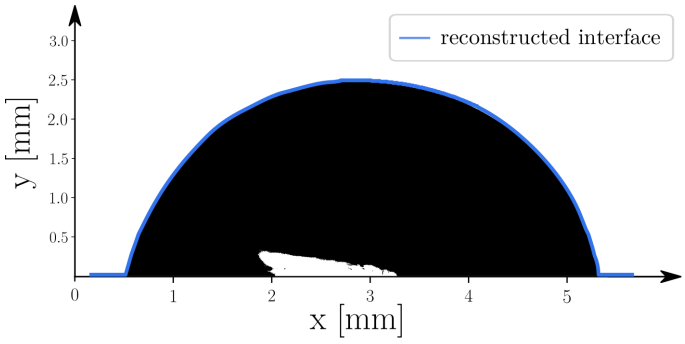

Fig. 3.6 – Comparison of the reconstructed interface performed by the Python image processing routines and the original photo of the droplet for the initial state of the droplet ($V_0 = 10\,\mu$L and $RH = 10\%$).

2.2 Measurement uncertainties

There are several sources of uncertainty in the experimental protocol and also in the post-processing of the data.
The first source of uncertainty concerns the micropipette used to control the initial volume of the drop. According to the manufacturer, the error on the volume is ± 1.6 % for a volume of 10 μL. The error then varies if the volume is increased: for a volume of 50 μL, the error decreases to ± 0.8 %. This ensures a precise measure of the volume and thus a high confidence in the experimental protocol. But the use of the pipette itself can be a source of uncertainty since the handling is delicate and must be extremely meticulous when working with drops with very small volumes, only a few microliters. Liquid can remain trapped in the pipette tip and thus distort the initial volume value desired. This uncertainty is difficult to quantify and is neglected in this study.
A second source of uncertainty appears during the post-processing step, in the image analysis performed with Python. The interface is detected thanks to the value of the pixels as explained in the previous paragraph. The distance error can be determined by drawing a plot profile on Image J as shown in Fig. 3.7a. Zooming on the significant jump showed at Fig. 3.5b, we observe that it has a certain thickness which constitutes an uncertainty for the position of the interface. It corresponds to an error of the order of $\delta = \pm 0.003$ mm, that needs to be taken into account for the measure of the geometrical features of the droplet, such as the height, the contact radius, the contact angle or the volume.

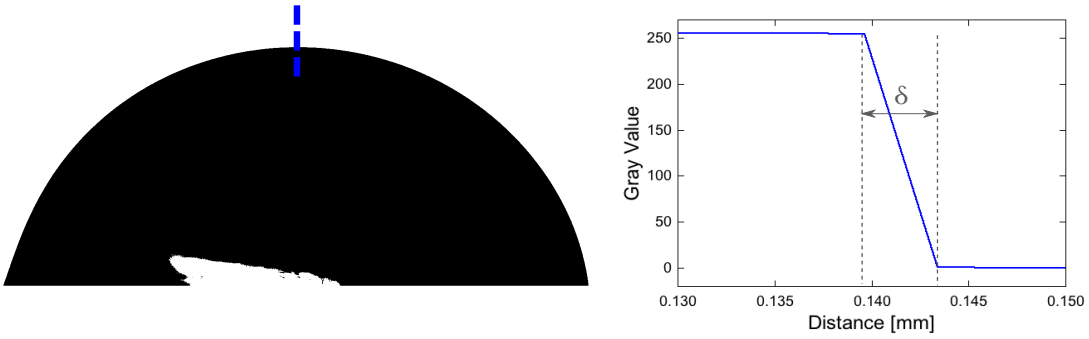

(a) (b)

Fig. 3.7 – Mesurement uncertainties from the image post-processing with Image J ($V_0 = 10\,\mu$L and $RH = 10\%$). (a) A plot profile is drawn across the interface. (b) The larger of the jump in the gray value is the error δ.

This error remains negligible compared to the measured quantities. It represents an error of about 1 % on the droplet radius which is acceptable and allows to have reliable results. In the following we choose not to display the error bars on the graphs because they are confused with the measurement points in most cases. This choice allows to gain in readability on the graphs.

The uncertainty regarding the contact angle is related to the error on the distances since the angle measurement depends on the reconstruction of the interface. The error on the angle can be calculated and is $\delta = \pm 1.7°$. It is therefore negligible in the range of angle values studied.

3 Results

The experimental results concerning the evaporation of pure water drops are presented in this section. Before detailing each of the parametric studies and comparing the different cases, we present in detail an example of experimental case to study the evolution of each of the measured variables. These experiments have already been done in the past by other authors. With this experimental work, the aim is not to demonstrate a particular behavior of the droplet in evaporation but rather to see if the experimental set-up that we have implemented allows to reproduce the correct evaporation dynamics by comparing with previously established laws and other experimental data.

3.1 Analysis of a basic case study

In the experiment presented in this paragraph, the relative humidity is 10%, the temperature is the ambient temperature of the laboratory and the initial volume of the droplet is 42 μL. We study step by step the experimental results measured by the Python image analysis method detailed in the previous section.
From the photos taken over time, the temporal variation of the interface of the droplet is recovered. Fig. 3.8 shows five images of the evaporating after a post-processing on Image J, for times $t = 0, 10, 20, 30, 40$ min.

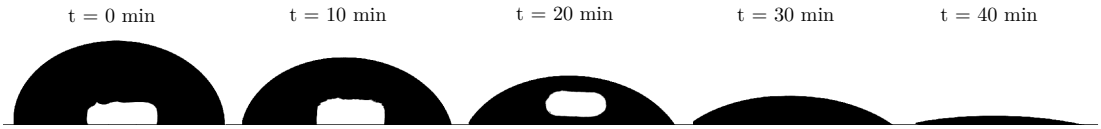

Fig. 3.8 – Images of a droplet evaporating in air, with an initial volume of 42 μL with a relative humidity equals to 10% for times $t = 0, 10, 20, 30, 40$ min.

On the images, the contrasts have been strengthened to better distinguish the drop. The drop appears black and the air around it appears white, which helps to detect the interface by identifying the pixel corresponding to the color jump as shown in Fig. 3.7b. The white spot that appears in the drop is a reflection of the lamp that illuminates our experimental set-up on the curved surface of the drop. This does not affect the image analysis and the results that follow since we are mainly interested in the interface of the drop. From the images, the evolution in time of the interface is deduced (Fig. 3.9).

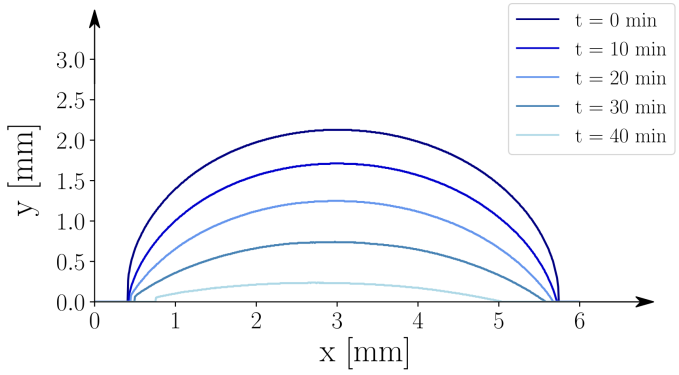

Fig. 3.9 – Interface reconstructed with Python along time t for a droplet evaporating in air, with an initial volume of 42 μL with a relative humidity equals to 10%.

We assumed that the droplet remains a **spherical-cap** during the whole evaporation, and this hypothesis is validated looking at Fig. 3.9. At the very end of the experiment, the interface appears less symmetrical, as the droplet becomes very small. The droplet sometimes switches to the unpinned mode at the very end of evaporation (Fig. 3.9) which disturbs the measurement of the geometric parameters of the droplet.
The radius of the droplet r is constant in time as long as the droplet evaporates in the pinned mode. We use the initial radius r_0 measured on the first picture as reference. The height $h(t)$ and the contact angle $\theta(t)$ of the droplet over time are presented in Fig. 3.10.

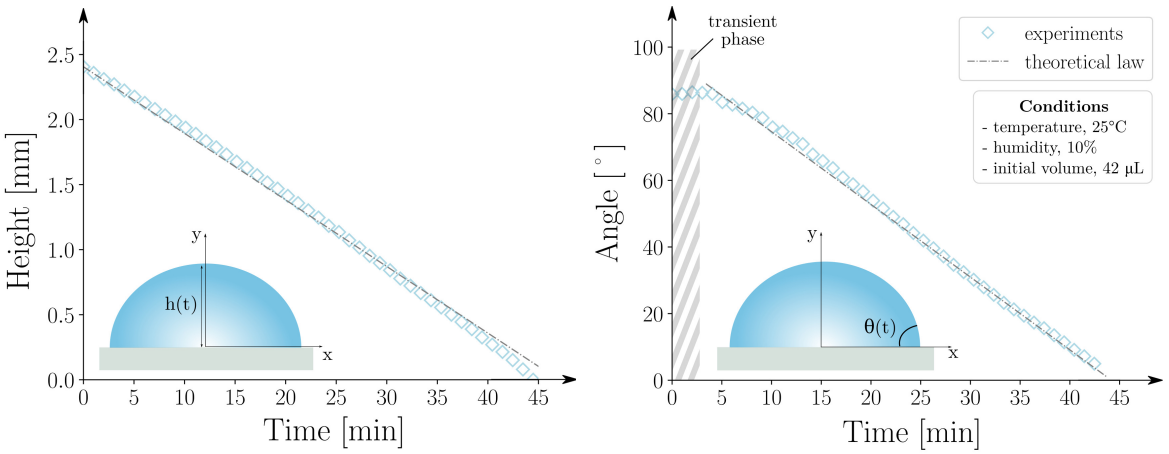

(a) (b)

Fig. 3.10 – Experimental results (blue markers) for a pure water droplet evaporating on a copper substrate in the pinned mode of evaporation. The height (a) and the contact angle (b) are compared with theoretical laws (dashed-dotted line).

The initial height h_0 is 2.5 mm and then h decreases linearly in time (Fig. 3.10a). As the droplet evaporates in the pinned mode, the time evolution of the contact angle $\theta(t)$ is a relevant parameter to study (Fig. 3.10b). The measure of the contact angle can be quite challenging at the end of evaporation when it becomes really small. The initial contact angle θ_0 is equal to 83°: it remains constant for a few minutes and then starts to decrease linearly. This suggests that the transient equilibrium phase was not completely over when we started recording the images. When the droplet is deposited onto the solid substrate, the sessile droplet spreads towards its equilibrium shape [38]. This transient phase is described in the litterature and usually takes less than a minute [37]. After that we can consider that the droplet has reached a quasi-steady state condition from a macroscopic point of view. We only wait a few seconds after deposition before taking photos of the droplet so this transient phase may be captured in the contact angle measurements. The transient phase is short and has little impact on the overall shape of the droplet, which is why it is only observed for the contact angle because it is a sensitive quantity.
The dynamics behavior of the height and the contact angle for an evaporating droplet in pinned mode is described by the following theoretical laws [40]

$$\begin{cases} h(t) = h_0(1 - t/t_F) \\ \theta(t) = \theta_0(1 - t/t_F) \end{cases} \tag{3.1}$$

where t_F is the final time of evaporation. This is valid as long as the droplet shape is a spherical-cap and if the contact angle is smaller than 90°. The experimental results are com-

pared with these laws (Fig. 3.10), and an excellent agreement is observed for both the height and the contact angle evolutions.

From the measurements of the height and the initial contact radius, the volume of the droplet is calculated at each time according to the geometrical relations 1.5. Fig. 3.11 shows the evolution in time of the droplet volume. A linear decrease is obtained again coherent with a theoretical law [40]

$$V(t) = V_0(1 - t/t_F) \tag{3.2}$$

The linear behavior is characteristic of the pinned evaporation mode. Physically, a linear profile is consistent since the driver of evaporation is the water vapor concentration gradient between the droplet interface and the relative humidity of the droplet environment. During the whole experiment, the relative humidity in the experimental set-up is kept constant by the humidifier/dryer modules. Thus, the concentration gradient is constant over time and therefore the evaporation rate remains the same. This linear dynamic is expected for the pinned evaporation mode. We will see in Chapter 4 that a different dynamic characterizes the unpinned evaporation mode.
This behavior is observed in several experimental and numerical works for different liquids and different substrates [37, 50, 51, 65, 88]. This allows to validate the experimental protocol as well as the obtained results. As a reminder, the aim of this work is twofold. On the one hand, it allows to build an experimental database on the evaporation of pure water droplets to validate the numerical model built on Basilisk (see Chapter 4). On the other hand, it prepares the setting up of an experimental device for the study of the evaporation of salty water droplets.
In order to complete the understanding of the evaporation dynamics, parametric studies are done where the initial volume and the relative humidity are modified.

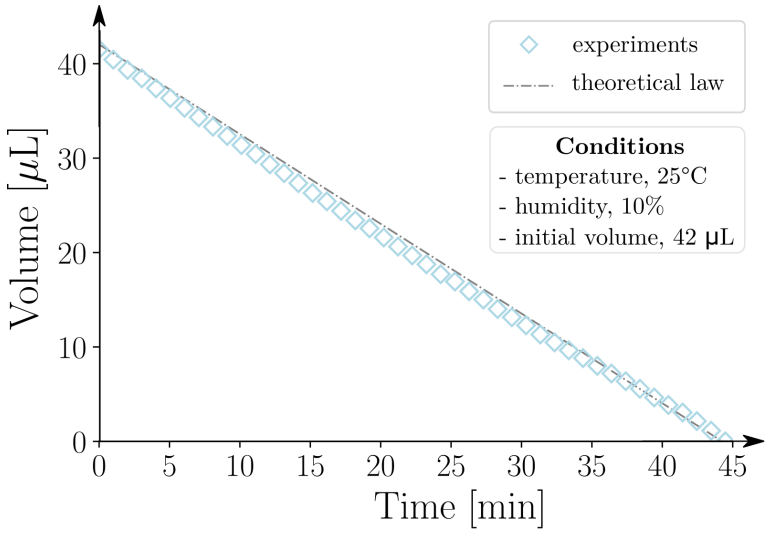

Fig. 3.11 – Experimental volume (blue markers) as a function of time for a droplet evaporating in air. The results are compared with a theoretical law (dashed-dotted line).

3.2 Variation of the initial volume

The goal of this part is to study the influence of the initial volume on the evaporation dynamics. The initial volume of the droplet V_0 is varied for a constant relative humidity equals to 10%. We performed experiments, with **three different volumes** between 26 and 42 μL. The informations relative to these experiments are presented in Table 3.1, in particular the geometrical features of the droplet at the beginning of each experiment.

V_0 (μL)	r_0 (mm)	h_0 (mm)	θ_0 (°)	t_F (min)	Bo
26	2.52	2.12	90.13	34.5	0.73
33	2.86	2.15	80.45	35	0.84
42	3.01	2.41	85.88	45	0.99

Tab. 3.1 – Characteristic lengths with variation of the initial drop volume V_0.

As the initial droplet volume increases, the initial radius r_0 and the initial height h_0 also increase. This means that the droplet spreads more on the substrate. The initial contact angle is not supposed to be influenced by the volume augmentation, as the angle only depends on the surface tension between the liquid and the substrate [49]. The contact angle varies between 80 and 90 °, the value is very sensitive to the local aspect of the material surface. The place of the droplet over the copper substrate is not exactly always the same. This can explain the differences in the measures of the initial contact angle.
When the droplet becomes larger, its Bond number Bo increases, which means that the effects of gravity increase. However the Bond number stays lower or very close to 1, which means that the spherical cap approximation is still valid. The surface tension remains the dominant force that controls the droplet shape.

From the pictures taken during the evaporation of the droplet, we follow the evolution of the height and the contact angle over time for each initial volume tested (Fig. 3.12). The left graph shows the height as a function of time (Fig. 3.12a) and the right graph shows the contact angle as a function of time (Fig. 3.12b).

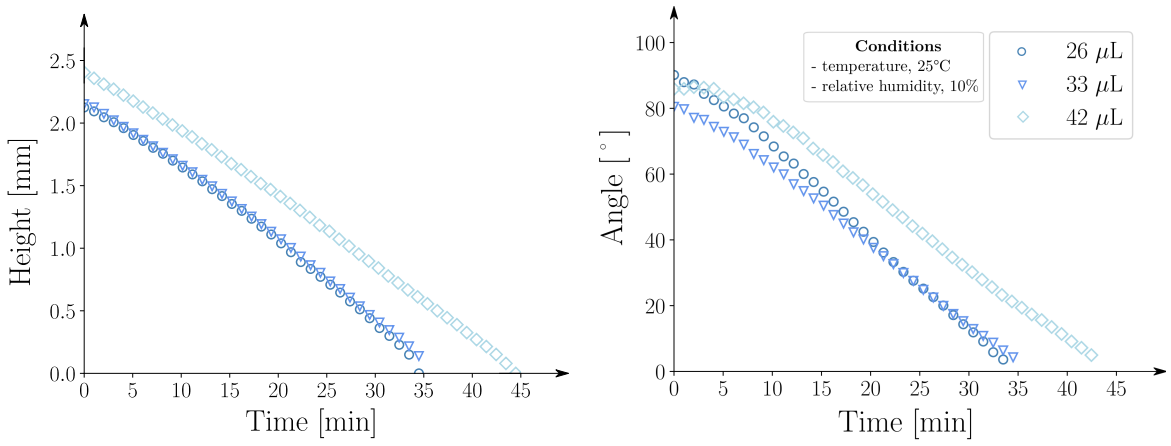

(a) (b)

Fig. 3.12 – Heights (a) and contact angles (b) for pure water droplets evaporating on a copper substrate in the pinned mode of evaporation with different initial volumes.

The height and the contact angle **decrease linearly in time** according to the theoretical laws (Eq. 3.1). The height evolution curves for the cases where the initial volume is equal to 26 and 33 μL are practically merged since the initial heights are identical (Fig. 3.12a). However, they do not have the same initial radius since the volume is different. The case where $V_0 = 26\,\mu$L shows a slightly faster evaporation which is consistent. We observe again and in particular for the case where $V_0 = 42\,\mu$L that the contact angle presents a first phase globally constant at the very beginning of the evaporation (Fig. 3.12b). This phase lasts a few minutes before observing a linear decrease of the contact angle.

We compute the volume for each experiment, according to Eq. 1.5. Fig. 3.13 shows the temporal evolution of volume. All curves follow the linear decrease predicted by the theory. A droplet with a higher initial volume takes more time to evaporate which seems quite intuitive. Regarding the final time of evaporation for the droplets of 26 and 33 μL, there is not a great difference. The difference of 10° in the initial contact angles may explain this. Indeed, in the case of pinned evaporation, it has been shown in the literature that the evaporation rate is globally constant during evaporation, the rate only decreases slightly and gradually [50]. However, the evaporation rate varies with the contact angle: as the contact angle increases, the overall evaporation rate decreases [88]. Since the case where $V_0 = 26\,\mu$L has a lower contact angle then its evaporation rate is globally lower which explains why its evaporation time is close to that of a larger droplet.

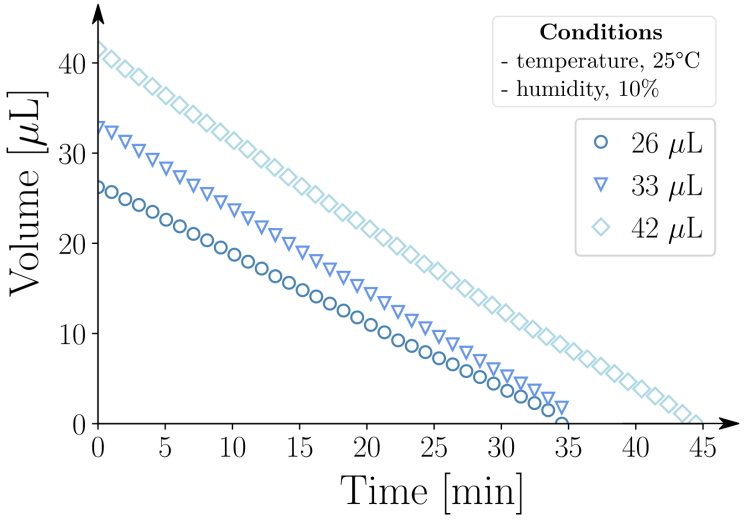

Fig. 3.13 – Droplet volumes as functions of time. Three cases are comparend to analyze the influence of the initial volume on the evaporation dynamics.

Fig. 3.14 presents the normalized volume V/V_0 as a function of the normalized time t/t_F. We normalize to be able to compare the evaporation dynamics without taking into account the initial parameters of each experiment. This allows to simplify the analysis of the physical problem and to highlight the characteristic properties of a system.
All the curves for the different initial volumes merge according the same linear law. Thus, it is well demonstrated that the characteristic behavior of evaporation in the pinned mode follows a linear decay dynamics. The initial volume affects the evaporation rate and the total evaporation time but not the linear dynamics.

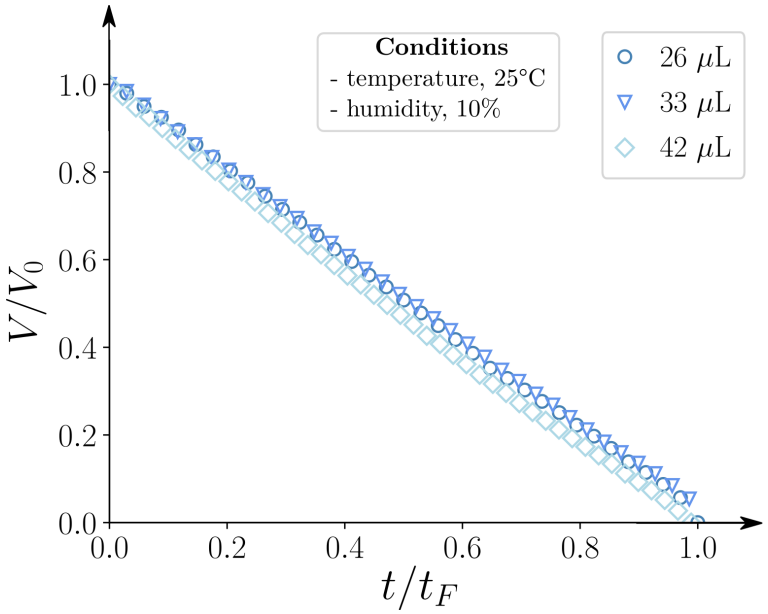

Fig. 3.14 – Scaled volumes V/V_0 as functions of the scaled time t/t_F for different initial volumes.

3.3 Variation of the relative humidity

The relative humidity of the environment in which the droplet evaporates is changed. The variation of the relative humidity modifies the vapor concentration gradient which drives the evaporation process. Thus, we expect to observe a slower evaporation as the relative humidity increases.
The experimental system allows to test relative humidities RH between 5% and 50%. **Three different humidities**, 10, 20 and 30 % are tested and the evolutions of the height and the contact angle of the droplet over time are measured. For each experiment a droplet of 25 μL of pure water is deposited in order to observe the influence of the relative humidity on the evaporation dynamics only. Table 3.2 presents the geometrical features of each droplet. We can note some differences especially for the initial volume which are due to the experimental uncertainties that depend on the user when depositing the droplet and also to the uncertainties related to the micropipette and the image analysis method.

RH (%)	r_0 (mm)	h_0 (mm)	θ_0 (°)	V_0	t_F (min)	Bo
10	2.52	2.12	90.13	26.0	42.5	0.73
20	2.45	2.04	83.28	23.5	48.0	0.69
30	2.42	2.09	86.15	23.8	61.0	0.69

Tab. 3.2 – Characteristic lengths with variation of the relative humidity RH.

The height $h(t)$ and the contact angle $\theta(t)$ of the droplet **decrease linearly in time**, as illustrated on Fig. 3.15. The height decreases linearly with time for the three humidities studied. It can be seen that as the relative humidity increases, the evaporation time increases. This reflects the expected effect of humidity on the evaporation rate [50]. As observed previously, the decrease of the contact angle is quite slow at the very beginning of the evaporation, meaning that the droplet has not find yet its equilibrium position.

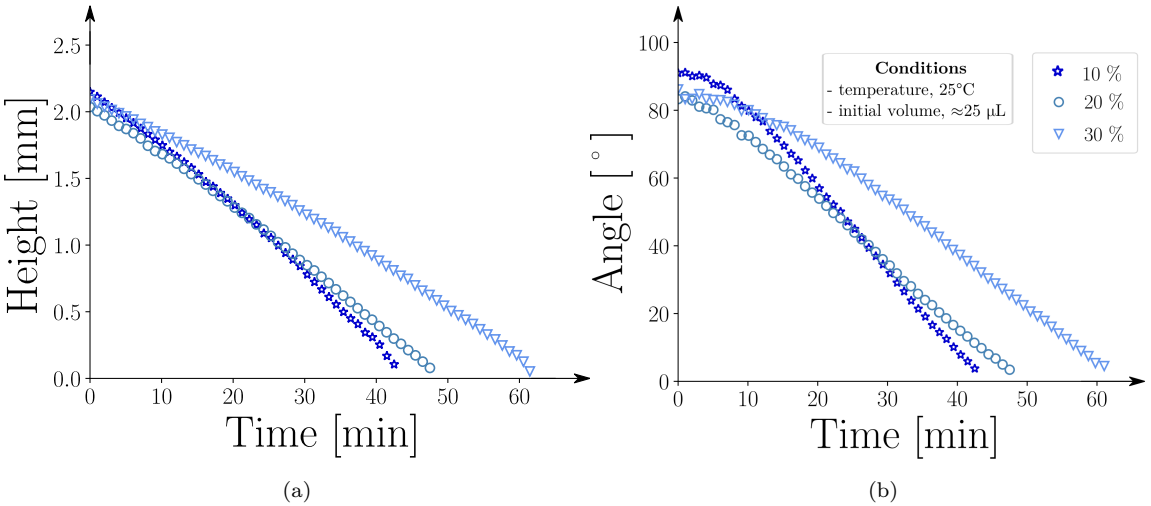

Fig. 3.15 – Heights (a) and contact angles (b) for pure water droplets evaporating on a copper substrate in the pinned mode of evaporation with different relative humidities.

The volume over time is calculated for each humidity tested. The volume is scaled by the initial volume V_0 corresponding to each case in order to compare the influence of the relative humidity (Fig. 3.16). We find the linear decreasing evolution of the volume predicted by the theoretical laws of the literature and a clear variation of the total evaporation time with the relative humidity. As the relative humidity increases, the total evaporation time increases: from about 43 minutes for the case $RH = 10\%$ to 61 minutes for the case $RH = 30\%$. This result seems quite intuitive, a dry environment leads to faster evaporation. When the relative humidity of the environment in which the drop is located increases, it becomes more and more saturated in vapor concentration. The phase change of water molecules into water vapor is reduced since the vapor concentration gradient decreases and evaporation is a diffusion limited process. The dynamics of evaporation decreases with the relative humidity.

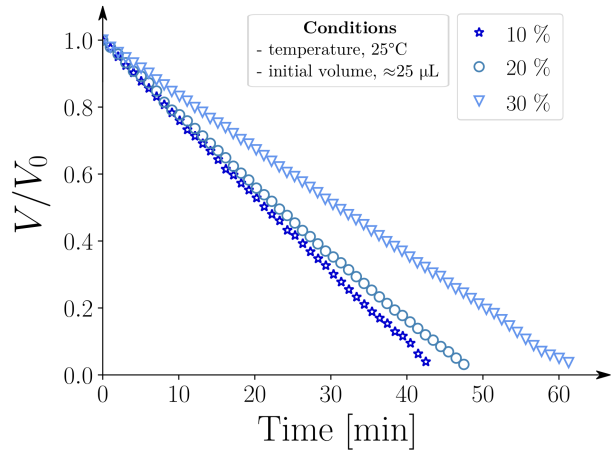

Fig. 3.16 – Evolution of the droplet volume as function of time for different relative humidities. The volume V is scaled by the initial volume V_0.

To go further in the conclusions and in the influence of relative humidity, we plot the scaled volume V/V_0 as a function of the time scaled by the final experimental time t/t_F. Fig. 3.17 highlights a unique behavior for the evaporation dynamics, independent of the chosen relative humidity. The evaporation dynamics follows a linear decay which is the typical behavior for a sessile droplet in the pinned evaporation mode.

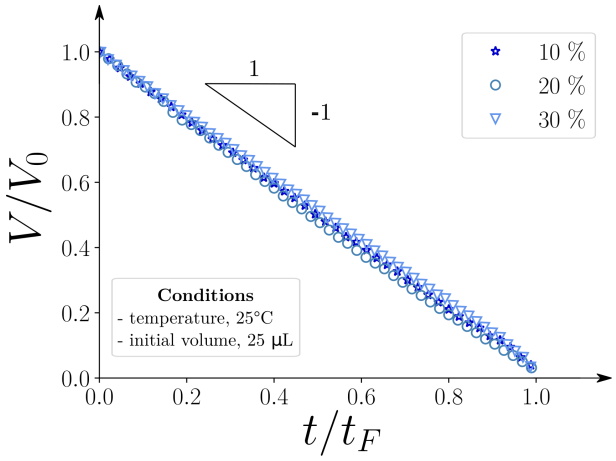

Fig. 3.17 – Scaled volumes as functions of the scaled time for different relative humidities.

What to remember ?

In this chapter, the first experimental study performed during this work is detailled. The aim is to set up an experimental device and a protocol, which can then be reused for a second experimental study on salt water droplets (see Chapter 5). This study also allows to collect experimental data which will be useful for the validation of the numerical code developed in the framework of this work (see Chapter 4).
This study concerns the analysis of the evaporation dynamics of sessile droplets of pure water. The droplets are deposited on a copper substrate whose surface condition allows a triple line pinning and thus a complete evaporation in the pinned mode.
The analysis of the droplet shape over time and the monitoring of the interface allow to validate the spherical cap hypothesis. The height and contact angle of the droplet show a linear decreasing evolution with time, which is consistent with the theoretical laws found in the literature. The volume of the droplet as a function of time also presents a linear decrease which is the expected characteristic behavior for droplets evaporating in the pinned mode. The evaporation rate is constant as the driving force of evaporation, the vapor concentration gradient, is constant during the experiment. The comparison with theoretical laws allows to confirm the experimental results which can then be used to validate the numerical model.
The experimental setup allows the variation of two control parameters: the relative humidity and the initial drop volume. The two parametric studies highlight again the linear evaporation dynamics independently of the relative humidity or the initial volume. An increase in the initial volume of the drop or in the relative humidity of the environment has an impact on the total evaporation time since it slows down the evaporation process and therefore lengthens the evaporation time.

4 Numerical simulations of evaporating pure water droplets

This chapter presents the results of the simulations performed for pure water droplets with the free-software Basilisk earlier introduced. The experimental data obtained in the previous chapter are used to validate the model.
The starting point of this work is the study of a spherical droplet evaporating in air as it is a case well described in the literature. To study the case of a sessile droplet, this first case has been modified.
In the second part, the new numerical implementations that have been made to enrich the model are detailed. Evaporation is a phase change which gives rise to a mass transfer at the interface: this has been implemented in the model in order to describe the physics of the problem as accurately as possible. Two distinct evaporation modes are studied in this work: the unpinned mode, i.e. with a radius that decreases with time while the contact angle remains fixed and the pinned mode, i.e. with a fixed contact radius during time while the contact angle decreases. The pinned mode requires a condition of anchoring the triple line during the entire evaporation time. The implementation of this condition is detailed.
Finally, in the last two parts, numerical results for the unpinned and pinned modes are presented and discussed. The relative humidity and the contact angle are both varied along the simulations to analyze their respective influence on the evaporation dynamics.

Contents

1 Spherical droplet

Before considering sessile drops, we consider the case of a **spherical drop** evaporating in an environment at rest where the relative humidity and the temperature are controlled. This case, simpler and perfectly symmetrical, serves as a test case for the numerical model of evaporation (Fig. 4.1). In 1877, Maxwell was interested in this problem for the study of drops forming an aerosol [61]. Then many authors used his findings for the study of sessile drops [88–90].

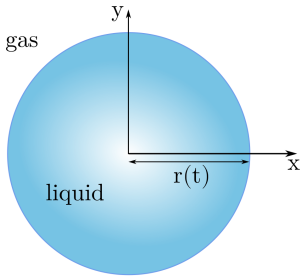

Fig. 4.1 – Spherical droplet of pure liquid. We follow the evolution in time of the droplet radius r(t). Its dynamics is described with the d^2 law.

For a spherical drop evaporating in an atmosphere at rest, the evolution of the radius is described by the d^2 law as follows [61]

$$r^2(t) = r_0^2 - \frac{2D_v}{\rho_l}(c_s - c_\infty)\, t \tag{4.1}$$

where r_0 is the initial contact radius, D_v is the diffusion coefficient of water vapor in air, ρ_l is the density of the liquid, c_s is the vapor saturation condition at the droplet interface and c_∞ is the vapor condition far from the droplet. The variable t_F is the time at which the droplet has completely evaporated. This results in $r(t_F) = 0$. Then, the d^2 law gives

$$r^2(t_F) = r_0^2 - \frac{2D_v}{\rho_l}(c_s - c_\infty)t_F = 0 \tag{4.2}$$

$$\Leftrightarrow r_0^2 = \frac{2D_v}{\rho_l}(c_s - c_\infty)\, t_F \tag{4.3}$$

By replacing this expression of r_0^2 in the d^2 law

$$r^2(t) = \frac{2D_v}{\rho_l}(c_s - c_\infty)(t_F - t) \tag{4.4}$$

Then finally

$$r(t) \propto \sqrt{t_F - t} \tag{4.5}$$

This theory can be written in a more general form where the evaporation dynamics of a spherical droplet in an infinite medium is described by a **power law** where y is the exponent of the law

$$r(t) \propto (t_F - t)^y \tag{4.6}$$

In the case of a drop evaporating in air in an infinite domain, the exponent y is equal to 0.5 [61]. With the Basilisk software, we can simulate the evaporation of a spherical droplet in the air. The numerical results will be compared with the theoretical law of d^2 in order to see if the model correctly reproduces the expected dynamics.

First, we analyze the vapor field around the droplet during evaporation. In the presented case, the relative humidity far from is equal to 20% and the initial volume is $V_0 = 10\,\mu$L. The field is presented for a time $t = 12$ s so just after the beginning of the evaporation process (Fig. 4.2). The evaporation takes about 20 minutes. The vapor concentration isolines form concentric circles around the droplet and the vapor concentration decreases as one moves away from the droplet, until reaching the boundary condition on the edges of the field. This means that the evaporation is uniform around the droplet: the numerical model reliably reproduces the diffusion of the vapor in the gas phase.

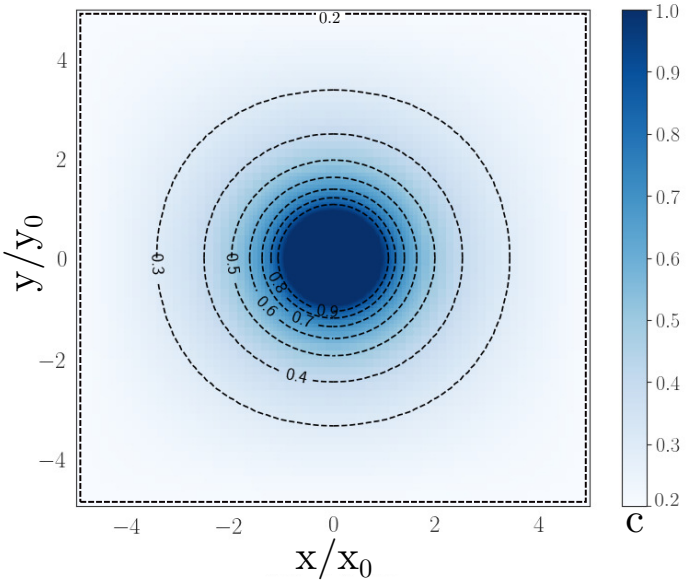

Fig. 4.2 – Vapor field around a spherical droplet evaporating in air at $t = 12$ s. The vapor concentration inside the droplet and at the droplet interface is the saturation condition $c_s = 1$ and the vapor concentration at the calculation domain boundaries is the condition representing the relative humidity of the environment far from the droplet $c_\infty = 0.2$. The dashed lines represent the isovalues of vapor.

Then, we plot the radius as a function of time (Fig. 4.3a). The radius is scaled by the initial radius r_0 and the time by the final time t_F in order to represent a general case, independent of the conditions of the experiment. This allows to reduce the d^2 law (Eq. 4.1) to an expression that no longer depends on the parameters of the liquid or the environment

$$\frac{r}{r_0} = \left(1 - \frac{t}{t_F}\right)^y \tag{4.7}$$

where y should be equal to 0.5 according to the theory. Therefore, the radius is plotted as a function of $1 - t/t_F$. A loglog scale is then used to analyze the power behavior. Fig. 4.3b shows that the data align according to a linear law, whose slope is $y = 0.57$. This means that **the dynamics of the radius follows the power law** described by Maxwell [61] as the exponent found is close to 0.5 (Eq. 4.7). The numerical model correctly reproduces the behavior of a spherical droplet evaporating in air. Some points deviate slightly from the theoretical law: these are the measurement points at the end of the evaporation. The droplet is then relatively small and approaches the size of the meshes of the calculation domain. Thus the measurement of the radius is less accurate since fewer meshes describe the droplet.
We now turn to the case of the sessile droplet. Before presenting the results of the simulations, some explanations are given on the numerical implementations made to simulate the evaporation of a sessile droplet.

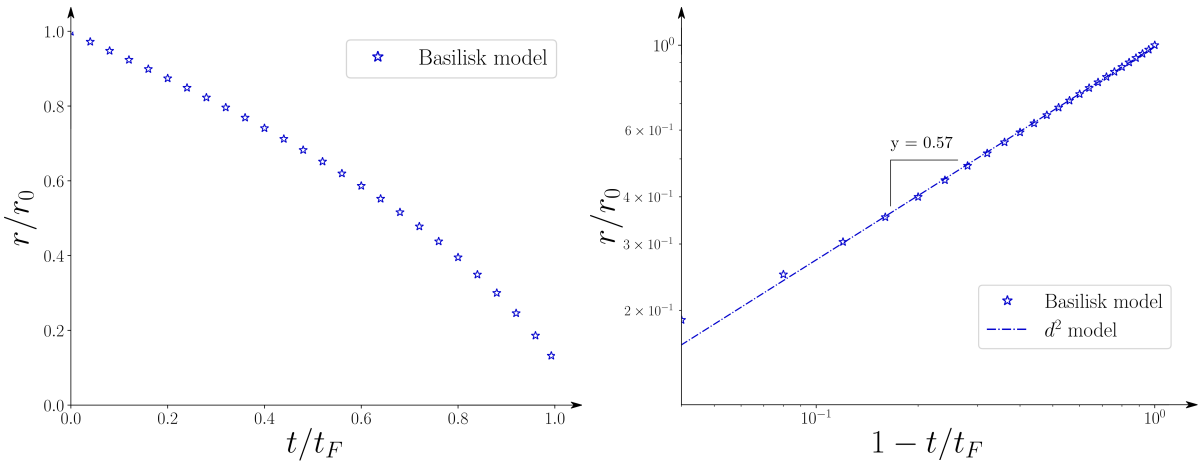

(a) (b)

Fig. 4.3 – (a) Evolution of the radius r scaled by the initial radius r_0 as function of the time t scaled by the final time of evaporation t_F. (b) Evolution of the radius r scaled by the initial radius r_0 as function of $1 - t/t_F$ in a logarithmic scale ($RH = 20\%$ and $V_0 = 10\,\mu$L).

2 Numerical implementations

We detail the new numerical methods developed to treat the case of sessile droplet evaporation. In a first step, the consideration of the phase change is described and is followed by the explanation of the implementation of the triple line pinning condition for the pinned evaporation mode is explained.

2.1 Phase change

The phase change corresponds to a **mass transfer**. This induces a velocity jump at the interface which results in a convective flow in the gas and an additional pressure in the liquid. This mass transfer was not taken into account until now in the Basilisk evaporation model. Many numerical methods have been developed previously for the study of phase change flows [91–97]. In the more specific context of VOF methods for DNS simulations of multiphase flows, the methods developed remain complex and sometimes unsatisfactory [98–100]. We propose here a **new method** based on the methods implemented in Basilisk and in particular on the volume fraction f.

First, the evaporation velocity $\mathbf{v}_e$ is calculated according to the following expression

$$\mathbf{v}_e \approx Pe_s D_v \overline{\nabla}(RH) \tag{4.8}$$

where Pe_s is the dimensionless Peclet number which compares the interface displacement and the vapor diffusion and RH is the relative humidity of the environment. This velocity is calculated at the beginning of the time step thanks to the vapor concentration gradient. The value of the Peclet number is fixed in the code, equal to 10^{-3}.

The second step is the advection of the interface. For phase-change problems, the VOF advection equation is

$$\frac{\partial f}{\partial t} + \overline{\nabla} \cdot (\mathbf{u} f) = -\frac{\dot{m}"}{\rho_l} \delta_I \tag{4.9}$$

where $\dot{m}"$ is the mass of liquid that evaporates across the surface of the droplet per unit time and δ_I indicates a dirac distribution at the interface.
The key point in this new method is to use the previously calculated velocity to advect the interface and to calculate the mass transfer term. The interface advection velocity is normally that of the fluid. However, by construction, in the cells that contain the interface, the mixed cells, the velocity is not exactly that of the fluid but a average value between the liquid and the gas. Malan [82] proposed a method to find the correct velocity of the liquid to detect the interface but this requires several additional complex calculation steps and to create a subdomain around the interface. We propose an alternative method which consists in calculating a phase change velocity and using this velocity in the advection equation. Thus the liquid velocity is not needed for advection and the phase change is well taken into account in VOF. To calculate the mass jump term, the advection equation is written as follows

$$\frac{f^* - f^n}{\Delta t} + \overline{\nabla} \cdot (\mathbf{v}_e^n f^n) = 0 \tag{4.10}$$

$$f^* = f^n - \Delta t \, \overline{\nabla} \cdot (\mathbf{v}_e^n f^n) \tag{4.11}$$

where f^* is the volume fraction at an intermediate time step and f^n is the volume fraction at the time step n. The term $\overline{\nabla} \cdot (\mathbf{v}_e^n f^n)$ corresponds to the mass transfer term $-(\dot{m}"/\rho_l)\delta_I$.

Physically, the loss of liquid mass due to evaporation is equivalent to the loss of volume fraction due to the advection of the interface advancing at the evaporation velocity. In this way we know the remaining volume fraction after evaporation and we can calculate the mass transfer term which corresponds to the difference in volume fraction between two time steps (Fig. 4.4). Geometrically we can write

$$m_{\text{geometric}} = \frac{f^* - f^n}{\Delta t} \tag{4.12}$$

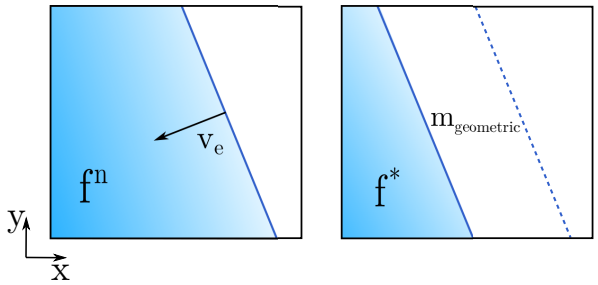

Fig. 4.4 – Reconstruction of the droplet interface in time with Basilisk. The phase change velocity $\mathbf{v}_e$ is used to advect the interface. The term of mass transfert $m_{\text{geometric}}$ is given by the volume fraction difference.

This geometric term must be multiplied to match the correct physical dimensions of a mass transfer term

$$\dot{m}" = m_{\text{geometric}} \cdot \rho_l \cdot \Delta = \frac{f^* - f^n}{\Delta t} \cdot \rho_l \cdot \Delta \tag{4.13}$$

where Δ is the size of the mesh. This shows the density jump at the interface between liquid and vapor. A condition is added to check that the volume fraction in the cell that previously contained the interface is empty after the interface has passed. The mass transfer term is added directly in the **Poisson solver**

$$\overline{\nabla} \cdot \left(\frac{1}{\rho^{n+1}} \overline{\nabla} p^{n+1} \right) = -\frac{1}{\Delta t} \dot{m}" \left(\frac{1}{\rho_l} - \frac{1}{\rho_g} \right) \delta_I \tag{4.14}$$

This allows the phase change to be taken into account while guaranteeing a velocity field $\mathbf{u}^{n+1}$ with zero divergence.

2.2 Pinned condition

When the droplet evaporates in a pinned mode, the radius remains fixed over time while the contact angle decreases. The triple line is therefore pinned throughout the evaporation. In the framework of the VOF reconstruction, this condition is non-trivial and requires special attention. A method has been implemented with the tools proposed by Basilisk.
This part repeats this method, previously presented in the following article "Lalanne, Cécile, et al. "Numerical model using a Volume-Of-Fluid method for the study of evaporating sessile droplets in both unpinned and pinned modes." European Journal of Mechanics-B/Fluids (2021)" [101].

For the sessile droplet configuration, the droplet is deposited on a substrate made of a non-corrosive material. We model the action of the substrate on the droplet by setting the value of the contact angle, θ, defined as the angle between the drop interface and the solid

surface. For the contact angle, we follow the method of Afkhami et al. [102] which uses the height functions in the VOF framework to impose a contact angle. In a 2D case, the cell containing the triple contact point is marked as a cell along the solid boundary with a volume fraction $f \neq 0$ and $f \neq 1$ and with a right cell with $f = 0$. This defines without ambiguity the cell. We compute the height functions for the two cells above the substrate (lines $h[1]$ and $h[2]$ in Fig. 4.5) in the horizontal direction from the y axis. We need some extra points to compute the curvature correctly at the triple point. We extend the work of [102] to a 5x5 stencil: consequently, the values of the ghost cells at each time step (two layers below the substrate, $h[-1]$ and $h[-2]$) are extrapolated linearly from the layers 1 and 2 above the substrate to impose a given contact angle

$$h[-1] = h[1] + \Delta / \tan\theta \tag{4.15}$$

where Δ denotes the cell size. $h[-2]$ is computed in the same way. We note that for $\theta < 45°$, we would compute the height function by the signed distance to the x axis. It is known that horizontal signed functions are more complicated to define accurately: anyway, the approach works fine enough with small angles.

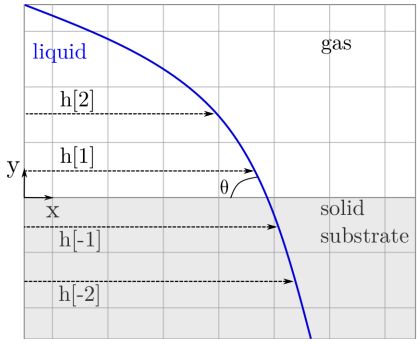

Fig. 4.5 – Use of horizontal height functions for the imposed contact angle θ. The height functions $h[1]$ and $h[2]$ allow to extrapolate the values of the ghost cells $h[-1]$ and $h[-2]$ which are then used to compute the curvature at the triple contact point and deduce the contact angle.

The classical VOF approach uses staggered grids for the velocity field then the normal and tangential components of the velocity at the substrate boundary ($y = 0$) are equal to zero by imposing the ghost cell values of the layers below the substrate. A consequence is that implementing an interface pinned configuration is quite complicated, the reason is that in the VOF approach the volume fraction f is transported with the staggered velocity field $\mathbf{u}$ resulting from the solution at time t of the Navier-Stokes equations using $\partial_t f + \nabla \cdot (f\mathbf{u}) = 0$. The staggered velocity field $\mathbf{u}$ over the 1st cell above the substrate has non-nul horizontal components u_x (for a cell of size Δ, the horizontal components are placed at $\Delta/2$) given a numerical slip when the volume fractions are transported, hence it is very difficult to ensure the stability of the pinned point of the interface at the boundary condition. Refining the numerical grid helps as the numerical slip scales with Δ.
Hooking a fixed point on a boundary condition needs precise handling: in the novel pinned implementation we have to modify the VOF reconstruction step to take into account specifically the conditions of constant radius and decreasing contact angle θ as a function of time.

Fig. 4.6 presents three schematics of a boundary cell containing the triple point (the bottom side represents the substrate): on the left, the classical VOF reconstruction for an unpinned evaporation mode and in the middle and on the right, the new pinned reconstruction. Fig. 4.6-a shows the slipping of the interface along the substrate with a contact angle θ which remains constant. For the novel pinned reconstruction approach, we proceed as following: once we compute the volume fraction at the next time step, $f(t_1)$ with $t_1 = t + dt$, we determine geometrically the new angle θ which keeps the mass in the local cell. This is done by defining the piecewise segment of the interface reconstruction passing through the pinned point x_p. In the following for sake of simplicity, we explain the algorithm in a local cartesian basis. The axisymmetrical equivalent is straightforward. The algorithm is composed of two different cases depending on the intersection point of the reconstructed piecewise segment with the cell boundaries. First, we normalize the distance with the cell size Δ, a dynamical variable depending on the time and space but fixed for a given time step. Secondly, we scale the value x_p using a local basis, in which the origin is placed at the left bottom corner of the cell, therefore we have all the lengths in the range $[0, 1]$ and Δ becomes equal to one. We have then:

1. the reconstructed segment passing through the pinned point x_p crossing the top of the cell at the point x_t (Fig. 4.6-b), then we have to compute the surface by a trapeze formule $f(t_1) = (x_p + x_t)/2$ to find x_t. We have finally: $\tan\theta_{i+1} = 1/(x_p - x_t)$.

2. if the reconstructed segment passing through the pinned point x_p crosses first the left side of the cell at the point y_t (Fig. 4.6c) we use a triangle formula $f(t_1) = y_t x_p/2$ for the surface and we have simply: $\tan\theta_{i+1} = 2\ f(t_1)/x_p^2$.

Once the angle θ_{i+1} of the pinned interface is computed we use the contact angle procedure to impose the boundary condition at the substrate, then θ_i is set to θ_{i+1} at each iteration.

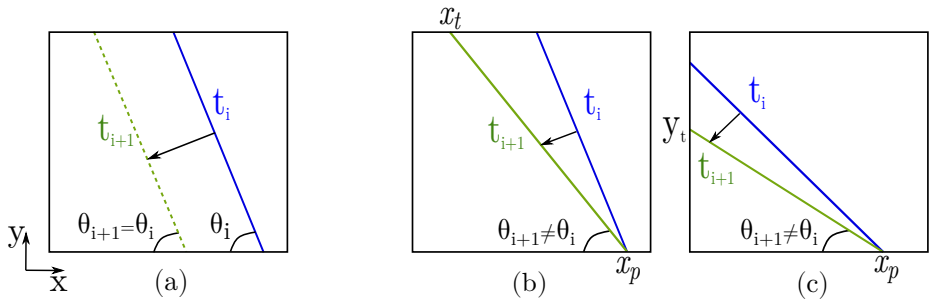

Fig. 4.6 – Schematics of the two steps VOF reconstruction on a boundary cell with a triple contact line: (a) is the classical reconstruction where the droplet radius decreases while evaporating always at constant contact angle θ, (b) and (c) are two cases of the new pinned mode depending of the line intersection, where the droplet radius is constant and the contact angle θ decreases as a function of time.

3 Unpinned mode of evaporation

When a sessile droplet is placed on a solid substrate, the presence of a substrate causes a perturbation in the evaporation dynamics compared to the case of the spherical droplet. When a surface is introduced, the droplet evaporates according to different evaporation modes. There are two main modes that are considered in this study as they represent the major part of the evaporation time. These modes are treated separately in this section. First, we consider the unpinned evaporation mode: in this case, the radius of the droplet decreases with time while the contact angle remains constant.

In the literature, several experimental studies with sessile drops of model liquids have shown that the d^2 law (Eq. 4.1), used to characterize the behavior of a spherical drop, remains valid to describe the **radius dynamics of a sessile drop** evaporating in air. It is for example the case when alkanes droplets evaporate in air as shown on Fig. 4.7a, where the exponent value is 0.48. The liquid considered in this section is pure water. It has been observed that the behavior of a pure water droplet evaporating in air deviates from the d^2 law. The power law introduced previously (Eq. 4.6) is however still valid but the exponent is different from 0.5 (Fig. 4.7b). For example, the data of Deegan [89], Poulard [103] and Shahidzadeh [104] converge to an exponent higher than 0.5, around 0.6.
In this part, we test the numerical model to see if we find the same dynamics and the same exponent for the power law. We compare the results with data from the literature. As a reminder, we did not perform experiments for the unpinned evaporation mode but only for the pinned mode.

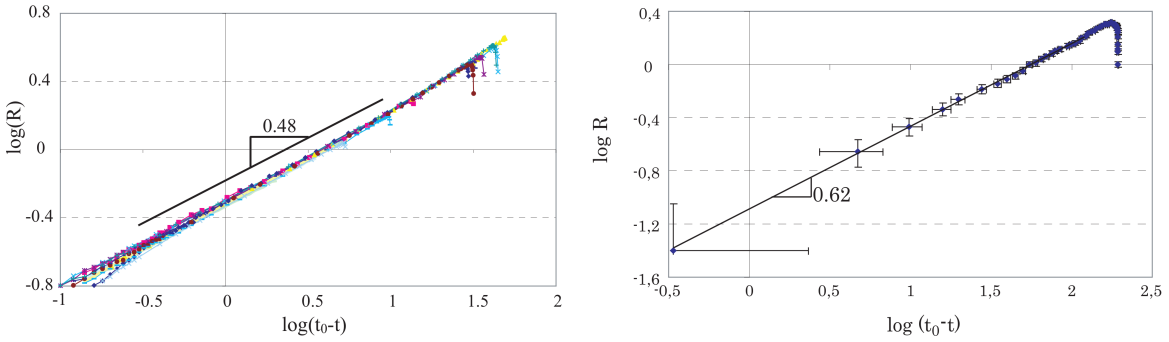

Fig. 4.7 – Analysis of the radius evolution R in time $t_0 - t$ (where t_0 here the final time of evaporation) for a sessile droplet. The logarithmic scale is used to highlight the power law behavior. (a) Data from Poulard for alkane on silicon wafer. (b) Data from Deegan for pure water on mica. (Graphs reproduced from [103])

Comparing to the case of the spherical droplet, the main difference is the **presence of the substrate** that must be modeled through boundary conditions as well as the contact angle that must vary throughout the simulations to represent different substrates. A contact angle is imposed with the already implemented macro "contact.h" available in Basilisk, which allows to set a contact angle on boundaries for interfaces described using a VOF tracer and height functions. Different contact angles are tested, between 45° and 90° to analyse the influence of the contact angle on the evaporation dynamics.
We perform 2D simulations, where the droplet is axisymmetric. Only half of the droplet is simulated to save time and the rest is reconstructed by symmetry. The Adaptative Mesh Refinement implemented in Basilisk is used to refine the mesh around the interface (Fig. 4.8a)

in order to obtain an accurate reconstruction in time of the moving droplet interface. The contact line moves along the substrate with a **slip condition**, which modelized a perfectly smooth substrate. The relative humidity will vary between the simulations to see its influence on the evaporation behavior.

3.1 Study of a sessile droplet with a contact angle of 90°

First, we propose to study a particular case in order to describe the evaporation dynamics before presenting the parametric studies where the relative humidity and the contact angle vary. The pure water droplet considered has a contact angle equal to 90° and the initial volume is set to 10 μL. The relative humidity of the environment is 0%. This corresponds to a special case since when a sessile droplet forms a contact angle of 90° with a surface, the evaporation flow is homogeneous along the interface, as in the case of a spherical drop evaporating in air.

The shape of the droplet over time is reconstructed (Fig. 4.8b). The droplet keeps a spherical cap shape all along the evaporation as the surface tension effects dominate the gravity effect. It is observed that the contact line slides along the substrate in accordance with the imposed boundary conditions. The contact angle remains constant during evaporation.

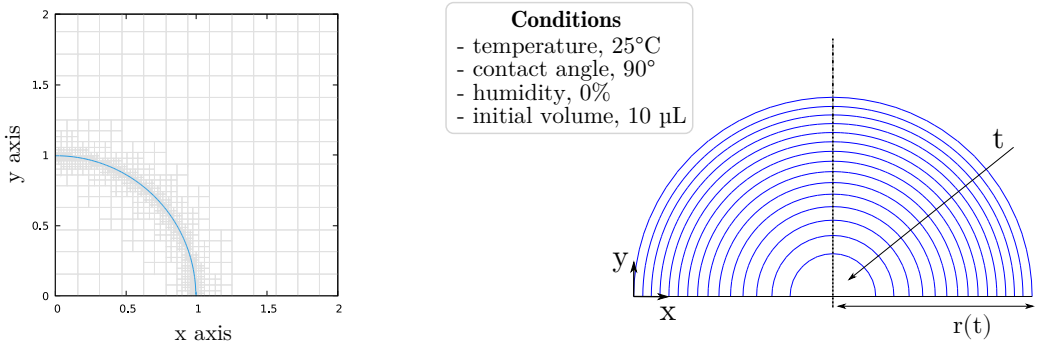

(a) (b)

Fig. 4.8 – (a) Reconstruction of the droplet interface with Basilisk and use of the Adaptation Mesh Refinement to follow the interface during the evaporation. (b) Interface evolution during evaporation for an unpinned sessile droplet with a contact angle of 90°.

The evolution of the contact radius of the droplet over time is presented at Fig. 4.9a. The radius decreases in time. To compare with the theoretical d^2 law, the squared radius is plotted as a function of time (Fig. 4.9b). The law is verified during most of the evaporation time, but at the end the Basilisk model moves away from this linear law. This apparent difference with the d^2 law needs more investigation. First, we checked that the numerical parameters of the model did not impact the results. A study on the mesh has been done and has shown that the chosen refinement levels allow to capture all the physics of the problem. An analysis on the size of the domain was done to verify that taking a domain ten times larger than the droplet was sufficient.

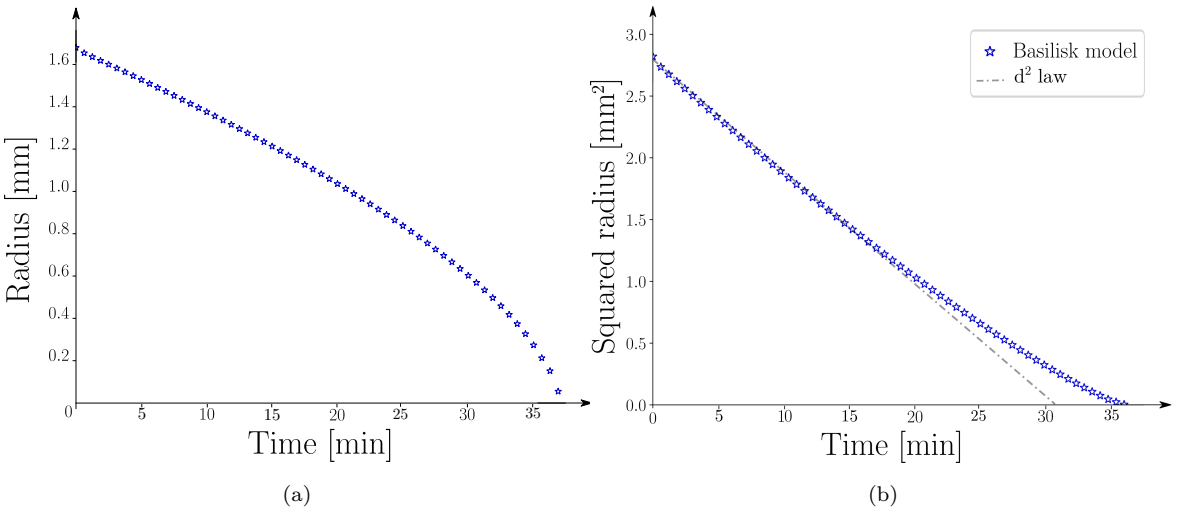

(a) (b)

Fig. 4.9 – Evolution of the droplet radius in time (a) and of the squared radius in time (b). The d^2 law is not verified for this example of sessile droplet: the numerical data (blue markers) move away from the theoretical law (dashed dotted line) at the end of evaporation.

As introduced before, this deviation from the d^2 law has already been observed in experimental studies [89,103,104]. We therefore tried to characterize the dynamics of the evolution of the radius in order to compare it with the results of the literature. We plot the radius as a function of $(t_F - t)$ (Fig. 4.10a) and switch to the log-log frame (Fig. 4.10b). A characteristic linear evolution is observed in the logarithmic scale which indicates that the radius of a sessile droplet follows a power law. The slope gives the exponent of the power law $y = 0.63$ (Eq. 4.6).

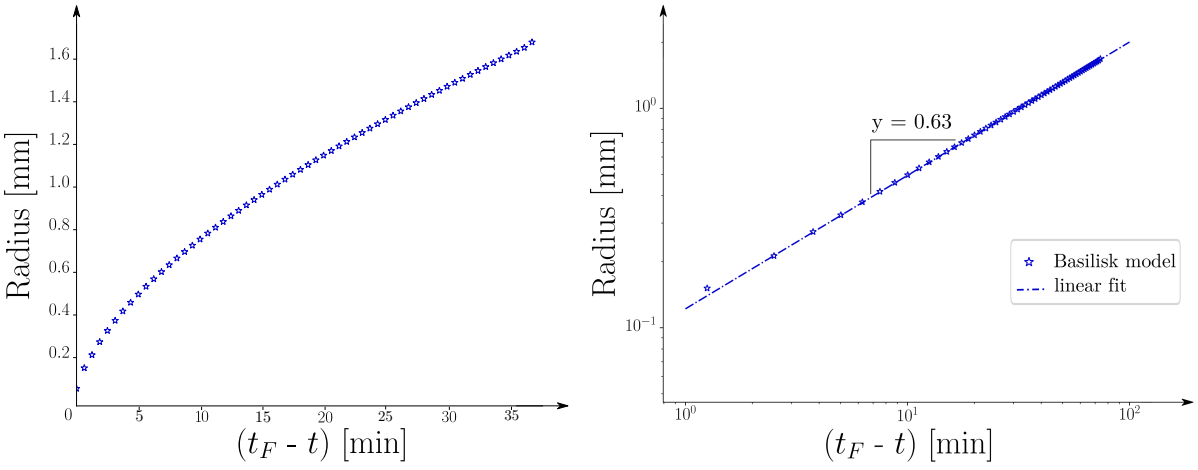

(a) (b)

Fig. 4.10 – Evolution of the droplet radius as function of (t_F - t) according to a linear scale (a) and then a logarithmic scale (b). A linear evolution is found in the logarithmic scale which means that the radius evolution follows a power law.

The evaporation dynamics of a droplet on a substrate follows a power law but **the exponent of this law is different** from the one obtained for a spherical drop in air as we obtain y = 0.63 and not y = 0.5. The theory is still applicable to the case where the sessile droplet is in contact with a solid substrate.

The evolution of the height and volume of the droplet over time can also be studied to characterize the evaporation dynamics. In this particular case where $\theta = 90°$, the height and the radius are identical and follow the same evolution. As we consider a droplet keeping the shape of a spherical cap, the volume is proportional to the cube of the radius

$$V(t) \propto r^3(t) \tag{4.16}$$
$$\propto (t_F - t)^{3y} \tag{4.17}$$
$$V^{2/3}(t) \propto (t_F - t)^{2y} \tag{4.18}$$

If y = 0.5 as in the case of a spherical droplet, then $V^{2/3}(t) \propto (t_F - t)$, that is a linear law. This has been observed experimentally by Erbil [105] and Soulié [37]. If we now consider the numerical result obtained for a sessile droplet of water, i.e. y = 0.63, then a linear law should be obtained for $V^{0.53}(t)$ and not $V^{2/3}(t)$. By scaling the volume by the initial droplet volume V_0, the following relation is deduced

$$\left(\frac{V}{V_0}\right)^{0.53} \propto 1 - \frac{t}{t_F} \tag{4.19}$$

To verify this, we plot successively $(V/V_0)^{2/3}$ and $(V/V_0)^{0.53}$ as a functions of time (Fig. 4.11). The numerical data do not follow a linear law for $(V/V_0)^{2/3}$. However $(V/V_0)^{0.53}$ as a function of time presents a linear decrease which validates the relation between volume and time in the case where the exponent y is different from the value predicted by the d^2 law.

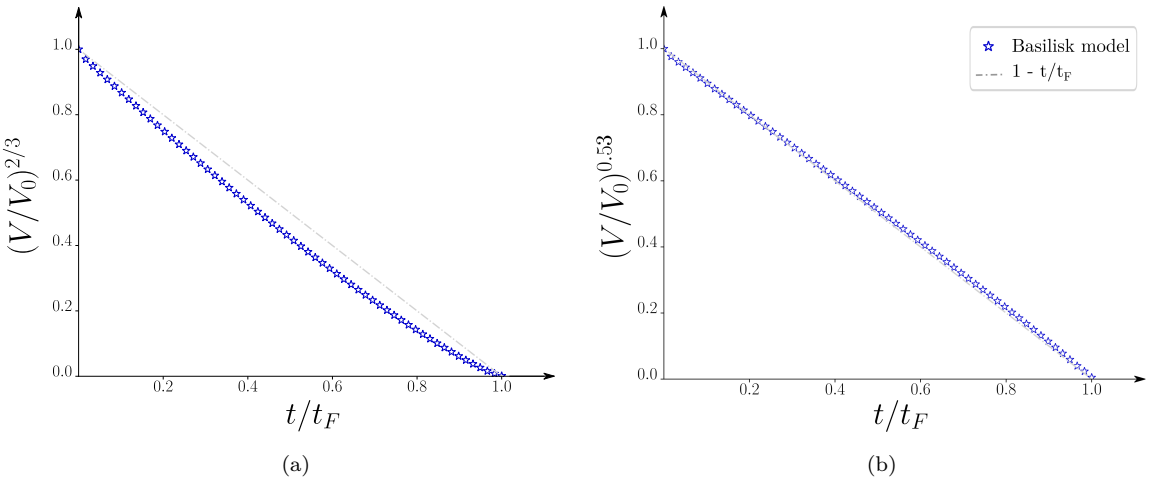

Fig. 4.11 – (a) Evolution of the scaled volume (V/V_0) at the power 2/3 as function of the scaled time (t/t_F). The theory predicts a linear decrease but we observe a difference. (b) Evolution of the scaled volume (V/V_0) at the power 0.53 as function of the scaled time (t/t_F).

The numerical results we have obtained must be compared with those of the literature and in particular with the experimental results. This allows to validate or not the model. As introduced at the beginning of this paragraph, the validity of the d^2 law for sessile droplets has already been discussed. The model puts forward a dynamics which follows the expected power law but the exponent is different from the one obtained in the theory for a spherical droplet (which was reproduced by the model however). Water appears to be a particular liquid since experiments with others liquids have shown that the law is well verified. In the

case of alkanes, Poulard and collaborators showed that the power law was respected and that the exponent was very close to the one predicted by the theory of spherical droplets as he found y = 0.48 [103]. In the case of water droplets, the experimental results showed that the evaporation dynamics follows the expected power law, i.e. $r(t) \propto (t_F - t)^y$. However, the exponent was quite different and higher than 0.5, as observed with the data collected by Deegan [89].
Different hypotheses to explain these differences have been proposed. Shahidzadeh explained the difference with the d^2 law by the presence of convection for the transport of the water vapor in air [104]. But in this numerical model, the vapor transport is purely diffusive which does not seem coherent with this explanation. Poulard and collaborators identified two regimes with different exponents for the evaporation of water. He proposed an explanation based on the particular properties of water. Indeed, in the experiments the contact angle formed by water on the substrate was larger than the one formed by alkanes. The d^2 theory remains relatively valid in the case of a sessile droplet, especially when the contact angle takes very small values or on the contrary when the contact angle is close to 180 °, i.e. when the surface and the droplet have only little interaction. The contact angles considered in this study are between 45° and 90°. This could be the reason why the law is different. Soulié also carried out an experimental work with pure water drops evaporating in a sliding mode, but in conditions where the contact angle remained very small, of the order of few degrees [37]. In these conditions, the d^2 law is verified which tends to confirm the influence of the contact angle.
We can conclude that the numerical model developed with Basilisk allows to simulate the evaporation dynamics as **the power law is verified**. The model reproduces the behavior observed experimentally for pure water sessile droplets. It would be interesting to perform simulations on other liquids than pure water, such as alkanes for example, to see if the behavior observed in the experiments is found numerically. In the following, the contact angle and the relative humidity will be varied in order to observe the influence of these two parameters on the evaporation dynamics.

3.2 Parametric studies

Variation of the contact angle

We vary the value of the initial contact angle of the drop. As the droplets evaporates according to the unpinned mode, the contact angle then remains constant for the whole evaporation process.
A change of initial contact angle models a different surface condition of the substrate (the liquid parameters remain unchanged). This can, for example, represent a change in the material of the substrate. Indeed, the same droplet deposited on two different materials forms different contact angles: for water on teflon Nguyen observed $\theta_0 = 108°$ [106], for water on pyrex glass Lim ended up with $\theta_0 = 65°$ [107] while for water on polished epoxy resin, Bourgès-Monnier and Shanahan obtained $\theta_0 = 55°$ [108]. We therefore vary the contact angle in this study to represent different pure water/material couples. The other parameters remain unchanged. We always consider a drop of 10 μL, evaporating in an environment with 0 % of relative humidity. The contact angle θ takes the following values: 90, 75, 60 and 45 °.

First, the shapes of each case are reconstructed (Fig. 4.12). Whatever the value of the contact angle, the spherical cap condition is well respected. The radius varies from one case to another and increases when the contact angle decreases as the initial volume is identical through the different cases tested.

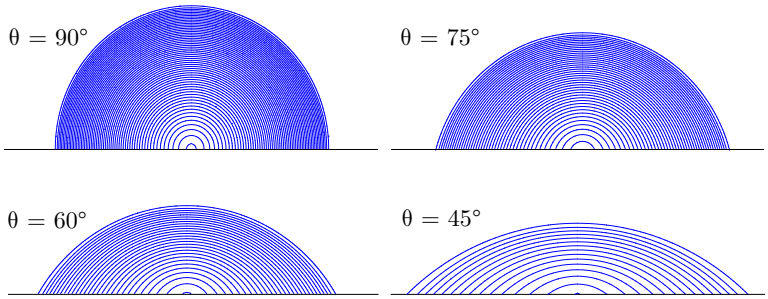

Fig. 4.12 – Reconstruction of the droplet interface in time with Basilisk for four different droplets. Each case starts with a different initial contact angle θ. ($V_0 = 10\,\mu$L and $RH = 0\%$)

For the cases where the contact angle is different from 90°, the radius and height are different for the same drop. We represent at Fig. 4.13 the variation of the radius as well as the variation of the height as a function of time for each tested case. The smaller the initial contact angle, the larger the initial radius, in order to keep the initial volume constant. The radius r is scaled by the initial radius r_0 to better compare each case (Fig. 4.13a). In the inset, for each case the radius decreases in time, according to the same behavior. The decay slope, or in a way the evaporation rate, becomes larger as the initial contact angle decreases. This is consistent since evaporation is proportional to the droplet radius and the radius is larger as the contact angle decreases. Droplets with a small contact angle evaporate faster. Concerning the height of the drops over time, the behavior is quite similar to that of the radius (Fig. 4.13b). When the initial contact angle decreases, then the initial height, which corresponds in fact to the maximum height of the drop, decreases.

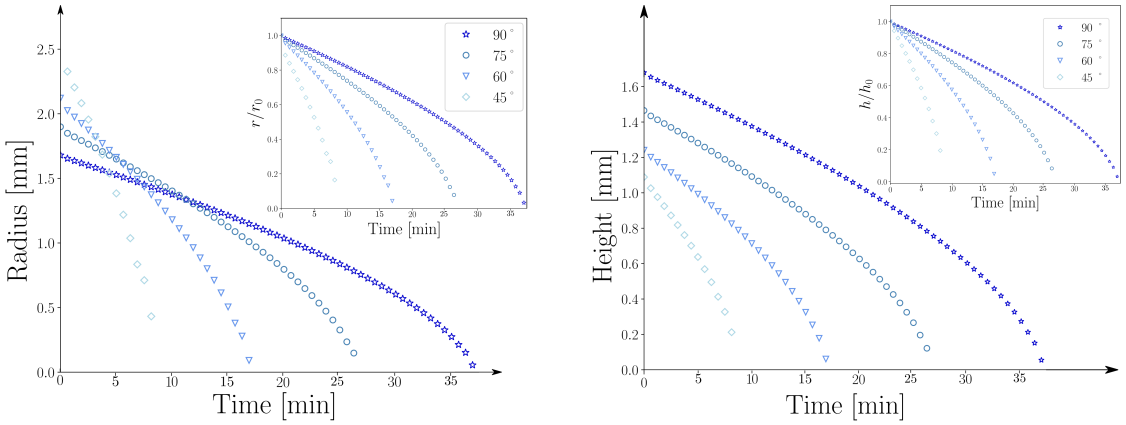

(a) (b)

Fig. 4.13 – Evolution of the droplets for different contact angles. (a) Radius r as a function in time and in the inset, the radius is scaled by the initial radius r_0. (b) Height h as a function of time and in the inset, the height is scaled by the initial height h_0. ($V_0 = 10\,\mu$L and $RH = 0\%$)

The change of contact angle seems to only affect the rate of evaporation and so the total time of evaporation. In order to confirm this observation, the evaporation rate dV/dt related to each case is calculated. The evaporation rate is not constant through the entire evolution process: it varies as the evaporation dynamics does not follow a linear behavior during the whole evaporation. The evaporation rate is however constant during the first two thirds of the evaporation since in this phase the dynamics follows a linear trend. The rate is thus calculated at the beginning of the evaporation between $t = 0$ min and $t = 5$ min, as an approximation

of the global evaporation rate. dV/dt decreases according a linear law when the contact angle increases (Fig. 4.14). This confirms that **the evaporation is faster for droplets with small contact angles**. The presence of the substrate disturbs the evaporative flow along the droplet interface. When the contact angle is smaller than 90°, the flow is non-uniform and diverges at the contact line. The singularity of the flow at the triple line is accentuated as the contact angle decreases which leads to a higher evaporation rate for small contact angles.

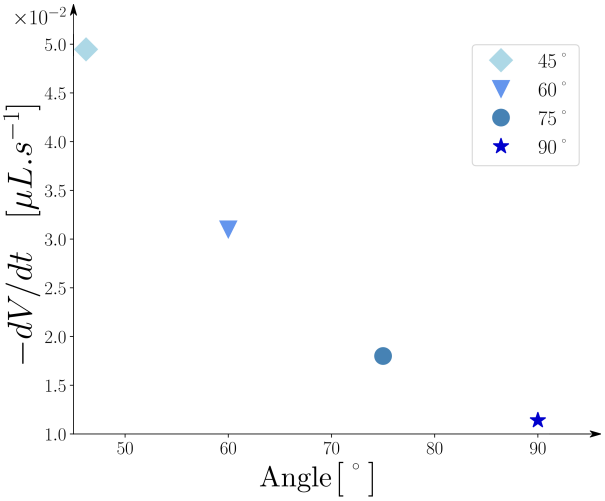

Fig. 4.14 – Evolution of the evaporation rate dV/dt as function of the value of the contact angle θ. The rate is calculated at the beginning of the evaporation, between $t = 0$ and $t = 5$ min. ($V_0 = 10\,\mu$L and $RH = 0\%$)

If the evaporation rate is linear with the contact angle then the final time could also be expected to vary linearly with this parameter. We will see that this is not the case because the evaporation rates were calculated and compared only over a restricted interval at the beginning of evaporation, where the evaporation dynamics were linear. The total time of evaporation t_F is presented as a function of the contact angle (Fig. 4.15). As already observed, the final time increases when the contact angle increases. The evolution seems to follow a power law $t_F \propto \theta^2$.

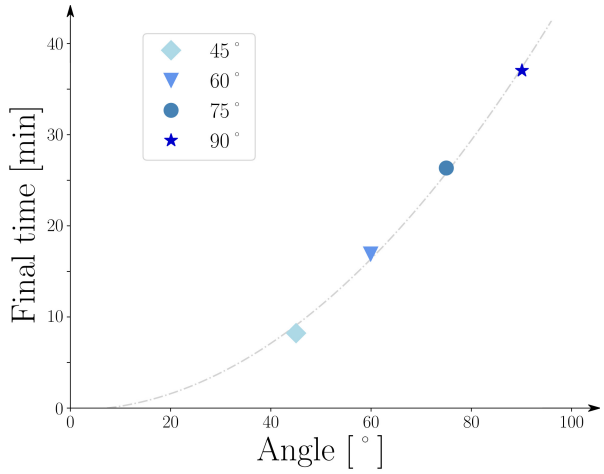

Fig. 4.15 – Relation between the final time of evaporation t_F and the contact angle θ. The evolution seems to follow a power law (dashed dotted line). ($V_0 = 10\,\mu$L and $RH = 0\%$)

In the context of corrosion, the final time of evaporation is an important information as it determines the contact time between the droplet and the solid substrate. The sessile droplet acts like an electrolyte solution. In the case where there is an electrochemical interaction between the substrate and the liquid (if the droplet contains chemical species that can react with the material constituting the solid), the evaporation time also determines the length of time in which these reactions can take place. For example, if we consider a liquid-solid couple that can lead to atmospheric corrosion, the evaporation time can determine in a first approximation the time when the corrosion can occur. Thus, the longer it takes for the droplet to evaporate, the longer the corrosion processes take place and therefore the more damage occurs.

The variation of angle allows to observe the influence of the contact angle on the evaporation dynamics. We want to know if the power law described at the beginning of this chapter describes the behavior of the droplet radius over time for the different contact angles tested and if the exponent y highlighted previously remains unchanged. We plot the radius as a function of (t_F - t) (Fig. 4.16a) and then switch to a logarithmic scale (Fig. 4.16b). For the four cases tested, the dynamics of the radius always follows a power law, as suggested by the linear behavior found in the logarithmic scale. For each case, the exponent y obtained is: 0.63 for $\theta = 90°$, 0.59 for $\theta = 75°$, 0.64 for $\theta = 60°$ and 0.58 for $\theta = 45°$, that is an average of 0.61. There is **no specific evolution of the exponent** with the contact angle. Regardless of the contact angle, a sessile droplet evaporating according to the unpinned mode follows a power law with $y = 0.61 \pm 0.03$.

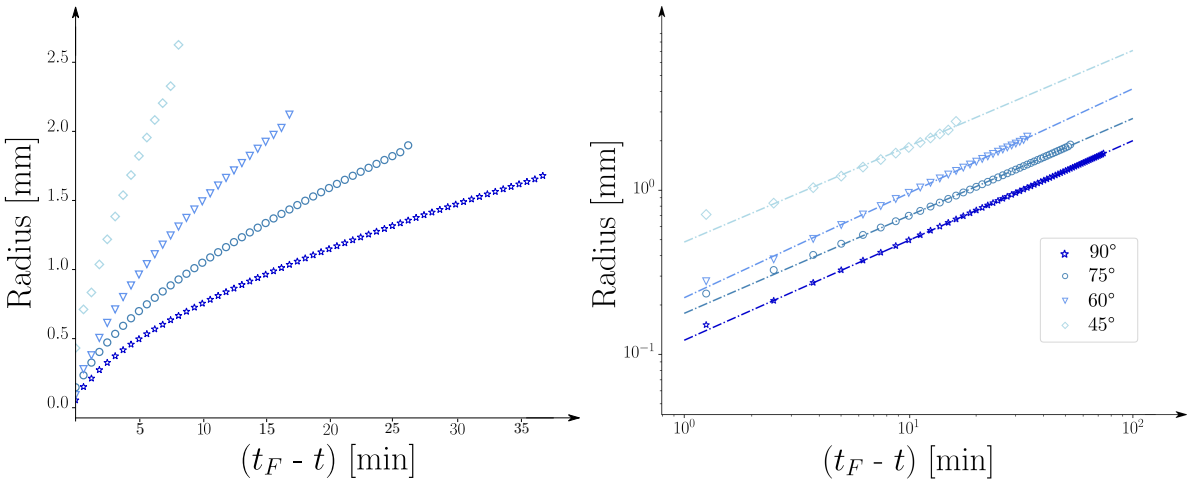

Fig. 4.16 – Evolution of the droplets radius as function of $(t_F - t)$ for different contact angles. The analysis is done in a linear scale (a) and in a logarithmic scale (b). ($V_0 = 10\,\mu$L and $RH = 0\%$)

In a second time, we study the evolution of the volume in time (Fig. 4.17). We consider droplets having the same initial volume, $V_0 = 10\mu$L, despite a different contact angle. The evolution of the volume as a function of time is decreasing and seems to follow two phases: a first linear phase and a second non-linear phase where the evaporation slows down (Fig. 4.17a). This behavior is the **typical behavior** expected in the case of a sessile drop evaporating according to the unpinned mode. This allows to **validate the numerical model**, it represents well the dynamics of evaporation for this mode of evaporation.
In the inset of Fig. 4.17a, the volume V is scaled by the initial volume V_0 and the time t is scaled by the final time of evaporation t_F. The data gather and overlap along the same curve

which shows that the change of contact angle does not influence the evaporation behavior of the sessile drop, it simply modifies the evaporation rate. By scaling, the parameters of each test case are no longer influencing the behavior and an universal evaporation behavior for the sessile drops in the unpinned mode is highlighted, independent of the initial contact angle. Finally we plot the scaled volume V/V_0 to the power 0.53 as a function of the scaled time (Fig. 4.17b). A linear decrease is observed, which is in accordance with the analysis made previously for the case where $\theta = 90°$. We can conclude that the power law presented at the beginning of this chapter is still verified and that the exponent y highlighted previously remains unchanged as the contact angle varies. Decreasing the contact angle does not change the power law behavior of evaporation, however the evaporation rate increases as the angle becomes smaller and smaller. The contact angle effect on the evaporation rate can be explained by the singularity of the vapor flux diffusing from the free surface of the droplet into the surrounding air at the droplet edge.

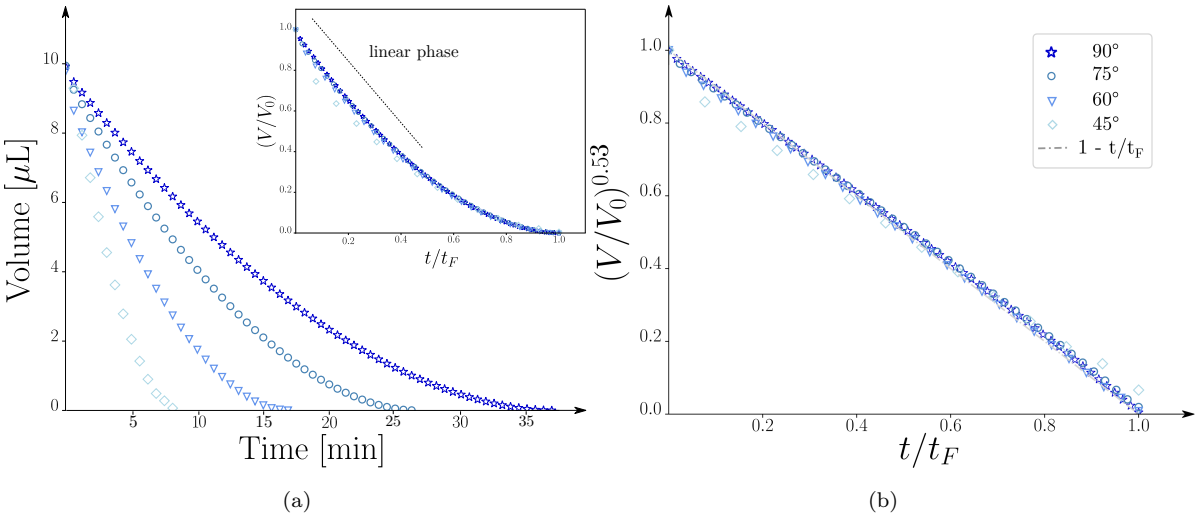

Fig. 4.17 – Droplet volume as function of time for different contact angles. (a) Evolution of the volume in time. In the inset, the volume is scaled by the initial volume and the time is scaled by the final time. (b) Evolution of the scaled volume to the power 0.53 as function of the scaled time. ($V_0 = 10\,\mu$L and $RH = 0\%$)

Variation of the relative humidity

In this second parametric study, the relative humidity of the environment is modified for each simulation. Four different humidities are tested: 0%, 20%, 40 % and 60 %. The more the humidity increases, the more the vapor gradient between the droplet and the distant environment decreases, which has for consequence to slow down the evaporation phenomenon. In this section, we compare the evaporation dynamics and the evaporation rate to check the influence of the relative humidity on the evaporation dynamics. We consider cases where the contact angle is equal to 90° so the height is identical to the radius: therefore, it is not necessary to follow in addition the evolution of the height. For each humidity, the droplet has the same initial volume $V_0 = 10\,\mu$L and the same initial radius $r_0 = 1.65$ mm. The humidity is thus the only parameter which influences the evaporation.

To study the dynamics of evaporation, the time evolution of the radius is analyzed (Fig. 4.18). All the curves follow the same decreasing behavior, but as the relative humidity in-

creases, the slope decreases and therefore the total evaporation time is longer. The droplet considered takes around 47 min to evaporates if the relative humidity is equal to 20% and around 62 min if the relative humidity is equal to 40%.

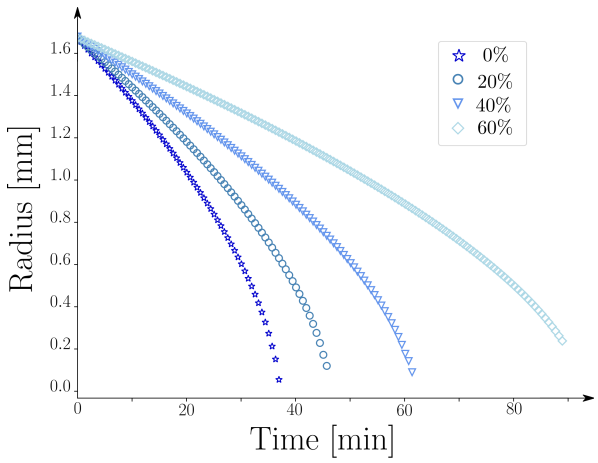

Fig. 4.18 – Evolution of the radius in time for different relative humidities. The initial radius and the initial volume is identical for each case which allows to compare the evaporation dynamics. ($V_0 = 10\,\mu$L and $\theta = 90°$)

The evaporation rate can be calculated for each relative humidity tested. As it varies along the evaporation process, it is calculated at the beginning of the evaporation, between $t = 0$ and $t = 5$ min. The evaporation rate is inversely proportional to the relative humidity (Fig. 4.19) which is coherent as a droplet evaporates slower in an environment with a high humidity percentage.

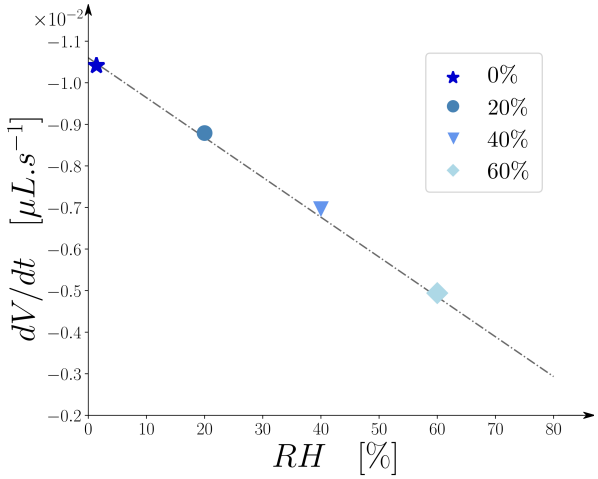

Fig. 4.19 – Evolution of the evaporation rate dV/dt as function of the relative humidity (RH) of the environment around the droplet. The rate is calculated at the beginning of the evaporation, between $t = 0$ and $t = 5$ min. ($V_0 = 10\,\mu$L and $\theta = 90°$)

As explained before, the final time of evaporation is an important variable to measure. We plot the final time of evaporation as function of the relative humidity (Fig. 4.20). The evolution seems to follow a power law $t_F \propto RH^{1.96}$ where the exponent is identical to the one of the power law found for the parametric study of the contact angle. This can be usefull to predict the total time of evaporation depending on the conditions of evaporation.

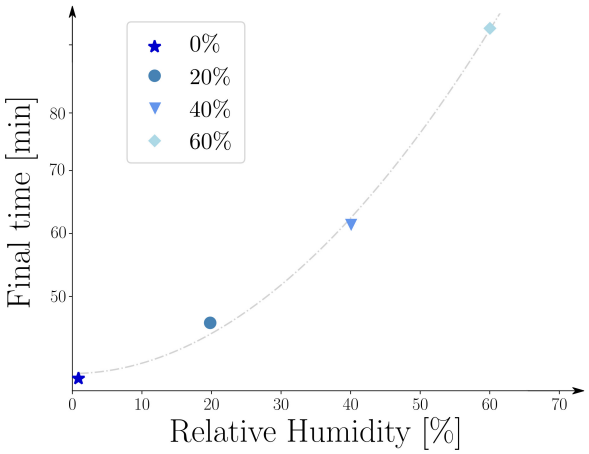

Fig. 4.20 – Relation between the final time of evaporation t_F and the relative humidity RH. The evolution seems to follow a power law (dashed dotted line).($V_0 = 10\,\mu$L and $\theta = 90°$)

As in the parametric study on the contact angle, one can ask whether the evaporation dynamics is still described by the power law previously explained despite a change in relative humidity and if the exponent of this power law will be modified by a change of humidity. We plot the evolution of the radius for the different cases as a function of $(t_F - t)$ according to a linear scale (Fig. 4.21a) then according to a logarithmic scale (Fig. 4.21b). For each percentage of humidity tested, the power law is respected since a linear law is found in the logarithmic scale. The slopes, which correspond to the exponents of the law are: y = 0.63 for 0% HR, y = 0.59 for 20% HR, y = 0.60 for 40% HR and y = 0.61 for 60% HR, that is an average of 0.61 as previously. To conclude, the relative humidity does not impact the evaporation dynamics and always follows a power law close to that of d^2 whatever the relative humidity. Physically, it means that the driving phenomenon of evaporation remains the same, the diffusion, even if the relative humidity is changed and if the evaporation time is more important.

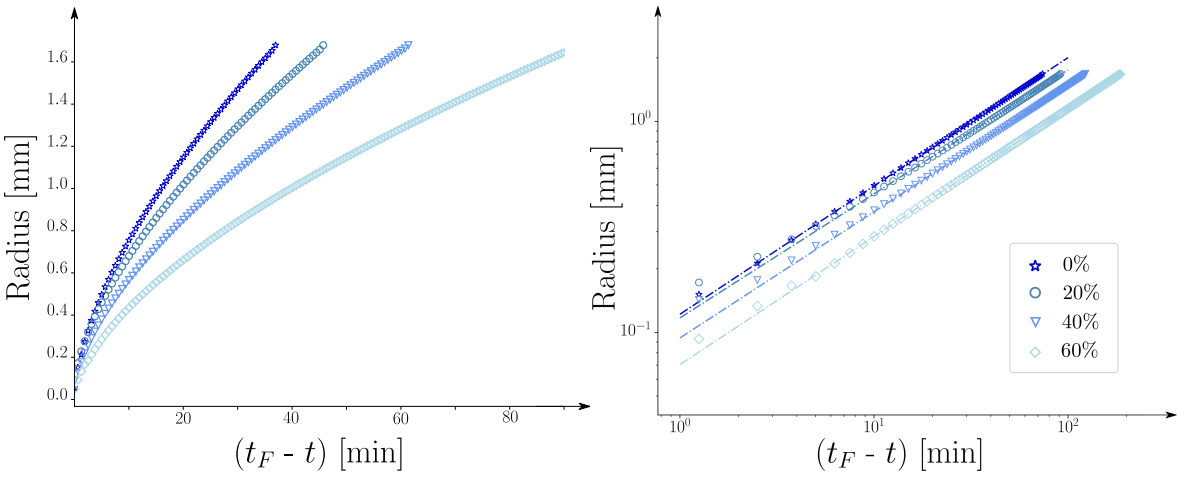

Fig. 4.21 – Evolution of the radius as function of $(t_F - t)$ for different relative humidities. The analysis is done in a linear scale (a) and in a logarithmic scale (b). In the loglog scale, the radius follows a linear law which is characteristic of a power law behavior in the linear scale. The slope of the linear scale does not vary much with the relative humidity which means that the exponent of the power law remains identical. ($V_0 = 10\,\mu$L and $\theta = 90°$)

Finally, the volume versus time is plotted for the four cases on Fig. 4.22. The **evaporation behavior is similar** for the different relative humidities tested (Fig. 4.22a). The change of relative humidity only affects the final time of evaporation as the evaporation rate decreases when the relative humidity increases. The scaling of the time by the final time t_F in the inset confirms this analysis since all the curves overlap. The volume V is scaled by the initial volume V_0 and plotted to the power 0.53 as function of the scaled time (Fig. 4.22b). The decrease is linear and thus respect the power law (Eq. 4.19) regardless of the value of the relative humidity of the environment. This concludes the parametric study about the relative humidity: the behavior of an evaporating sessile droplet remains unchanged if the relative humidity varies. The dynamics is always described by a **power law with the same exponent**.

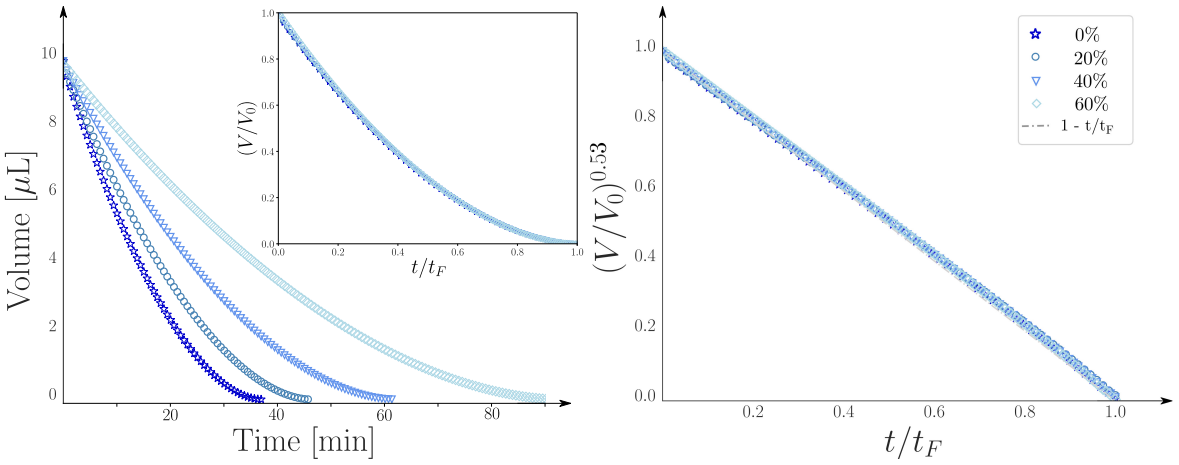

(a) (b)

Fig. 4.22 – Volume as function of time for different relative humidities. (a) Evolution of the volume in time. In the inset, the volume is scaled by the initial volume and the time is scaled by the final time. (b) Evolution of the scaled volume to the power 0.53 as function of the scaled time. ($V_0 = 10\,\mu$L and $\theta = 90°$)

4 Pinned mode of evaporation

In this last section, we consider sessile droplets evaporating according to the pinned mode. To perform the numerical simulations, we use the pinning implementation detailled in Section 2. During the evaporation process, the contact radius is fixed while the contact angle varies. First, the numerical model is validated with the experimental data presented in Chapter 3. Then, two parametric studies are presented to observe the influence of the initial contact angle and the relative humidity on the evaporation dynamics.

4.1 Analysis of a particular case

To test the numerical implementation of the **contact line pinning condition**, we simulate the evaporation of a sessile droplet with an initial contact angle $\theta_0 = 80°$ and an initial volume $V_0 = 42\,\mu$L. The relative humidity chosen for this case is 10%. The numerical results are compared with the results of the previously introduced experimental study.

The interface is reconstructed and recorded during the evaporation (Fig. 4.23). It is thus verified that the droplet evaporates according to a pinned mode: the radius remains constant while the contact angle decreases with time. This reconstruction of the interface over time seems to show a constant dynamics since the distance between the positions of the interface remains globally constant. We will continue this analysis in more detail by studying one by one the variables that describe the evolution of the droplet over time, namely the height h, the contact angle θ and finally the volume V.

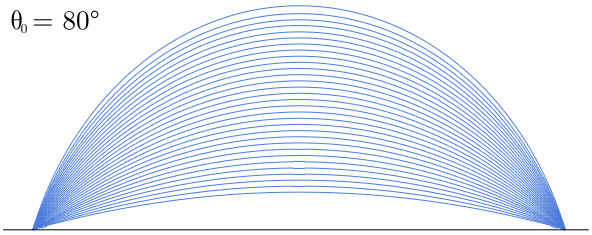

Fig. 4.23 – Interface reconstruction with the VOF method of Basilisk. Sessile droplet evaporating in the pinned mode where the radius is fixed. ($V_0 = 42\,\mu$L and $RH = 10\%$)

The evolution of the contact angle θ is plotted against time (Fig. 4.24). The numerical and experimental results are compared. The trend is similar and the results obtained with the model are very close to the experimental observations, which allows to **validate the model** and in particular the anchoring condition of the triple line. However, some differences are to be noted concerning the conditions specific to each case (Fig. 4.24a). The initial contact angles are slightly different ($\pm 5°$). Indeed, the contact angle is difficult to control experimentally and also difficult to measure so we did not succeed in obtaining an initial angle of exactly 80°. Moreover, the experimentally measured contact angle shows a constant phase for about 5 minutes. This corresponds to the equilibrium time of the droplet [38], which is neglected in the simulations. These two differences justify the discrepancies between the numerical and experimental points. To abstract from these two differences, the contact angles are scaled respectively by the initial contact angle θ_0 are compared (Fig. 4.24b). In the inset of this figure, the equilibrium phase is removed from the experimental data and the data are then shifted to the left to compare only the evaporation phase. This way, the coherence between the numerical model and the experimental results appears clearly. The contact angle varies linearly in time when the droplet evaporates in the pinned mode. This is the expected behavior described by theoretical laws [40].

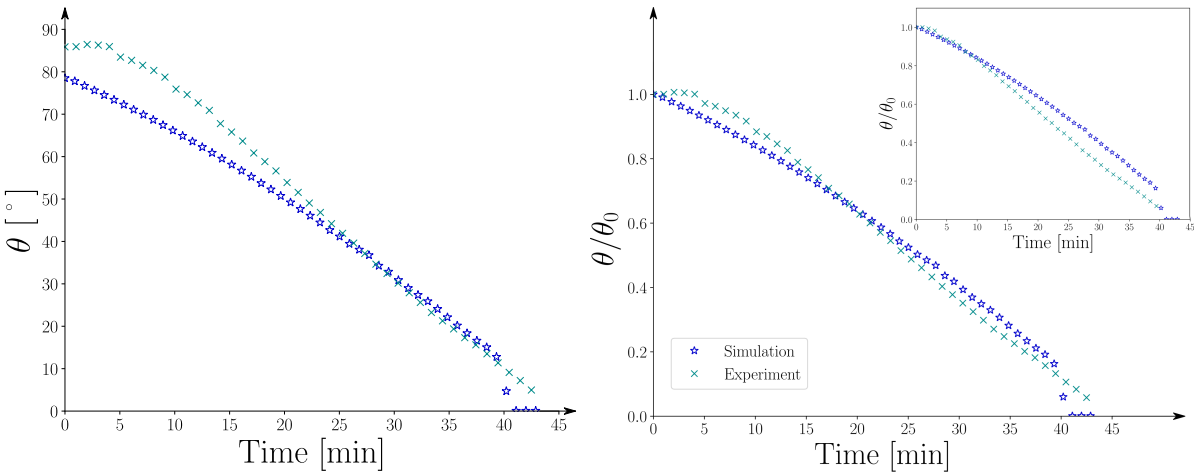

(a) (b)

Fig. 4.24 – Evolution of the contact angle as function of time. (a) Comparison between numerical results and experimental data. (b) The contact angles are scaled respectively by the initial contact angle to better compare the results. The inset presents the same data but the equilibrium phase observed for the experiment at the beginning of the evaporation is removed. ($V_0 = 42\,\mu$L, $RH = 10\%$ and $\theta = 80°$)

When the droplet becomes very small and very flat, i.e. for contact angles lower than 15°, the reconstruction limit of the method is reached. Indeed, only the horizontal height functions are used for the reconstruction of the interface. When the contact angle decreases, the shape of the droplet becomes flatter and flatter even if it still verifies the spherical heading hypothesis. In this geometric configuration, horizontal height functions are no longer able to accurately reconstruct the interface. Vertical height functions would be much more suitable. This is a possible improvement of the numerical method: we can consider a condition on the contact angle that would allow to switch from the use of horizontal height functions to the use of vertical ones. This justifies that the last numerical data points at the end of evaporation are out of the trend.

The height h and volume V as functions of time are then studied (Fig. 4.25). These quantities decrease linearly, which confirms the observation made by analyzing the evolution of the interface. Physically, this means that the evaporation rate, i.e. the global evaporation rate, remains constant during the whole evaporation. The droplet does not evaporate faster at the beginning or at the end of the evaporation. This is coherent with the theoretical formulation of the evaporation rate for the pinned mode proposed by Picknett and Bexon [50]. Many authors then proposed approximate expressions to describe the evaporation flux [53,105,108–110]. Hu and Larson [88] have developed an approximate expression by combining experimental, numerical and theoretical work. This expression is in good agreement with the theory of Picknett and Bexon for contact angles between 0 and 90°. As this is the range of angles we are studying here, the following expression of Hu and Larson for the evaporation rate will be used to compare the numerical results obtained

$$\frac{dm}{dt} = -\pi r_0 D_v (1 - RH) c_s (0.27\theta^2 + 1.30) \tag{4.20}$$

According to this relationship, the evaporation rate is proportional to the radius, the vapor concentration gradient, and the diffusion coefficient of the vapor in the air. The evaporation

rate depends weakly on the contact angle and when the contact angle becomes smaller than 40°, the evaporation rate becomes constant. This is even more true if the initial contact angle is small [50]. A sessile droplet evaporating in a pinned mode shows a **linear behavior** as a function of time, contrary to what has been observed for the unpinned mode. The numerical model reproduces the correct dynamics which validates the numerical tool.

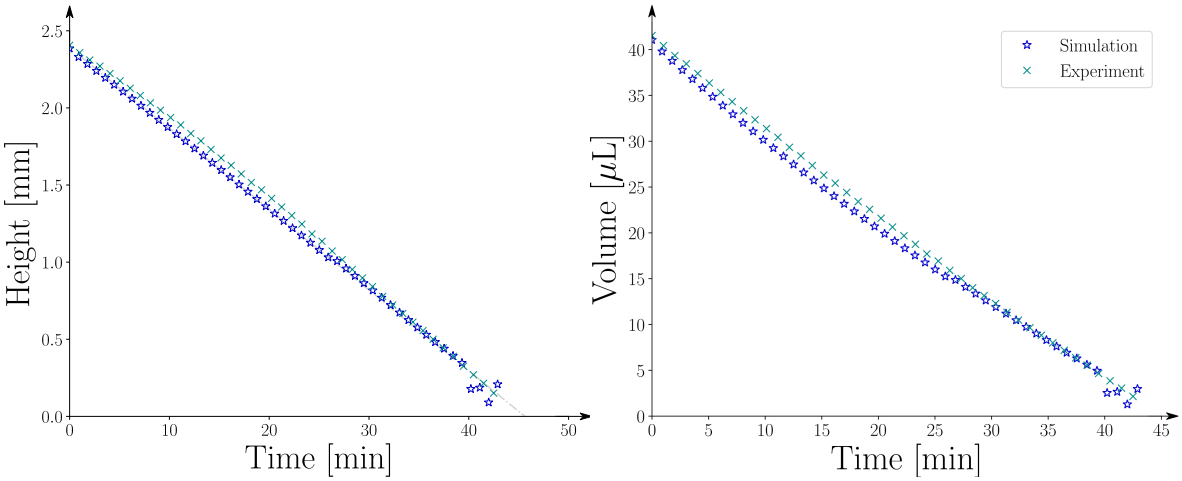

(a) (b)

Fig. 4.25 – Comparison between numerical and experimental data. (a) Evolution of the droplet height in time. (b) Evolution of the volume in time. ($V_0 = 42\,\mu$L, $RH = 10\%$ and $\theta = 80°$)

Analysis of the velocity field

To complete this analysis, the velocity field inside and outside the droplet is also studied. Unlike the unpinned mode, the pinned evaporation mode with the triple line anchor condition results in a particular hydrodynamics inside the droplet that is interesting to reproduce since it affects the transport of species possibly present in the droplet [68]. The code is able to reproduce a velocity field consistent and in agreement with other results in the literature [64, 65, 111–113].
Because of the pinning condition, a **capillary flow** appears, going from the center to the droplet edge (Fig. 4.26a). This supports the dynamics of evaporation flow compensation to maintain a spherical cap shape for the droplet. The two components of the velocity are also plotted along a vertical axis (Fig. 4.26b). The maximum velocities are localized at the interface and especially at the triple point, where the evaporative flow is the most important (Fig. 4.27a). Outside the droplet, the increased evaporation flow at the triple line and the phase change result in a **recirculation zone** in the air around the droplet (Fig. 4.27b). This recirculation can impact the saturation conditions at the interface of the droplet, towards its top. In the conditions we considered case, the intensity of this recirculation zone is extremely low (the maximum velocity is about 10^{-8} m.s^{-1}) so it does not impact the evaporation dynamics of the droplet.

Access to the velocity field inside and outside the droplet is an advantage of numerical simulations over experiments. It is possible to use tracers inside the droplet to track the flows inside the droplet but it is more complicated to have access to the flows outside.

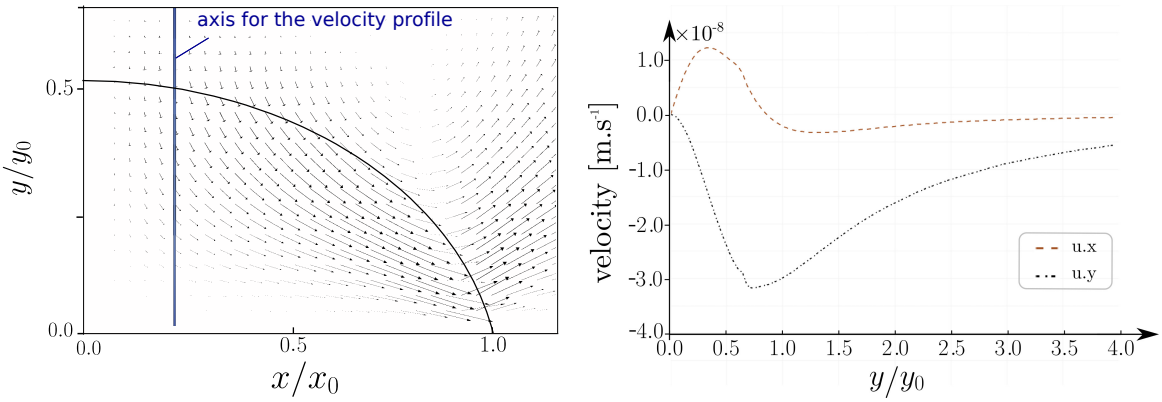

(a) (b)

Fig. 4.26 – (a) Vectors representing the velocity field inside the droplet. The vectors size scale for the velocity norm. (b) Velocities $u.x$ and $u.y$ along a vertical axis (represented in blue on graph (a)). ($V_0 = 42\,\mu$L, $RH = 10\%$ and $\theta = 80°$)

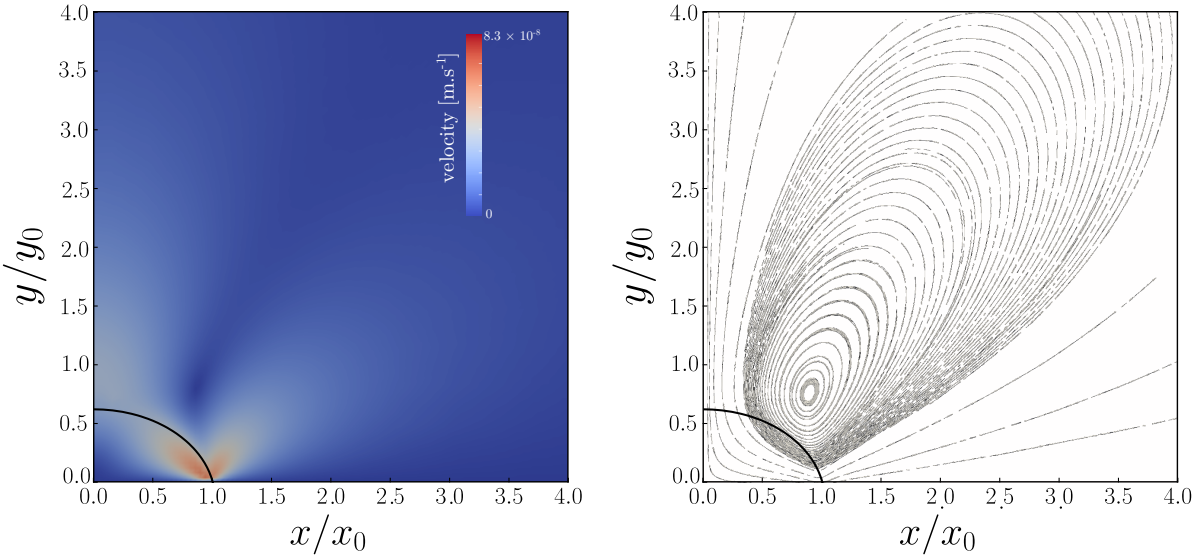

(a) (b)

Fig. 4.27 – Velocity field inside and outside the droplet. (a) Field representing the norm of the velocity. (b) Velocity streamlines highlighting a recirculation area in the gas phase. ($V_0 = 42\,\mu$L, $RH = 10\%$ and $\theta = 80°$)

4.2 Parametric studies

Variation of the initial contact angle

The initial contact angle θ_0 is modified for each simulation to observe the influence of this parameter on the evaporation dynamics. Four different values are tested: 80, 70, 60 and 50°. The other parameters remain unchanged from one case to another, namely: an initial volume of 10 μL, a relative humidity RH of 0% and an ambient temperature of 25°C. The evolution of the angle, the height h and the volume V of the droplet are plotted against time.

For each angle tested, the height decreases linearly with time (Fig. 4.28a). The initial height is different for each case since the initial contact angle varies while the initial volume remains constant. The study of the evolution of the contact angle as a function of time shows the same dynamics (Fig. 4.28b).

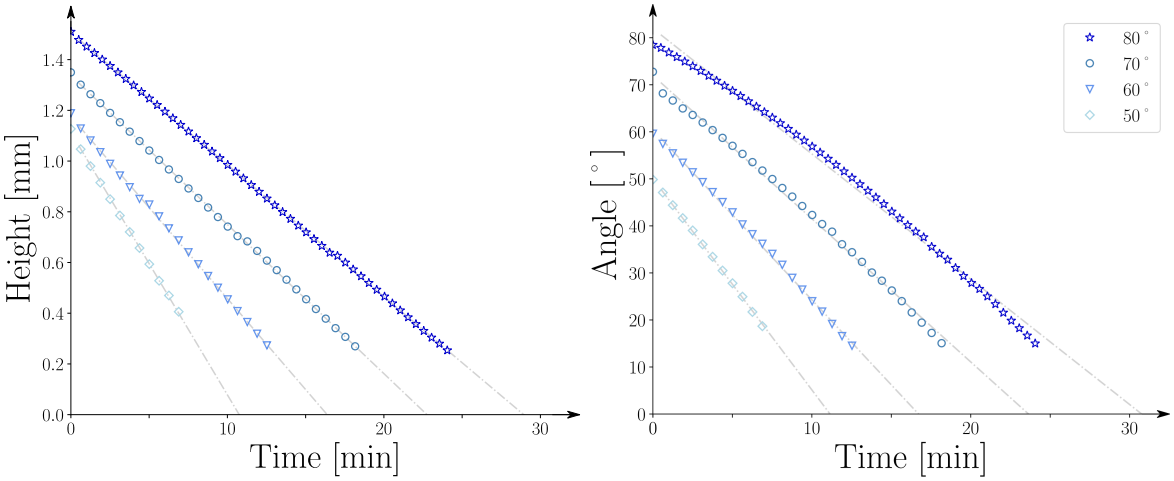

(a) (b)

Fig. 4.28 – (a) Comparison of the height evolution in time. (b) Comparison of the contact angle evolution in time. Different initial contact angles are tested to observe the influence of the angle on the dynamics ($V_0 = 10\mu$L and $RH = 0\%$).

From the height and the contact angle, while considering the initial contact radius, the volume of the droplet is calculated over time (Fig. 4.29a). Again the linear decay dynamics is found for the different study cases. However, the slopes are different for each case. Comparing the volumes, as the initial volumes are identical, it is very clear that the decay is faster when the initial contact angle is smaller. The evaporation is faster when the initial contact angle is lower: the final evaporation time is about 12 minutes when the initial contact angle is 50° while for an initial contact angle of 80° the final evaporation time is around 30 min.
We can relate these observations to the evaporation rate of the droplet which is given by the Hu and Larson approximation (Eq. 4.20). We notice with this relation that the evaporation rate depends on the contact angle according to a power law. By calculating the evaporation rate for each angle tested, it appears that the power law is well verified (Fig. 4.29b). The evaporation rate increases as the initial contact angle decreases as predicted by the formulation of Hu and Larson (Eq. 4.20). The smaller the contact angle becomes, the less influence it has on the evaporation rate, the points seem to tend towards a constant when $\theta < 40°$.

Finally, the volume is scaled by the initial volume V_0 and the time is scaled by the final time t_F for the four cases (Fig. 4.30). It appears that all the curves overlap and follow the same decreasing wit a slope of 1. This highlights the fact that changing the initial contact angle only affects the evaporation rate but not the dynamics of the system: the linear behavior is the signature of the pinned evaporation.

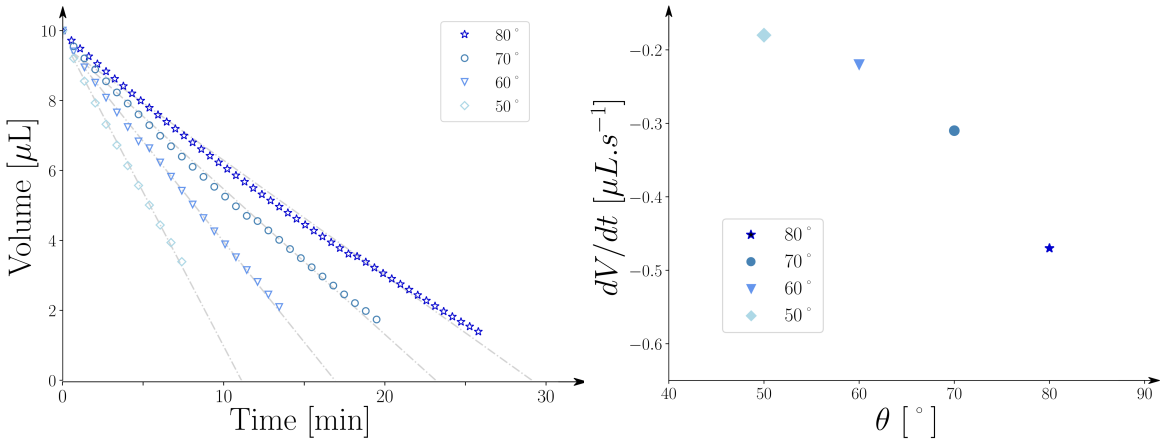

(a) (b)

Fig. 4.29 – (a) Comparison of the volume evolution in time. (b) Evaporation rate as function of the contact angle θ. Different initial contact angles are tested to observe the influence of the angle on the dynamics ($V_0 = 10\,\mu$L and $RH = 0\%$).

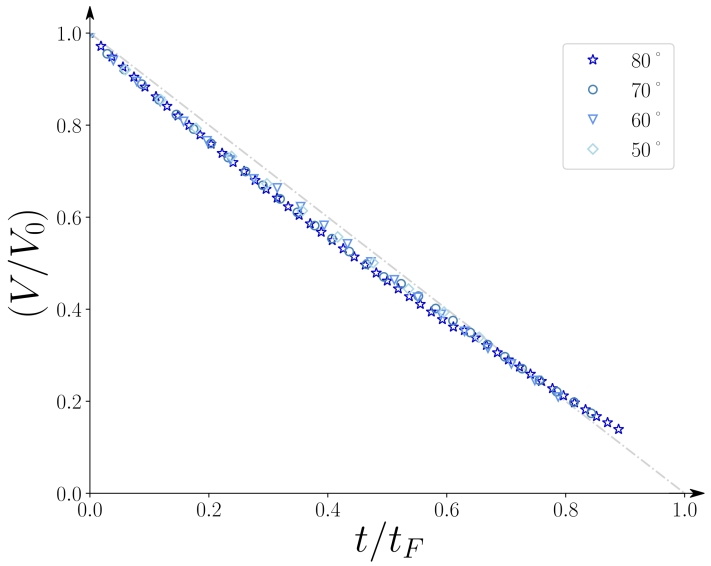

Fig. 4.30 – Scaled volume (V/V_0) as function of the scaled time t/t_F. Different initial contact angles are tested to observe the influence of the angle on the dynamics ($V_0 = 10\,\mu$L and $RH = 0\%$).

To conclude this first parametric study, it is important to emphasize that the numerical model built with Basilisk correctly reproduces the expected evaporation dynamics. The numerical results were validated by showing that the linear behavior of the droplet geometrical parameters (angle, height and volume) was well found for the different values of initial contact angle tested. This linear behavior is the typical behavior of a pure water droplet evaporating in the pinned mode. Moreover, the theoretical relationship between the evaporation rate and the contact angle was verified.

Variation of the relative humidity

The relative humidity is modified for each of the simulations to analyze its influence on the evaporation dynamics. Four humidities are considered: 0, 20, 40 and 60%. The same droplet is studied for each case, it is simply the environment in which it evaporates that is modified through the value of the humidity. The temperature of the environment remains unchanged with an ambient temperature of 25°C. The initial contact angle is 70° and the initial volume is 10μL. The evolution of the droplet's geometrical characteristics, height, contact angle and volume, are followed over time. The linear decay dynamics is found for the evolution of the height (Fig. 4.31a), the contact angle (Fig. 4.31b) and the volume (Fig. 4.32a).

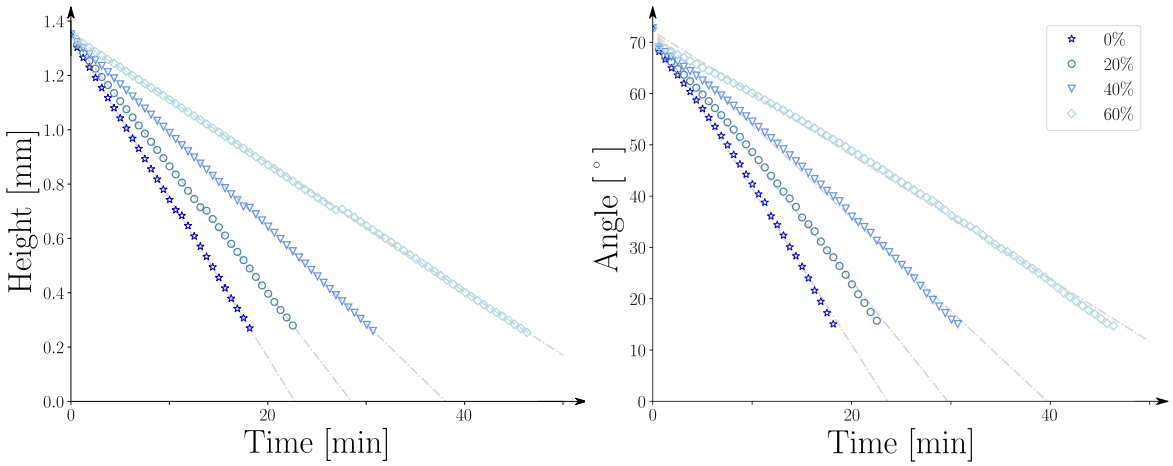

(a) (b)

Fig. 4.31 – (a) Comparison of the height evolution in time. (b) Comparison of the contact angle evolution in time. Different relative humidities are tested to observe the influence of the humidity on the dynamics ($V_0 = 10\,\mu$L and $\theta_0 = 70°$).

Comparing each of the cases, it is evident that the influence of relative humidity lies in a change in evaporation rate since the slopes are different. The physical interpretation of these results is consistent since a droplet placed in a very humid atmosphere evaporates more slowly than a droplet placed in a dry atmosphere. To confirm that the numerical model correctly reproduces the effect of relative humidity on the evaporation phenomenon, the evaporation rate is calculated for each case tested (Fig. 4.32b). The evaporation rate indeed decreases when the relative humidity increases. The linear relationship between evaporation rate and relative humidity is in agreement with the theoretical expression of evaporation rate (Eq. 4.20).

Finally, the volume is scaled by the initial volume V_0 and the time is scaled by the final time t_F for the four cases (Fig. 4.33). It appears that all curves overlap and follow the same decreasing line of slope 1. This highlights the fact that changing the relative humidity only affects the evaporation rate but not the dynamics of the system itself: the linear behavior is the signature of the pinned evaporation mode. This parametric study on the relative humidity allows to validate once again the numerical model of Basilisk. Indeed, the numerical results are consistent with the theoretical laws.

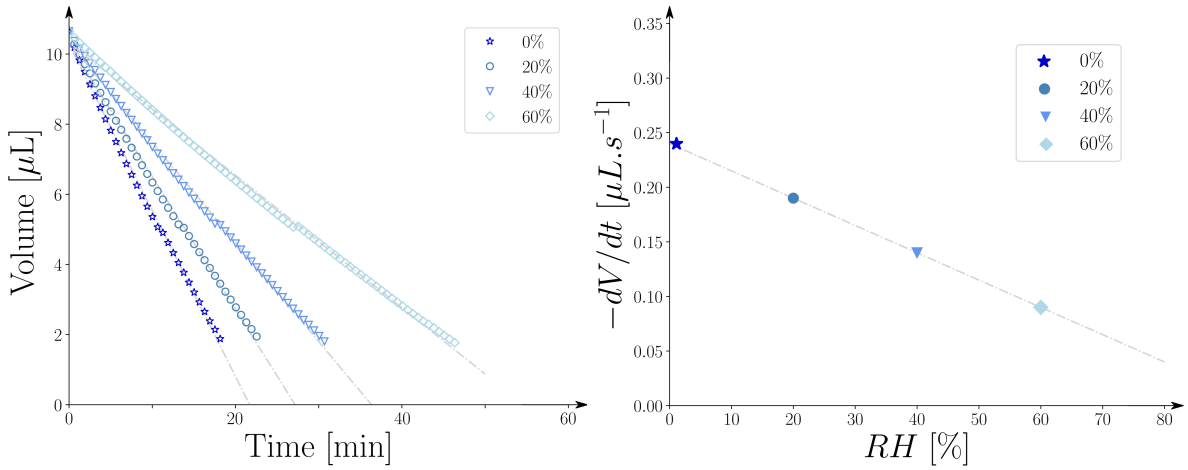

(a) (b)

Fig. 4.32 – (a) Comparison of the volume evolution in time. (b) Evaporation rate as function of the relative humidity RH. Different relative humidities are tested to observe the influence of the humidity on the evaporation dynamics ($V_0 = 10\,\mu$L and $\theta_0 = 70°$).

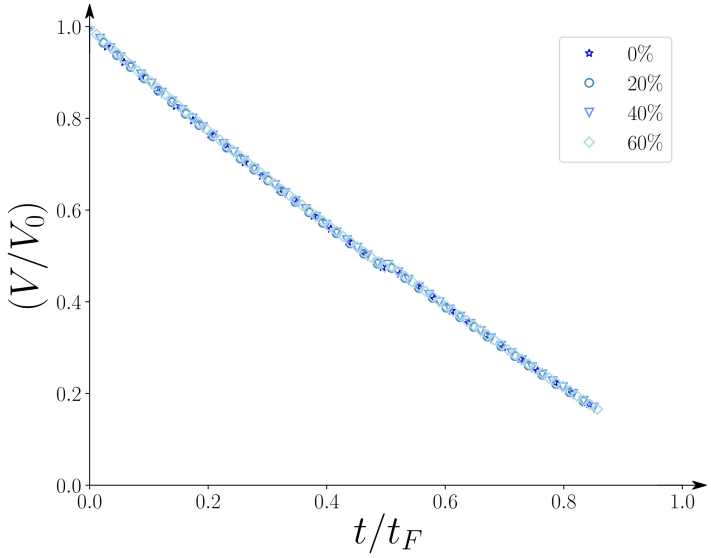

Fig. 4.33 – Scaled volume (V/V_0) as function of the scaled time t/t_F. Different relative humidities are tested to observe the influence of the humidity on the dynamics ($V_0 = 10\,\mu$L and $\theta_0 = 70°$).

What to remember ?

This chapter presents the numerical work done on the evaporation of pure water droplets. The development of new numerical implementations in Basilisk is a major point of the work. Taking into account the phase change during evaporation based on the calculation of the volume fraction is a simple and effective method that allows to represent accurately the physical phenomena. The implementation of a triple line anchoring condition to simulate the pinned evaporation mode was a numerical challenge. The results obtained are satisfactory and allow to validate the numerical model.

The validation of the model was made possible by the study of different cases and by the comparison with experimental data that we had previously obtained as well as with results from the literature. The numerical model allows to simulate spherical and sessile droplets. We have shown that the evaporation dynamics of spherical droplets simulated by the model follows well the theoretical d^2 law. The work on sessile droplets then allowed us to study the two evaporation modes separately.

For the unpinned mode, we showed that the d^2 law could be generalized as a power law to describe the evaporation dynamics. The exponent of the law is modified with respect to the d^2 law for pure water droplets since we find 0.63 instead of 0.5. This result had been demonstrated experimentally in the literature and allows us to validate the numerical results. The physical mechanism that would explain this difference is not yet very clear and several hypotheses have been put forward.

For the pinned mode, we found the linear decreasing behavior for the evolution of the contact angle, the droplet height and the volume with time. Using the experimental data presented in the previous chapter, the numerical results were confirmed. The triple line anchoring condition sets up a particular hydrodynamics within the droplet, with a capillary flow starting from the top to the edge of the droplet that we have highlighted during the study of velocity fields. This condition combined with the phase change also gives rise to a flow in the gas phase. We have shown the presence of a recirculation zone, which could possibly impact the evaporation dynamics of the droplet under certain conditions.

For both evaporation modes, parametric studies have been performed to analyze the impact of the initial contact angle and relative humidity on the evaporation dynamics. The effects were characterized through the calculation of the evaporation rate. It appears that the evaporation rate decreases when the relative humidity increases, since a high humidity minimizes the evaporation engine. This shows that the assumption of a purely diffusive evaporation when building the numerical model was correct. On the other hand, the evaporation rate increases as the contact angle decreases. The singularity of the evaporation flow at the triple line is accentuated for small angles.

To conclude, this work allows to build a reliable model on pure liquids, which will be then modified and embellished to reproduce the evaporation of mixtures, in particular saline droplets.

5 Experimental study of the evaporation of saline sessile droplets

In the previous chapters, we focused on the evaporation of pure water droplets. We now move to the study of saline sessile droplets from a experimental point of view in this chapter and from a numerical point of view in the following one.
To experimentally study the evaporation of salt solution droplets, a new experimental setup is described in the first section. In the second section, the evaporation dynamics of a saline droplet is analyzed, depending on the initial salt concentration.
The salt deposit left at the end of the evaporation forms various pattern that are interesting to observe. Its morphology depends on the initial salt concentration in the droplet and reflects the hydrodynamics taking place within the droplet during evaporation. The influence of relative humidity on the salt deposit is also considered. The third section presents a qualitative analysis of final patterns.
A focus is made on the patterns containing salt crystals in the fourth section.
Finally, experiments on evaporation cycles are introduced. Successive saline droplets deposited at the same location induce an interesting evolution of the salt pattern.
A part of the experimental results were obtained during the internships of Anaelle Givaudan and Paul Boumendil (2020/2021) and then Vu Hai La and Ilyass Rhani (2021/2022).

Contents

1 Experimental set-up and protocol

1.1 Set-up

The experiment consists in evaporating a saline sessile drop in a controlled environment. Fig. 5.1 shows a schematic illustration of the experimental setup for observing the evaporation process of sessile droplets. The same laboratory glove box than for evaporating pure water droplets is used (Fig. 3.2) but we improved the experimental set-up by adding another camera to obtain the **top view**.
The protocol remains roughtly the same as the one described for the study of pure water droplets (see Chapter 3). However, the addition of an extra camera requires synchronizing the shots from the two cameras in order to obtain the top and side views for the same time. The salt deposit obtained at the end of evaporation is photographed separately to obtain high quality pictures where the salt crystals are as sharp as possible. The two points that differ from the experiments with pure water are the salt solution to prepare and the substrate used. These two points will therefore be detailed.

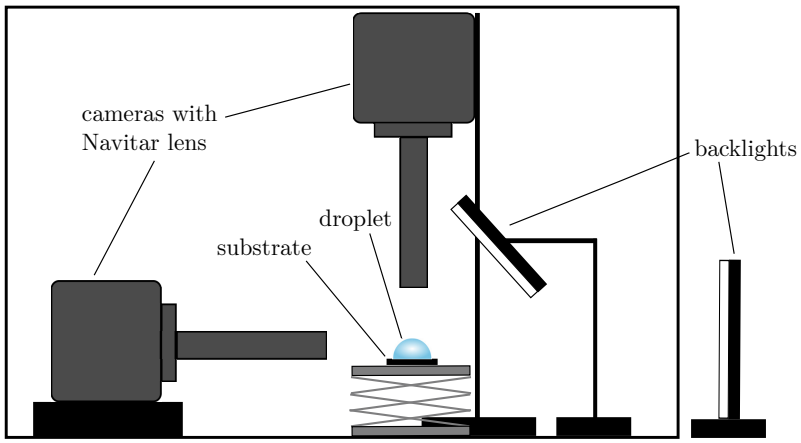

Fig. 5.1 – Schematic illustration of the experimental set-up for the study of the evaporation of saline sessile droplets. Two cameras are used to record the side and top views of the droplet during the evaporation.

Solid substrate

The solid substrate used for the evaporation of saline droplets is a **silicon wafer** supplied by SIL'TRONIX Silicon Technologies. The silicon wafer is single-sided polished, with a surface roughness less than 5 Å. This means that the surface is smooth. As in the first experiments with pure water, we want the droplet to evaporate according to a single evaporation mode during the whole time. The droplet contains salt and therefore the droplet is pinned to the substrate because of salt particles nucleation at the triple contact line. We do not need a rough substrate to ensure the pinned mode of evaporation, this is why we used in this case a smooth silicon wafer. Besides, as the droplet contains salt, the contact with a copper substrate would have generated corrosion under the droplet, which would have modified the dynamics of the system [17].
A silicon wafer can be used several times, for different experiments. Between each experiment, it is rinsed with distilled water to remove the salt deposit and cleaned with acetone. After four uses the wafer is changed because the surface can be damaged during handling and cleaning. The sessile droplet is deposited by a **single channel micropipette** (model

VE100, VWR Signature Ergonomic High-Performance Pipettor, droplet volumes from 10 μL to 100 μL) onto the silicon wafer.

Saline solutions

We are interested in saline droplets. The chosen salt is **sodium chloride (NaCl)** since it is the main salt dissolved in sea water. This is therefore consistent with the context of this study: we are seeking to characterize the sessile droplets deposited on structures because of the sea spray in marine environments. Sodium chloride is also widely used in the chemical industry to produce other compounds.
The saline solutions are prepared with Sodium Chloride NaCl (Sigma Aldrich) with salt concentrations ranging from 10^{-4} to 1.5 mol.L^{-1} NaCl. This range allows to represent the salt concentrations of several seas and oceans: for example for the Baltic Sea, the concentration is 6×10^{-2} mol.L^{-1} and for the Atlantic Ocean, the concentration is 4.6×10^{-1} mol.L^{-1}.

A first solution with the maximum salt concentration 1.5 mol.L^{-1} NaCl is prepared and then the others are made by dilution of the mother solution in distilled water. In order to better observe the crystals at the end of evaporation, some blue dye (e133) is added to the solutions. The dye quantity is so small that it is considered not to alter the properties of the solution (only few droplets in the mother solution of 500 mL).

We record the evaporation dynamics simultaneously from two sides with Nikon D810 cameras equipped with Navitar lens every 15 seconds. In order to obtain high quality photos, the set-up is illuminated from the side and the top with two backlights.
The side view allows the continuous monitoring of the shape dynamics by measuring the contact angle, the height and the contact radius (Fig. 5.2a). It also enables to study the crystals emergence as shown in Fig. 5.2b. We can measure and compute the crystal height as function of time to understand their growth dynamics.
The top view gives another measure for the contact radius and allows to verify if the droplet is spherical (Fig. 5.2c), which was not possible with the previous experimental set-up used for pure water droplets. The top view also provides valuable information about the birth of the crystals and their dynamics during evaporation. The final topology of the sediment as shown in Fig. 5.2d provides quantitative and qualitative data for the understanding of the evaporation process.

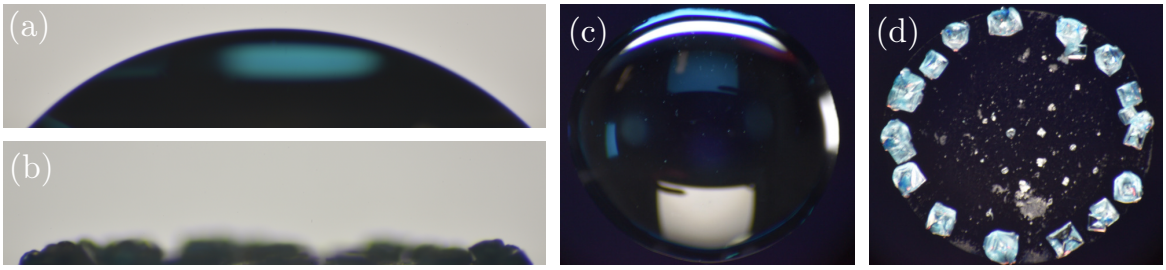

Fig. 5.2 – Side views of an evaporating sessile droplet of initial volume $V_0 = 10$ μL with 1 mol.L^{-1} of NaCl at $RH = 10\%$ at the initial state t=t_0 (a) and the end of evaporation $t = t_F$ (b). Top views for the same droplet at t=0 (c) and t_F (d).

1.2 Data analysis

To process the series of photos obtained during the experiments, we use the same tools as in the case of pure water, ImageJ and Python. For the side-view photos, the steps are identical, allowing to follow the height and angle over time. The details on the use of each tool as well as the data processing protocol are not recalled here, everything is explained in the Chapter 3.

The top view is used to check that the droplet is spherical and gives the average value of the contact radius. Indeed, during the deposition of the droplet, it can take an oval form (two examples are shown on Fig. 5.3 for a concentration of 10^{-2} mol.L^{-1}) if the manipulation of the pipette is not correctly done. The assumption of cap-sphericality is then no longer valid and the formula for calculating the volume based on geometrical relations can no longer be used. If this is the case, the experiment must be redone to obtain a spherical droplet. The top view also allows us to study the formation of crystals (Fig. 5.5). At the end of the evaporation, the picture of the deposit is analyzed with ImageJ to characterize its morphology. ImageJ allows for example to measure the width of the coffee-ring, the surface occupied by the deposit compared to the initial contact surface of the droplet, the size of the salt crystals and the distance between the crystals. This gives quantitative information to be able to compare the different deposits between them and to understand the influence of certain parameters such as the relative humidity.

The uncertainties on the data are the same as those quoted in the case of pure water. The modification of the experimental set-up and in particular the fact of placing from now on the cameras inside the glove box makes it possible to decrease the uncertainty of measurement on the detection of the interface. It is divided by two because the quality of the pictures is improved if they are not taken through the Plexiglas wall of the box. We have then $\delta = \pm 0.0015$ mm.
The analysis of the deposits is conditioned by their repeatability. For different initial salt concentrations, we have checked that we always obtain the same morphology of deposit (Fig. 5.3). Each salt deposit is in fact unique but some characteristics are identical at the same initial concentration. For deposits where salt crystals form, there are more differences, especially in terms of number and arrangement of crystals. We have therefore done four identical experiments for high salt concentrations in order to have averaged values (Fig. 5.3).

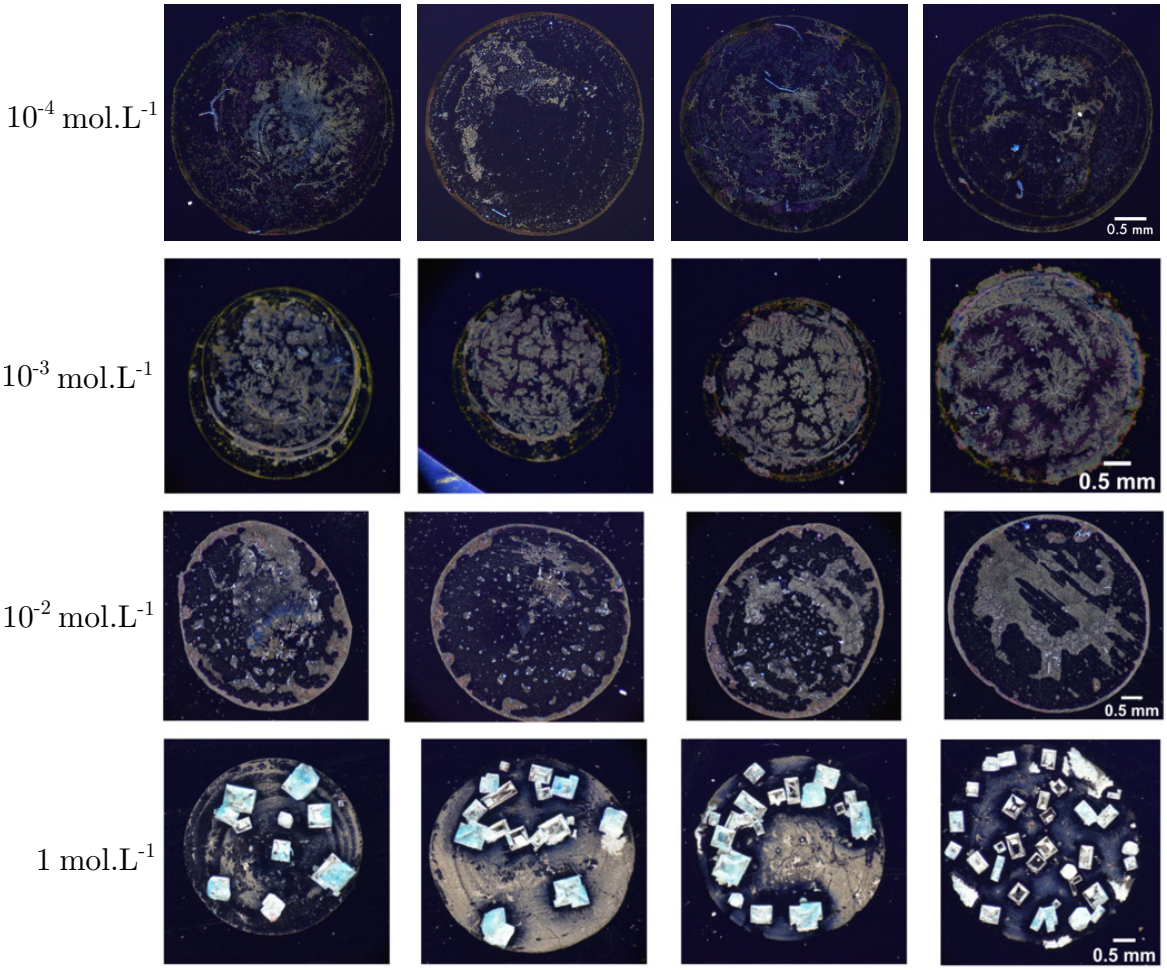

Fig. 5.3 – Repeatability analysis of salt deposits for four different initial sodium chloride concentrations. The initial volume is $V_0 = 10\,\mu$L and the relative humidity is $RH = 50\%$ for all the experiments. Four tests were performed for the same concentration in order to observe the variation of the deposit morphology under similar conditions.

2 Evaporation dynamics

Evaporation dynamics for an initial salt concentration of $1\,\mathrm{mol.L^{-1}}$

First, we are interested in the evaporation dynamics of the droplet of saline solution over time. A case is selected to be studied as an example. The initial volume is $V_0 = 10\,\mu\mathrm{L}$, the relative humidity is $RH = 10\%$ and the initial salt concentration is $c_0 = 1\,\mathrm{mol.L^{-1}}$. This is a fairly high concentration since the range studied is from 10^{-4} to $1.5\,\mathrm{mol.L^{-1}}$.

The series of pictures taken from the side and from above allow to follow the evolution of the droplet over time.
The side view (Fig. 5.4) shows the decrease of the droplet height during evaporation. The radius remains constant while the contact angle decreases. The droplet maintains a spherical heading shape until the salt crystals interact with the interface and deform it. This phenomenon appears at the end of evaporation, in the last few minutes. After complete evaporation of the water in the solution, the salt remains on the substrate and forms a deposit and we can measure the height reached by the crystals.

Fig. 5.4 – Side views of an evaporating sessile droplet of initial volume $V_0 = 10\ \mu\mathrm{L}$ with $1\,\mathrm{mol.L^{-1}}$ of NaCl at $RH = 10\%$, for different times during evaporation.

The top view (Fig. 5.5) allows to check that the droplet evaporates well according to a pinned mode and that the contact line does not detach at any point. The crystals start to appear on the pictures after about 20 minutes, when the water height is equivalent to the size of the crystals. This is why we show pictures of the end of the evaporation on the timeline (Fig. 5.5). We can see the crystals forming and growing as the evaporation proceeds. In this case, the initial salt concentration is high enough that the supersaturation condition is reached inside the droplet, at the triple line, and salt crystals form. Finally, at the end of evaporation, the salt deposit can be studied using the top view. More details on the crystals will be given in the Section 4.

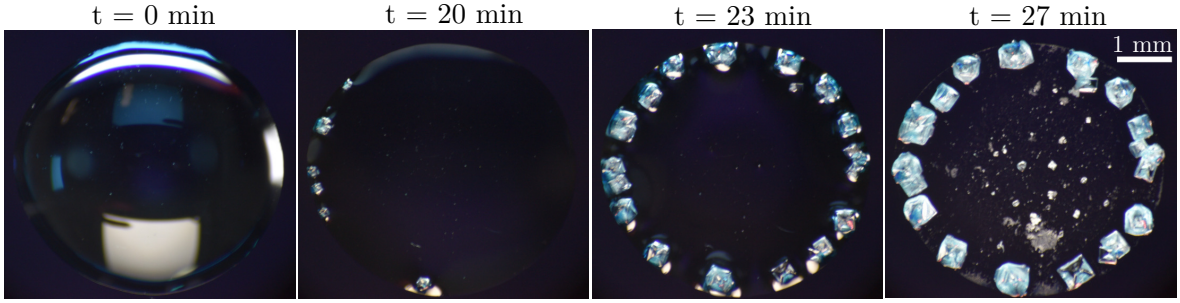

Fig. 5.5 – Top views of an evaporating sessile droplet of initial volume $V_0 = 10\ \mu\mathrm{L}$ with $1\,\mathrm{mol.L^{-1}}$ of NaCl at $RH = 10\%$, for different times during evaporation.

From the image analyse, the evolution of the droplet height is plotted over time (Fig. 5.6a). Two phases are observed: a first decreasing linear phase and a second increasing and constant phase. The Python routine used for image processing finds the maximum height in the pictures. At the beginning of the evaporation, the maximum height is that of the droplet.

Then at a certain time, the height of the crystals exceeds the height of the droplet. The maximum point in the picture is no longer the height of the droplet but the height of the largest crystal formed. This explains the two phases. When the crystals reach the interface, they deform it. It becomes impossible to calculate a contact angle or the volume of the droplet according to a geometrical approach of spherical cap. This is the reason why there is no experimental data at the end of evaporation for angle and volume (Fig. 5.6b and 5.7). The interection between the crystals and the droplet interface can also induces a displacement of the crystals towards the center of the pattern [114]. The first phase describes the evolution of the droplet height, following the linear decreasing behavior expected for the evaporation of a sessile droplet according to the pinned mode. We find the same dynamics as in the case of a pure water droplet. The second phase shows the growth of salt crystals, to be studied in the dedicated section 4.

The evolution of the contact angle is plotted against time (Fig. 5.6b). The initial contact angle formed by salt water on the silicon wafer is about 55°. The contact angle then decreases linearly. At the end of the evaporation, the salt crystals deform the interface of the droplet and make it impossible to measure a contact angle between the liquid and the substrate.

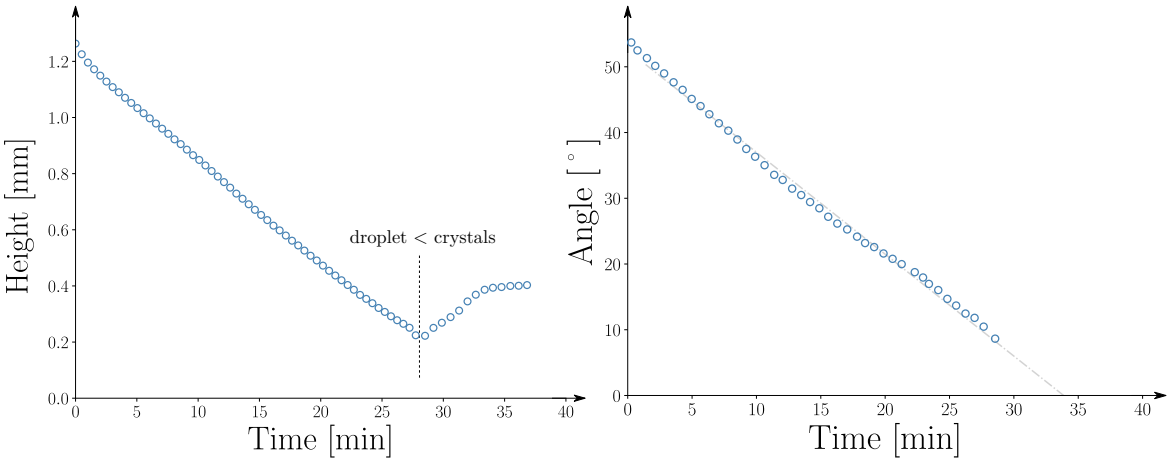

Fig. 5.6 – (a) Evolution the maximal height in time. In the first decreasing phase, the maximal height is the droplet height and in the second increasing phase, the maximal height is the crystal height. (b) Evolution of the contact angle in time. ($V_0 = 10\,\mu$L and $RH = 10\%$). The error bars are not shown on the figures for readability reasons because they are of a size comparable to that of the data markers.

Finally, the volume of the droplet is computed over time with the spherical cap assumption (Fig. 5.7). The volume of the droplet decreases linearly with time. The behavior is identical to that of a pure water droplet evaporating in the same pinned evaporation mode. The presence of salt in the droplet does not impact the shape of the law followed by evaporation dynamics. To go a little further, we modify the initial salt concentration to observe the influence of this parameter on the evaporation dynamics.

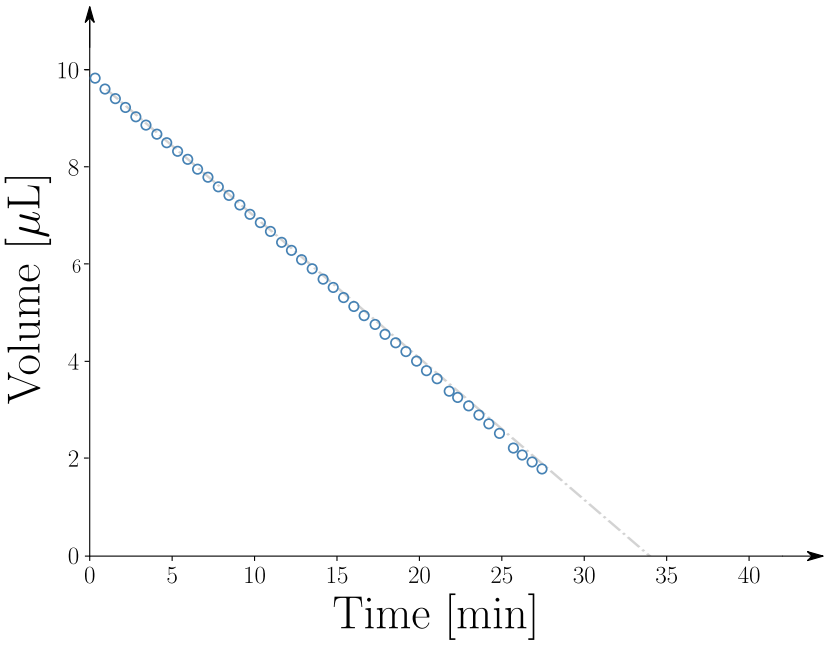

Fig. 5.7 – Evolution of the droplet volume as function of time for a saline droplet. ($V_0 = 10\,\mu$L and $RH = 10\%$)

Influence of the initial salt concentration

Three different initial salt concentrations are tested: 0.5, 1 and 1.5 mol.L^{-1}. The height of the droplet is measured over time (Fig. 5.8). For the three concentrations, the droplet height follows the same dynamics and decreases linearly in time. However, we observe that as the initial concentration increases, evaporation slows down. The slope of the line decreases and the evaporation time increases.
This slowing down of evaporation when the salt concentration increases has been observed experimentally [37] and can be explained with Raoult's law [115]. Sodium chloride being non-volatile, the addition of a non-volatile solute in the solution leads to a decrease in the vapour pressure of the solution. The presence of salt crystals formed along the contact line may also play a role in decreasing the evaporation rate. Indeed, the area close to the triple line tends to concentrate in salt while it is the place where the evaporation flow is normally the strongest. Because of the salt structures present at the triple line, water cannot evaporate easily at this point. The salt enrichment near the triple contact line slows down the evaporation flux [116]. However, this relative between initial salt concentration and evaporation flux varies depending on the substrate properties. The opposite effect is observed with a nanoporous substrate [117].
The comparison with a droplet containing no sodium chloride ($c_0 = 0\,$mol.L^{-1}) is not possible if we want to keep the same liquid/substrate couple. In this case, the evaporation mode changes which influences the evaporation rate and the evaporation dynamics, which would bias the comparison. Given the results obtained so far, we can predict that a droplet containing no salt should evaporate faster than saline droplets under the exact same conditions.

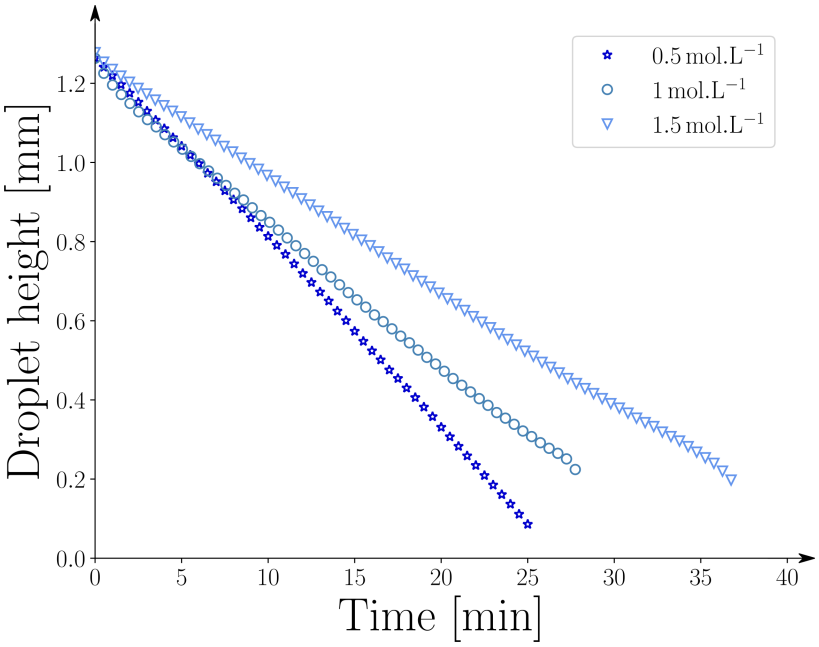

Fig. 5.8 – Evolution of the droplet height in time for three different initial salt concentrations. ($V_0 = 10\,\mu$L and $RH = 10\%$)

3 Qualitative analysis of final patterns

We focus on the study of the salt deposit patterns obtained after complete evaporation of the droplet. The saline deposit is a testimony of the hydrodynamics that has been set up in the droplet during the evaporation. Its analyse allows to understand the hydrodynamic flows that take place inside the droplet. The salt deposit is a function of several parameters: initial salt concentration, initial volume of the droplet and relative humidity.
We consider a droplet containing sodium chloride. Depending on the local salt concentration, the salt can precipitate and form crystals. This phenomenon does not happen when the droplet contains colloids and it explains why differences between colloidal and crystalline evaporative deposits are observed [118]. Indeed, the salt is completely dissolved in the droplet at the beginning of the evaporation and the nucleation and growth processes of the crystals complicate the dynamics within the droplet. Crystals will be studied in detail in the next section.

3.1 Patterns depending on the initial salt concentration

Description of the different patterns observed

First, we study the influence of the initial salt concentration on the morphology of the salt deposit, because the prediction of the morphology of the salt deposit is important in many industrial applications [114, 119, 120]. For example, in the case of corrosion, potential corrosion sites are often related to the areas where salt is deposited [121], where crystals form since this indicates a high local salt concentration at some point during evaporation. The droplet behaves like an electrolyte solution in corrosion problems, the more concentrated the droplet is in salt, the more conductive it is and the more electrochemical phenomena will be facilitated. To initiate corrosion, a critical concentration of NaCl must be reached: this value depends on the liquid material couple considered. For instance, for iron the critical value is between 10^{-4} and $3 \times 10^{-3}\,\mathrm{mol.L^{-1}}$ [122]. The most concentrated areas in the droplet are therefore those where corrosion takes place and where the salt crystallizes. If we are able to predict the salt deposits then we are able to predict the corrosion sites as they are both related to the hydrodynamics taking place inside the droplet.
A large range of initial concentrations is tested, from 10^{-4} to $1.5\,\mathrm{mol.L^{-1}}$. If the salt concentration is too low, then the droplet evaporates according to a unpinned mode [37]. To be able to compare the droplet behaviors and really study the impact of the initial salt concentration, it is necessary to ensure that the droplets evaporate according to the same mode. The lowest concentration tested is therefore chosen to allow the anchoring of the triple line during evaporation. For the maximum concentration tested, we remain below the saturation limit concentration which is $c_{sat} = 6.1\,\mathrm{mol.L^{-1}}$ for sodium chloride in water. The salt deposits obtained for each concentration are shown in Fig. 5.9.

As the initial salt concentration increases, the deposit changes and salt crystals appear. For low concentrations $c_0 = 10^{-4}\,\mathrm{mol.L^{-1}}$, a **coffee-ring pattern** is obtained (Fig. 5.9a). Salt is accumulated at the triple line of the droplet and forms a ring. For concentrations below $10^{-3}\,\mathrm{mol.L^{-1}}$, the deposit is of coffee-ring type.

When the initial salt concentration reachs to $5 \times 10^{-3}\,\mathrm{mol.L^{-1}}$, the deposit evolves. As it goes on, the distribution of salt changes: salt is deposited at the triple line but also at the center of the droplet. The amount of salt deposited in the center of the droplet increases with the initial concentration. The coffee-ring becomes less and less pronounced. When the

initial salt concentration reaches 7.5×10^{-3} mol.L^{-1}, the salt deposit is **uniform** and covers the entire contact surface previously occupied by the droplet (Fig. 5.9b).

For a salt concentration approaching approximately 5×10^{-2} mol.L^{-1}, **crystals** are observed. A thin layer of salt still remains on the substrate. The thin layer of salt decreases as the salt crystallizes to form larger structures. For example, we clearly observe a distribution of salt crystals at the triple line when $c_0 = 7.5 \times 10^{-2}$ mol.L^{-1} (Fig. 5.9c). A thin layer of salt on the substrate occupies a smaller and smaller area.

When the initial salt concentration increases further and exceeds 10^{-1} mol.L^{-1}, **larger crystals** are formed. They are distributed on the contour of the deposit and also in the center. From 7.5×10^{-1} mol.L^{-1}, a transition takes place again and the morphology of the deposit changes (Fig. 5.9d). The number of crystals decreases drastically but their size increases.

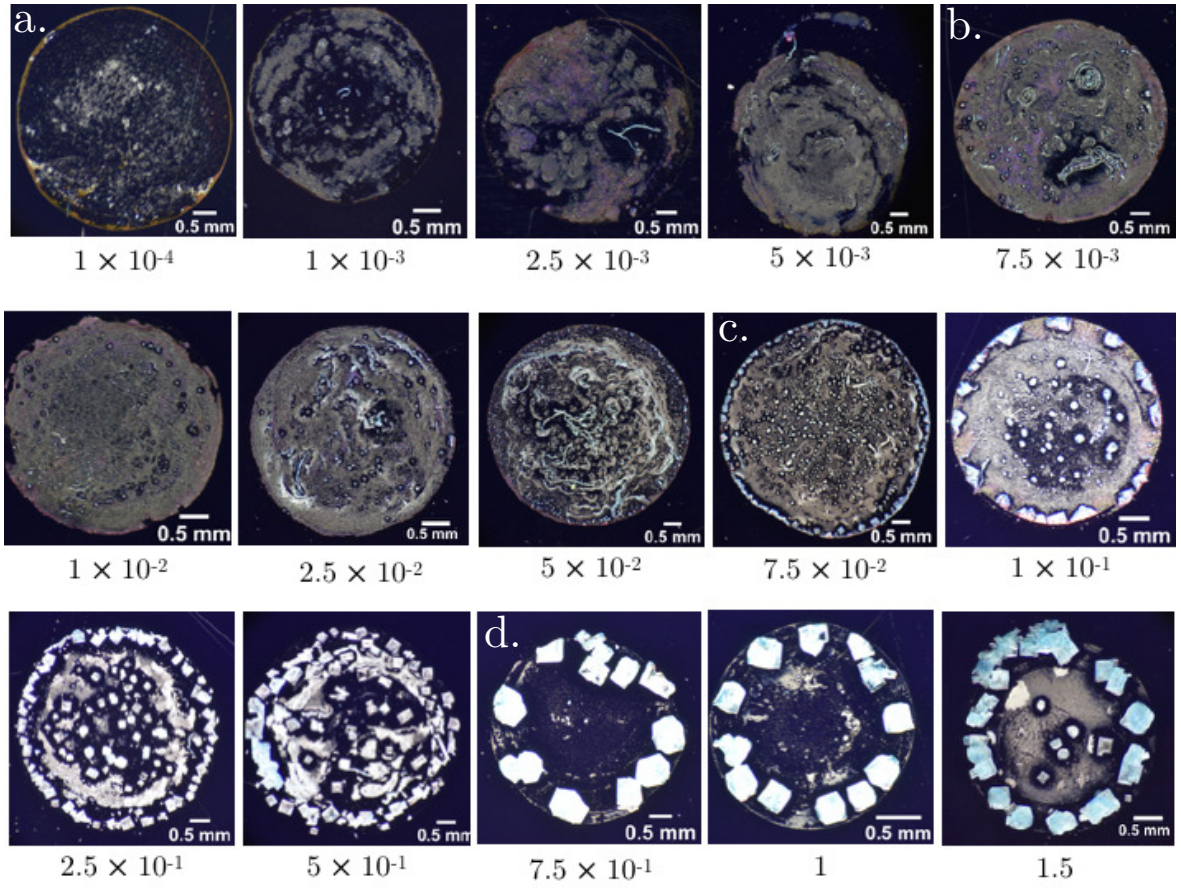

Fig. 5.9 – Deposit patterns obtained after evaporation depending on the initial salt concentration. The concentration c_0 varies between 1×10^{-4} and 1.5 mol.L^{-1} from the top left to the bottom right. ($V_0 = 10\,\mu$L and $RH = 10\%$)

It is clear that the solute concentration has an influence on the final deposition pattern. The morphology of the deposit evolves around certain values of initial salt concentration that this study has brought forward. For concentrations below 10^{-3} mol.L^{-1}, the deposit is of coffee-ring type. Then between 10^{-3} and 5×10^{-2} mol.L^{-1} the deposit is uniform. Numerous small salt crystals then appear before gathering to form larger crystal structures from 7.5×10^{-1} mol.L^{-1}.

Discussion

For low concentration, a **coffee ring deposit** is observed. This deposit has been extensively studied, notably by Deegan [68,89,123] who was the first to explain the hydrodynamics leading to the formation of the coffee-ring pattern. When the droplet evaporates in a pinned mode, depending on the contact angle, the liquid evaporating at the triple line must be compensated by liquid coming from the center of the droplet. This sets up a flow that is called **capillary flow**, which brings all the salt present in the droplet (represented with red dots) to the triple line during evaporation (Fig. 5.10). The same phenomenon occurs in the case of a pure water droplet evaporating in the pinned mode. The driving force behind this flow is not the presence of salt but the anchoring of the triple line and the spherical cap condition. The salt then behaves as a passive tracer due to its low concentration, it does not affect the properties of the liquid. The supersaturation condition is not reached at any point in the droplet and no crystal is formed because the initial concentration is too low. The behavior of the salt is identical to that of colloids.

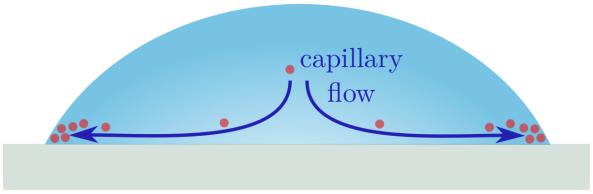

Fig. 5.10 – Formation of the coffee-ring salt pattern. The capillary flow induced by the pinned mode of evaporation transports the salt (red dots) from the center of the droplet to the triple contact-line.

By increasing the initial concentration of salt, the hydrodynamics inside the droplet evolves. The increasing amount of salt deposited at the triple line is related to the establishment of a **Marangoni flow** within the droplet. As capillary flow builds up within the droplet to compensate for the high evaporative flow at the triple line, salt accumulates at the edge of the droplet. The salt concentration is therefore higher in the contact line region than at the top of the droplet. The surface tension depends on the solute concentration and varies locally with the concentration (Eq. 1.2). It increases with the concentration which means that the surface tension is stronger at the triple line than at the top of the droplet. This creates a surface tension gradient which gives rise to a flow directed from the top of the droplet towards the edge of the droplet which is called Marangoni flow. This flow eventually participates in transporting even more solute towards the contact line, like the capillary flow (Fig. 5.11a). The presence of a very low Marangoni flow can therefore give rise to a coffee-ring type deposit. The Marangoni flows is observed depending on c_0 and the relation between the surface tension and the concentration (Fig. 5.11b).

At a certain point, when the surface tension gradients become too large, i.e. when the initial salt concentration increases, the liquid supply at the corner of the droplet exceeds the amount of liquid lost during evaporation. To ensure equilibrium and mass conservation at the triple line, **recirculation cells** appear in the droplet. This prevents salt from accumulating in the triple line and leads to a more homogeneous distribution of salt in the droplet. Thus, the resulting deposit is a thin layer of salt over the entire area initially occupied by the droplet: this is referred to as a **uniform deposit** (Fig. 5.12). It is important to keep in mind that the mechanisms take place one after the other, in a certain order. The constraints linked to the geometry of the droplet and the evaporation mode lead to the capillary flow from the beginning of the evaporation. This flow transports salt to the triple line which locally increases the surface tension and gives rise to the Marangoni flow. This second flow transports even more liquid towards the edge of the droplet until recirculation cells are created. When the initial concentration of solute increases, the same phenomena take place but the Marangoni

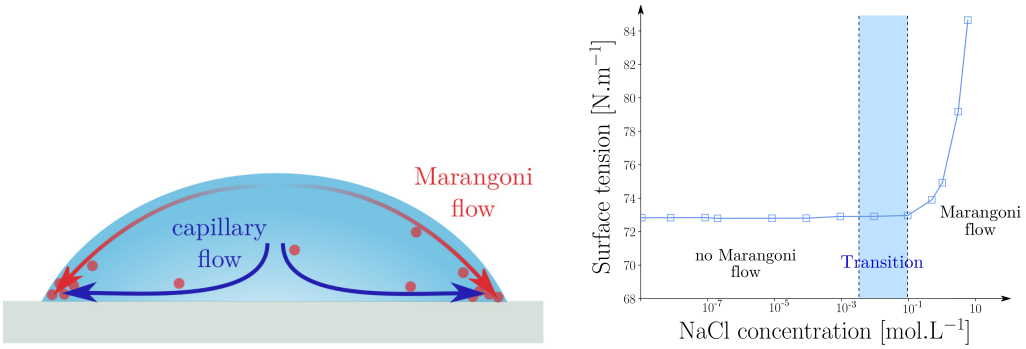

(a) (b)

Fig. 5.11 – (a) Participation of the Marangoni flow in the coffee-ring pattern. The Marangoni flow is low but transports salt (red dots) to the contact line. (b) Observation of Marangoni flow related to the relation between surface tension and salt concentration.

flow appears more quickly and with a stronger intensity. Again the initial salt concentration is too low to form crystals.

Fig. 5.12 – Formation of the uniform pattern. The quantity of liquid supplied at the contact line is too large compared to the evaporation flow so recirculation cells are created.

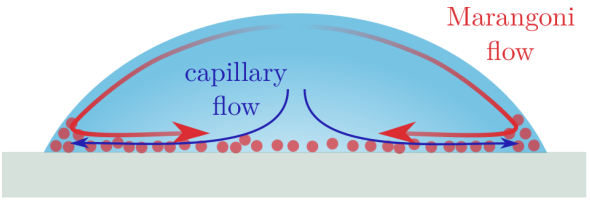

For concentrations equal or bigger than approximately 5×10^{-2}mol.L^{-1} NaCl, the condition of crystallization is reached and gives rise to crystals. This condition is initially exceeded in the regions where the salt accumulates, i.e. along the contact line. A thin layer of salt still remains on the substrate, occupying a smaller and smaller area. From $c_0 = 1\,\text{mol.L}^{-1}$, large crystals are formed on the triple contact line (Fig. 5.13). This can be explained by the fact that it is energetically more favorable to grow already existing crystals than to form new ones. Since the first crystals form at the triple line since this is where the salt is delivered in the first place, it seems consistent to observe the crystals distributed at the contact line. A hydrodynamic argument has also been put forward by Efstratiou [124]. This will be explained in the section on crystal formation.

Fig. 5.13 – Formation of the salt crystals. At one point, the saturation concentration is reached near the triple contact line and crystals start to growth from there.

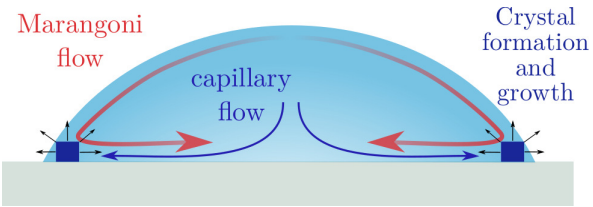

3.2 Patterns depending on the relative humidity

Description of the different patterns observed

In this last part, the influence of relative humidity on the morphology of the salt deposit is studied. Three humidities are considered 10, 30 and 50% and five different initial salt concentrations from 10^{-4} to 1 mol.L^{-1} (Fig. 5.14).

For the lowest concentration, a coffee-ring shaped deposit is obtained regardless of the relative humidity. For $c_0 = 10^{-3}\,\text{mol.L}^{-1}$, the patterns obtained for humidities of 10 and 30 % are similar (Fig. 5.14 a.1 and b.1): it is the transition between the coffee-ring and the uniform deposit. The deposit obtained in a relative humidity of 50% is closer to a coffee-ring than to a uniform deposit (Fig. 5.14 c.1). The ring is well marked and wider than for a lower concentration. Salt is deposited in small spots in the center of the ring.
When the initial concentration increases again and reaches $c_0 = 10^{-2}\,\text{mol.L}^{-1}$, the three deposits are identical regardless of the relative humidity considered. The salt is distributed on the surface of the substrate and forms a uniform deposit. The first tiny crystals can be observed from this concentration. For $c_0 = 10^{-1}\,\text{mol.L}^{-1}$, salt crystals appear in all three deposits, but with some differences. For $RH = 10\%$ and $RH = 30\%$ (Fig. 5.14 a.4 and b.4), the largest crystals and the majority of the crystals are located at the triple line while for $RH = 50\%$, the crystals are distributed in the center of the deposit (Fig. 5.14 c.4). As the relative humidity increases, the crystals are smaller. The number of crystals also seems to decrease with increasing humidity.
Finally, for the last concentration tested $c_0 = 1\,\text{mol.L}^{-1}$, we observe large crystals in the three deposits. The same observation as for the previous concentration can be made: for the two lowest humidities, the crystals are localized at the triple line and are more numerous (Fig. 5.14 a.5 and b.5). For $RH = 50\%$, the crystals are in the center of the deposit without particular arrangement (Fig. 5.14 c.5).

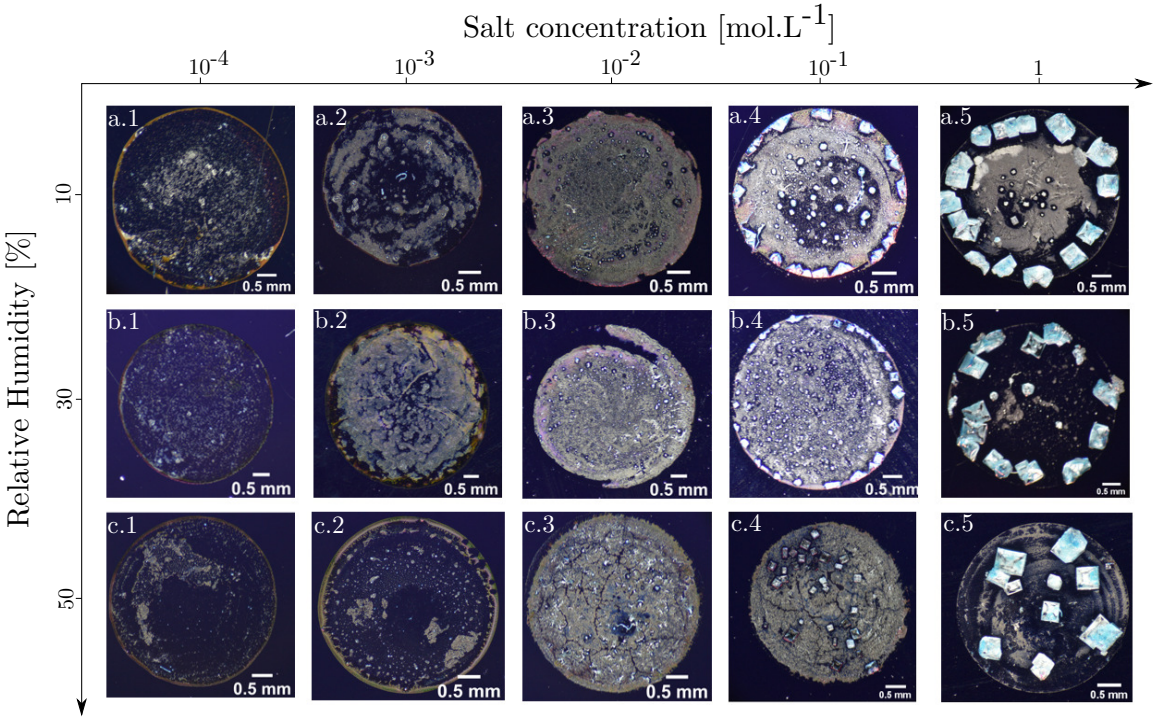

Fig. 5.14 – Salt deposits obtained after evaporation depending on the initial salt concentration and the relative humidity.

Discussion

For the lowest salt concentration, the relative humidity doesn't impact the pattern with the presence of the coffee ring. The evaporation of sessile droplets does not depend on the environmental relative humidity in the sense that the evaporation dynamics is the same [37].

Capillary flow drives fluid towards the contact line. Then, the NaCl is driven outward with the water and forms a ring along the contact line, when the drop is completely dried. An increase of the concentration to the value of $10^{-3}\,\mathrm{mol.L^{-1}}$ leads to different patterns as a function of the relative humidity. If the humidity is higher, then evaporation is slower. One can imagine that the hydrodynamic processes are also slower and take longer to set up. This could explain why the resulting deposit is still coffee-ring like when the relative humidity is 50%, whereas it has already transitioned to a uniform deposit at lower humidities. More generally, the different patterns show that a lower relative humidity quickly leads to areas of high sodium chloride concentration since the driving force for evaporation is more important. The condition of crystallization is thus more easily reached and gives rise to crystals, which will then grow. On the contrary, a high relative humidity leads to a slower evaporation rate which produces a slower capillary drift towards the droplet edge. As the evaporation rate is slow, the salt ions has more time to diffuse towards the formed crystal nuclei. As a result bigger crystals emerged when the relative humidity increases, particularly for $1\,\mathrm{mol.L^{-1}}$.

As a conclusion, relative humidity seems to play a more determining role for high initial salt concentrations. In particular, when crystals are formed in the salt deposit, differences in the morphology of the deposits are observed. The position of the crystals follows the contact line for the two lowest humidities, whereas the crystals are randomly distributed in the center of the deposit for the highest humidity. As the relative humidity increases, the evaporation process slows down as the water vapor concentration gradient decreases. This difference in dynamics can explain the deposits obtained. These first observations, especially on the crystals, motivate a second study on the influence of the relative humidity on the formation and growth of salt crystals in Section 4.

4 Focus on the patterns containing salt crystals

During the evaporation of the droplet of saline solution, only the solvent, namely water, will evaporate because sodium chloride is a non-volatile solute. This solute initially entirely dissolved in the droplet since we consider initial concentrations lower than the condition of supersaturation, will then be able to precipitate and crystallize. This gives rise to salt crystals, which are complex structures with many properties. In this section, we first focus on the formation of crystals, relying on the internal hydrodynamics of the droplet to explain the process. The growth of the crystals is then studied, in particular by following the evolution of the height of the crystals over time. Finally, the influence of the relative humidity on the growth of the crystals and on the salt deposit obtained after complete evaporation is studied.

4.1 Apparition of salt crystals

A droplet of initial volume $V_0 = 10\,\mu$L with an initial concentration of $c_0 = 1\,\text{mol.L}^{-1}$ in a relative humidity $RH = 10\%$ is studied. From the top view of the droplet, we can observe the formation of the salt crystals during evaporation (Fig. 5.15). The droplet evaporates in the constant contact area mode, where the contact angle decreases whereas the contact radius is constant in time. The triple contact line is then pinned. This evaporation mode leads to a compensation flow from the center of the drop to the contact line called capillary flow, which maintains the spherical shape of the drop despite the strong evaporation flow at the triple line [68].
After about 19 minutes of evaporation, the crystals are visible on the pictures from the top view: the characteristic height of the crystals becomes comparable with the height of the droplet interface. The first crystals appear on the edges of the droplet, at the triple line.
When the saline droplet evaporates, as it is a solute/solvent mixture, the salt which is a nonvolatile solute is carried by the capillar flow to the edge of the droplet. It becomes supersaturated in the vicinity of the contact line as the water evaporates [118]. This will lead to crystal nucleation at the triple contact line. The contact line area is the most concentrated zone in the droplet so it is coherent to observe the first crystals there.

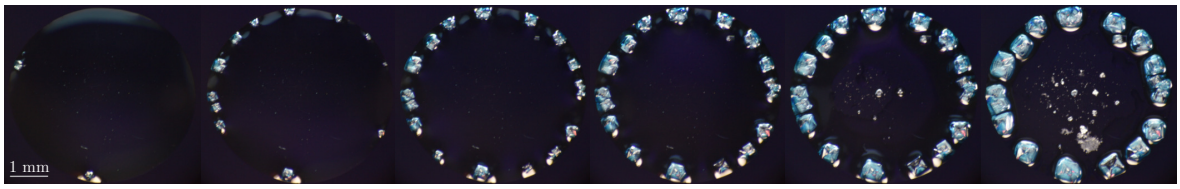

Fig. 5.15 – Top views of an evaporating sessile droplet of initial volume $V_0 = 10\ \mu$L with $1\,\text{mol.L}^{-1}$ of NaCl at $RH = 10\%$. The formation of salt crystals is observed at the end of evaporation, from $t = 19$ min 45 sec to $t = 24$ min 45 sec, every minute.

As evaporation continues, more and more crystals appear around the perimeter of the droplet. The crystals are evenly distributed and grow larger as they grow. The preferred direction of crystal growth is toward the center of the droplet. They also grow in height simultaneously. This seems consistent since at this stage of evaporation, the remaining liquid is mostly in the middle, surrounded by this discontinuous ring of crystals (there is also liquid between the crystals). Efstratiou [124] demonstrated the presence of flows directed towards the forming crystals using a micron resolution particle image velocimetry technic (micro-PIV). The fact that the already created crystals grow rather than new crystals are formed is justified by vortices localized on the sides of the crystals. Indeed, the salt deposit at the

triple line is formed by a succession of well-distinct salt crystals and not by a continuous salt ring. The mechanism proposed by Efstratiou justifies this discontinuous structure. Another mechanism had been previously proposed by Takhistov [125]. At the end of the evaporation, some small crystals remain in the center of the droplet. One can imagine that this quantity of salt did not have time to be transported to the triple line, the water evaporating, the condition of supersaturation and crystallization must have been reached.

Several questions remain unanswered about the appearance and formation of salt crystals during evaporation: when do the crystals appear, why do they form in a regular distribution along the triple line ? The second question will be further investigated in the next part 4.3. Regarding the timing of the crystals, from the pictures (Fig. 5.15), most of the crystals seem to form all at the same time, at a specific moment of the evaporation. When the edge of the droplet becomes very concentrated in salt, the local concentration exceeds a critical concentration that causes the supersaturation limit (also called the metastable limit) to be exceeded (Fig. 5.16). When this limit is reached, the conditions are met for nucleation to take place. Nucleation points appear along the triple line and salt crystals will form. As long as the supersaturation limit is exceeded, crystals will form [126]. However, the precipitation of salt results in a decrease in the salt concentration of the solution. So as soon as crystals start to form and grow, the salt concentration inside the droplet will decrease, until it finally falls below the supersaturation limit (Fig. 5.16). This explains why the crystals are formed in a specific time lapse and that new crystals are not formed later. Moreover, it is energetically more favorable to grow existing crystals than to form new ones.

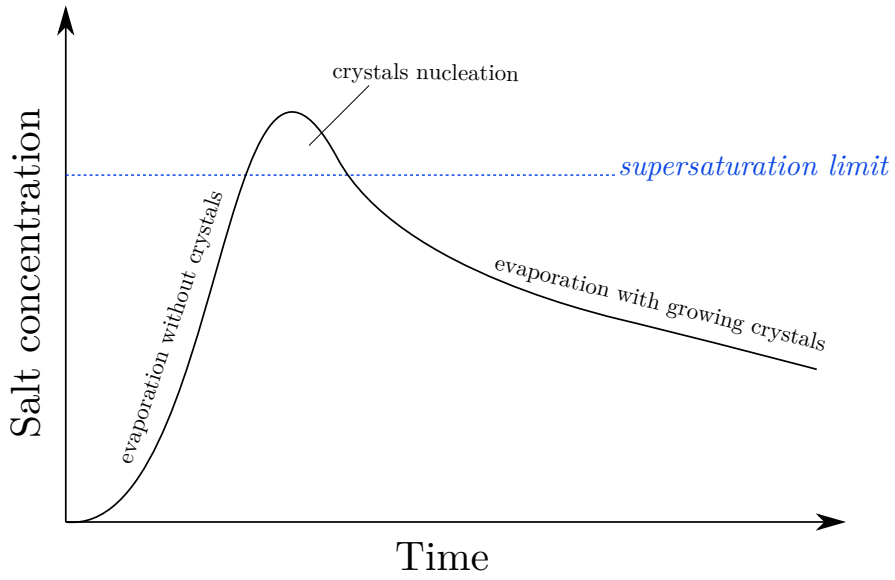

Fig. 5.16 – Evolution of the salt concentration in time along the evaporation. When the salt concentration exceeds the supersaturation limit, crystals nucleation occurs.

4.2 Crystals growth

As explained earlier, tracking the maximum point of droplet height provides access to a measure of vertical salt crystal growth. When the typical crystal size exceeds the maximum height of the droplet interface, we begin to measure the evolution of the crystal height. This does not track any particular crystal, but only the largest crystal. This study is a first experimental approach that we thought interesting to explore. Many improvements are

possible to allow a more specific monitoring of the growth of crystals during evaporation. For instance, the top view of the droplet gives acces to the lateral growth of the salt cystals.

The time when the maximum height of the crystals exceeds the maximum height of the droplet is noted t^*. The tracking of the crystals starts when they are already formed and have a height of a few tens of micrometers. The height of the largest crystal is plotted as a function of time t^* (Fig. 5.17). Two phases are observed. First, a growth phase that seems to follow a linear trend. Then, the growth slows down and stops at the very end of the evaporation. Physically, the linear growth phase corresponds to a constant supply of salt from the salt solution to the crystal. This is consistent with the currents directed towards the crystals observed experimentally by Efstratiou [124]. At the end of the evaporation, the amount of solvent remaining in the droplet being very small, these currents, and the flows in general in the droplet slow down and stop. The salt supply to the crystals is therefore no longer assured.

The maximum height reached by the largest crystal at the end of evaporation is about 0.215 mm.

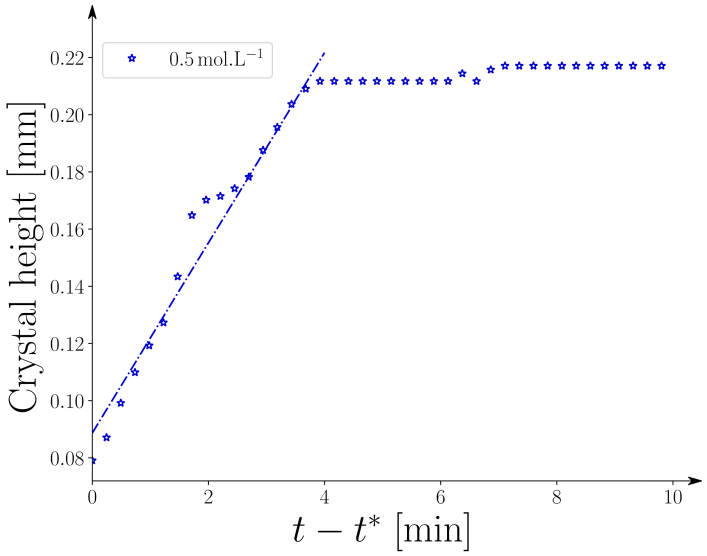

Fig. 5.17 – Crystal height as function of time $(t^* - t)$, where t^* is the time where the maximal crystal height exceeds the maximal droplet height. The initial salt concentration is 0.5 mol.L^{-1}. ($V_0 = 10\,\mu$L and $RH = 10\%$)

Influence of the initial salt concentration

Crystal growth is compared for three experiments performed under the same conditions but with different initial sodium chloride concentrations, from 0.5 to 1.5 mol.L^{-1} (Fig. 5.18). Salt concentrations sufficient to form crystals on evaporation should be considered. Whatever the initial concentration tested, two phases are always observed: a first phase of linear growth and a second phase at the very end of evaporation where the height does not increase anymore. During the linear phase, the growth rate G does not seem to be impacted by the change in initial concentration since very similar values are found, $G \sim 10^{-7}$ m.s^{-1}. This is coherent with the theoretical growth rate of NaCl crystals [127]. Depending on the initial concentration, the crystals do not have the same maximum sizes. When the initial concentration increases, the maximum size also increases. The cases at 1 and 1.5 mol.L^{-1} show similar heights.
It is complicated to interpret these results because additional data would be needed. Indeed, there may be a limiting initial concentration at which a variation in concentration no longer

has any influence on the crystals, their growth and their typical size. This would explain why the cases at 1 and 1.5 mol.L^{-1} are comparable. To conclude, experiments with intermediate concentrations as well as concentrations higher than 1.5 mol.L^{-1} are needed.

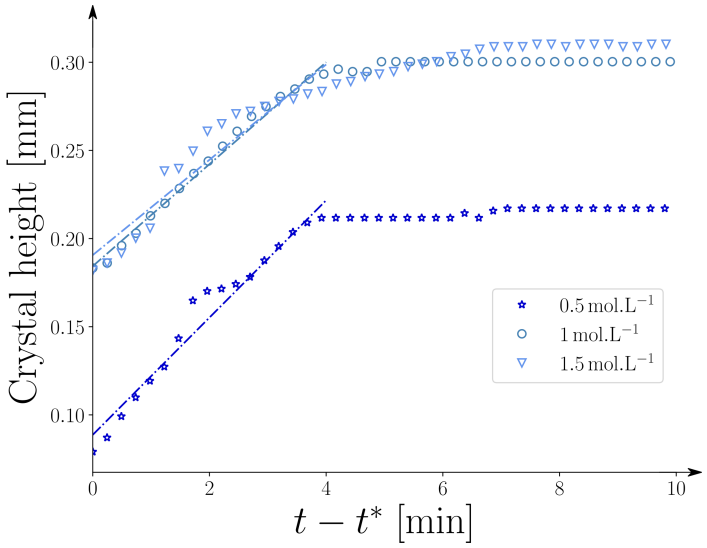

Fig. 5.18 – Crystal height as function of time ($t^* - t$) for different initial salt concentrations, where t^* is the time where the maximal crystal height exceeds the maximal droplet height. ($V_0 = 10\,\mu$L and $RH = 10\%$)

4.3 Arrangement of salt crystals in the final pattern

Influence of the relative humidity

From the study of the deposits as a function of initial concentration and relative humidity (Fig . 5.14), we note that humidity does not seem to have an impact on the morphology of the salt deposit when the initial salt concentration is less than $c_0 = 10^{-1}$ mol.L^{-1}. For higher concentrations, as the relative humidity increases, the pattern changes, especially the size and arrangement of the salt crystals. Thus, to study the influence of relative humidity, we use initial concentrations higher than $c_0 = 10^{-1}$ mol.L^{-1}.

For $RH = 10$ % and 30 % (Fig. 5.19a and 5.19b), the nucleation of the crystals appears exactly along the contact line and they immediately adhere to the substrate. The crystals then grow radially towards the center of the droplet, without moving. This enhances the pinning of the contact line by increasing the substrate wettability [118] and the contact line remains pinned until the very end of evaporation. At the end of evaporation, the crystals are uniformly distributed along the triple contact line. Whereas for a higher relative humidity $RH = 50$ % (Fig. 5.19c), the crystals are formed precisely at the contact line, but they do not adhere directly on the solid substrate and then are dragged towards the center of the droplet before attaching the substrate at some point and finally grow from there. The crystals growth probably leads to the depinning of the contact line as it modifies locally the internal flows and creates crystal driven flows [124]. Depinning is indeed observed in the top part of the deposit (Fig. 5.19c).
The differences between those two configurations could be explained by the influence of the relative humidity. Indeed, a higher relative humidity slows the evaporation process. This means that the flows inside the droplet are slower and that the solute concentration evolves

slowly along the interface. When the saturation condition is reached and the nucleation happens, the crystal grows very gradually, supplied by internal flows. It remains small enough to be carried by the flows inside the droplet for some time before adhering to the substrate. This can explain why the crystals move from the triple contact line towards the center of the deposit.

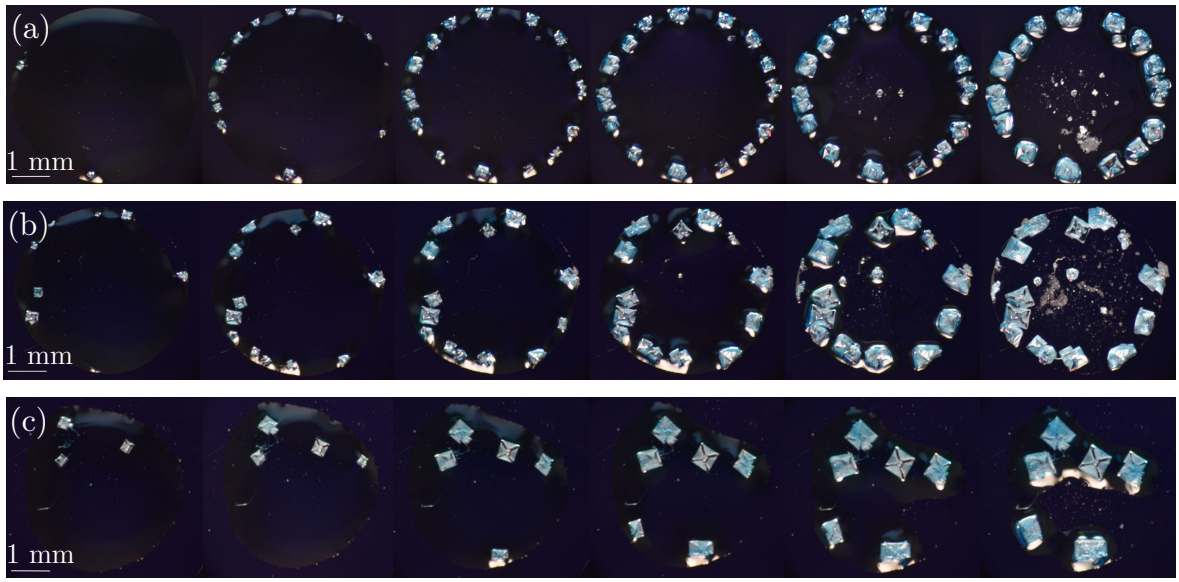

Fig. 5.19 – Top views of an evaporating saline droplet for different relative humidities. (a) $RH = 10\%$, (b) $RH = 30\%$ and (c) $RH = 50\%$. ($V_0 = 10\,\mu$L and $c_0 = 1\,\text{mol.L}^{-1}$)

If we focus on the number of salt crystals obtained for each humidity, some differences can be noticed (Fig. 5.21b). For $RH = 10$ %, the crystals are distributed along the triple contact line, all have roughly the same size and shape, except for some small crystals resting at the center. When the relative humidity is increased, for $RH = 30$ %, the crystals are still distributed along the initial contact line but the number of crystals decreases: we count 12 big individual crystals against 17 for $RH = 10$ %. The crystals seem less uniformly distributed along the triple contact line. Some crystals seem to have merged during the evaporation process. Finally, when the relative humidity is equal to 50 %, we get even fewer crystals, only 6 for this experiment. The number of crystals is given here as an indication: we perform each experiments 5 times, in order to confirm the observations, and we notice that for the same experiment, the number of final crystals vary around an average value. Finally, comparing the three different experiments, we conclude that the number of crystals has decreased as we increase the relative humidity. The crystals shape for a higher relative humidity appear more geometrical and cubic. NaCl has a natural crystal structure with a face centered cubic lattice. Increasing the relative humidity leads to longer evaporation times and thus slower evaporation dynamics inside the droplet: the crystal shape is affected by the evaporation rate [128]. In the case of colloidal stains, an ordered particle arrangement is due to a low deposition speed [129]: these results show that the same argument could be used for NaCl crystallization mechanism.

The arrangement of crystals at the contact line appears rather orderly. The distance between two consecutive crystals along the perimeter of the deposit appears to be constant for a given humidity. The distance between the centers of two neighboring crystals is measured and averaged over all crystals. This average distance is noted λ.

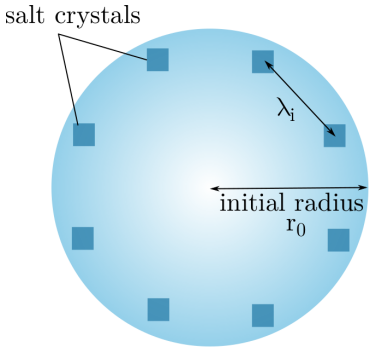

Fig. 5.20 – Measure of the distance between two salt crystals in the final salt pattern. The wavelength λ is the average distance between the crystals $\lambda = \frac{1}{n}\sum \lambda_i$, where n is the number of crystals.

The average distance between crystals is studied as a function of relative humidity (Fig. 5.21a). For a more correct comparison, λ is scaled by the initial radius of the droplet because it may have varied during the different experiments. The distance between the crystals increases with the humidity according to a proportional relation. This shows a particular influence of the relative humidity on the morphology of the salt deposit. This result should be put in perspective with the number of crystals obtained as a function of relative humidity (Fig. 5.21b). As the number of crystals decreases, it is consistent that the distance between crystals increases.
Since the amount of salt in the droplet is a finite quantity, there is a maximum amount of crystals that can be formed from such an initial concentration. Depending on the properties of the solute and the solvant and the rate of evaporation, a maximal theoretical crystal yield can be calculated [127]. This gives the mass of crystals formed but does not predict the number of crystal structures that we are trying to understand.

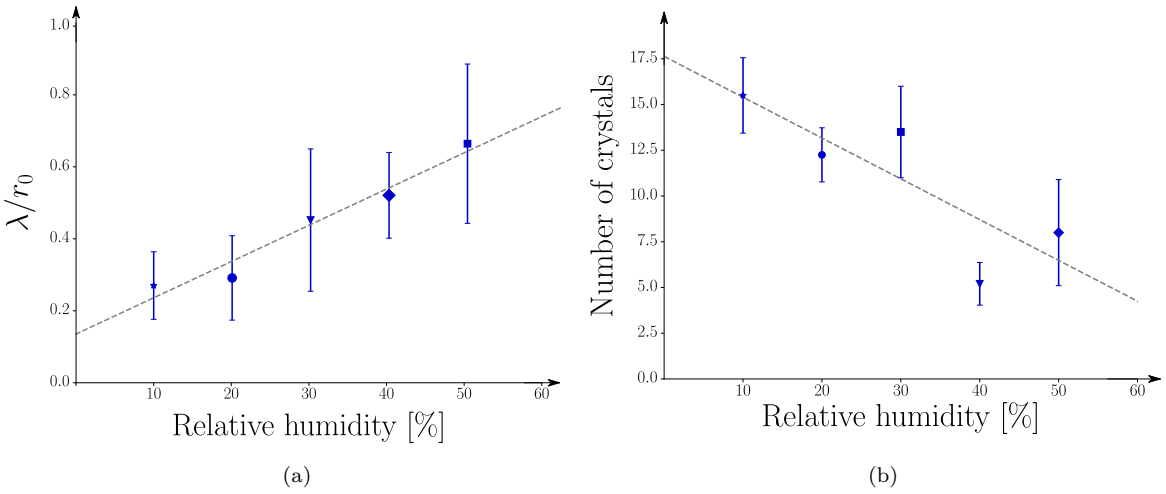

Fig. 5.21 – (a) Distance between salt crystals in the deposit at the end of evaporation as function of the relative humidity. (b) Number of salt crystals in the deposit at the end of evaporation as function of the relative humidity. ($V_0 = 10\,\mu$L and $c_0 = 1\,$mol.L^{-1})

Influence of the initial salt concentration

The number of crystals and the distance between crystals are measured on the deposits left by a saline droplet of higher initial concentration, $c_0 = 1.5\,\mathrm{mol.L^{-1}}$, for different relative humidities between 10 and 40%. Overall, over the range of humidities tested, the number of crystals obtained is lower as the initial concentration increases (Fig. 5.22b). In the same way as for an initial concentration of $1.5\,\mathrm{mol.L^{-1}}$, the number of crystals decreases with increasing humidity. As for the distance between crystals, it increases again with relative humidity (Fig. 5.22a). However, the distances between crystals are smaller when the initial salt concentration increases. A mechanism is proposed in the next paragraph to explain these results.

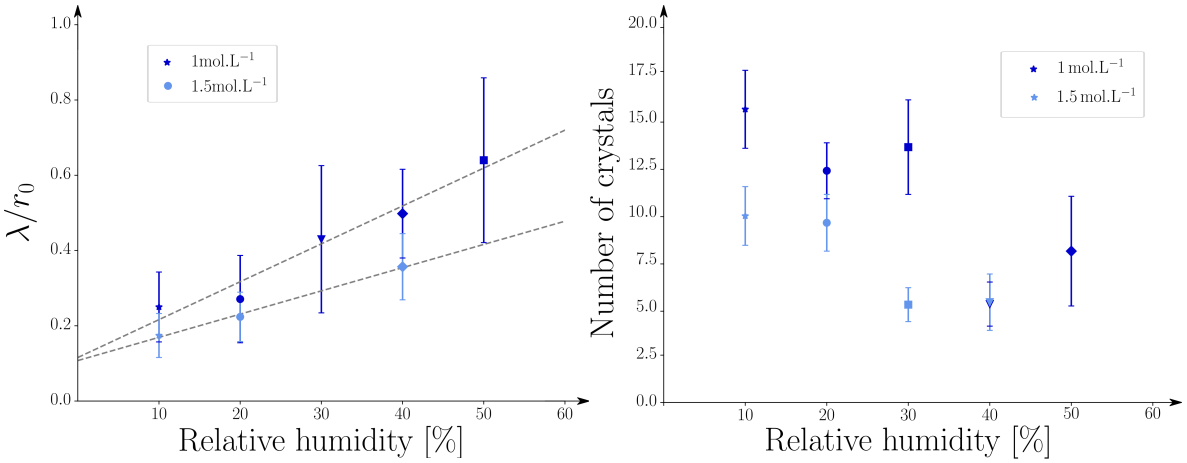

(a) (b)

Fig. 5.22 – (a) Distance between salt crystals in the deposit at the end of evaporation as function of the relative humidity, for two different initial salt concentrations. (b) Number of salt crystals in the deposit at the end of evaporation as function of the relative humidity, for two different initial salt concentrations. ($V_0 = 10\,\mu\mathrm{L}$)

Instability mechanism

The formation of salt deposits raises several questions: How is the position of each crystal determined? Why are there fewer crystals when humidity increases? Based on the hydrodynamics mechanisms that evolve with the initial salt concentration and the relative humidity and that create the various pattern morphologies (Fig. 5.9), we discuss a mechanism for the different structures of the final deposit, the arrangement and the number of the salt crystals.

The crystals arrangement in the salt pattern is particular. The structures are regularly positionned where was the triple contact line: the distance λ between the crystals in each pattern was measured. λ can be defined as a wavelength that is associated with an instability that determines the flow recirculation structures inside the droplet. λ is approximately $2\pi a r_0/n$, where r_0 is the droplet radius and n is the number of localized sediments. We measure the distance of the segment between the centers of the crystals and not the distance of the arc of the circle, which explains that a coefficient a is needed for this relationship to be verified with the values presented previously (Fig. 5.22). An instability could therefore be responsible for the different patterns observed and the arrangement of the crystals. In the case of the sessile droplet of salt solution evaporating into the air due to a moisture gradient, what tends to destabilize the system is the surface tension gradient that is due to the non-homogeneous

salt concentration in the droplet during evaporation. The effect of temperature, inertia or gravity are negligible. During evaporation, recirculation cells form due to the surface tension gradients between the top and the edge of the droplet. These cells are called Marangoni cells and form when a critical Marangoni number is exceeded. The driving force of the Marangoni instability is very often a temperature gradient but here the driving force is the salt concentration gradient. Based on the thermal Marangoni number, a solutal Marangoni number Ma_s is defined with an analogy between the effect of the temperature and the salt concentration on the surface tension [4, 130, 131]

$$Ma_s = \frac{\partial \gamma}{\partial c} \frac{\Delta c \, r_0}{\mu D} \tag{5.1}$$

where γ is the surface tension, c is the salt concentration, μ is the dynamic viscosity and D is the diffusion coefficient of the solute in the solvent According to several experiments in the literature, the critical solutal Marangoni number is around 10^2 [64, 130, 132]. When Ma_s exceeds this value then the Marangoni instability develops and forms the recirculation cells. We do not know exactly the values of all these parameters in our experiments but we can establish a scale. $\partial\gamma/\partial c$ is at most 5×10^{-3} from the relationship between surface tension and salt concentration (Fig. 1.4). The maximum salt concentration difference can be scaled as the saturation concentration value $c_s = 6.11\,\mathrm{mol.L^{-1}}$. The droplet radius in the experiments was $r_0 = 2.15 \times 10^{-3}$ m. The dynamic viscosity is of the order of 10^{-3} Pa.s and the diffusion coefficient D is of the order of $10^{-5}\,\mathrm{m^2.s^{-1}}$ [133]. This gives Marangoni numbers around 10^3 for the experiments which is above the critical Marangoni value. This means that Marangoni instabilities can develop in the system. For the initial salt concentrations considered in this study ($c_0 > 1\,\mathrm{mol.L^{-1}}$), we have a system that will reach the critical value for the solutal Marangoni number. This can be seen as an unstable state at initial time, as the salt concentration is fixed at the beginning of the experiment. If the initial salt concentration is reduced, then the surface tension gradient and the concentration gradient will be lower: the Marangoni number will not reach the critical value so no instability will be develop in the system. A Marangoni flow can appear without inducing any instability if the salt concentration is low. The number of crystals varies with the relative humidity. As the relative humidity increases, the number of crystals obtained in the salt deposit increases. The number of crystals is defined by the wavelength of the instability. The wavelength is controlled by the relative humidity, which is an initial perturbation of the system. As the system is unstable, the instability will develop along the evaporation. The value of the relative humidity influences the evaporation flux: if the humidity is low, the evaporation flux is strong which results in a strong initial perturbation. The value of the initial perturbation induces the instability mode that will appear. A high perturbation gives a high instability mode n with a small wavelength and thus a lot of Marangoni cells (Fig. 5.23).

This being said, there are still unanswered questions: when does crystallization occur? Is the position of the crystals determined by the instability and the flow or is it the other way around? If the crystallization occurs before the establishment of the flow, one can imagine that the position of the crystals forces the wavelength of the instability. Crystallization is difficult to observe since it takes place close to the substrate. Indeed, it is more favorable to nucleate close to the substrate than in the bulk of the solution [127]. For each relative humidity, we note the time from which the crystals are visible on the top pictures. This time is scaled to the final time, which depends on the relative humidity. We find that the appearance of the crystals is done at 65 $\pm$ 6% of the evporation time whatever the relative humidity. This result had already been observed experimentally for micrometer sized droplets [134]. The

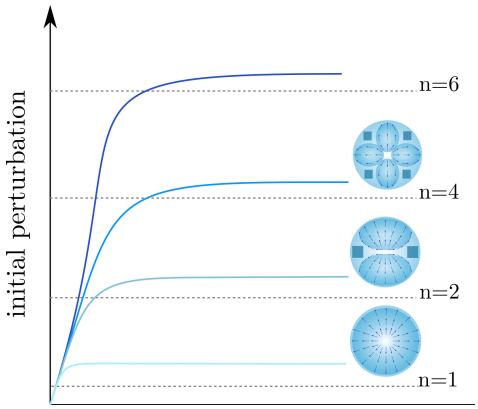

Fig. 5.23 – Initial perturbation of the system that selects the instability mode n. The perturbation is the relative humidity of the environment surrounding the sessile droplet.

crystallization thus takes place well after the establishment of the Marangoni recirculation cells. We can therefore hypothesize that the position of the salt crystals is determined by the Marangoni cells (Fig. 5.24). It remains to be determined whether the crystals form between the recirculating cells or in the center of the cells along the triple line. The points between the cells correspond to areas where the velocity is slower, so salt can accumulate and stagnate at these points, eventually forming the crystals. Within the cells, Marangoni flows bring salt to the edge of the droplet which is therefore a highly concentrated area where crystal formation is likely. To answer this question, additional experiments are needed since our current data do not support a particular mechanism.

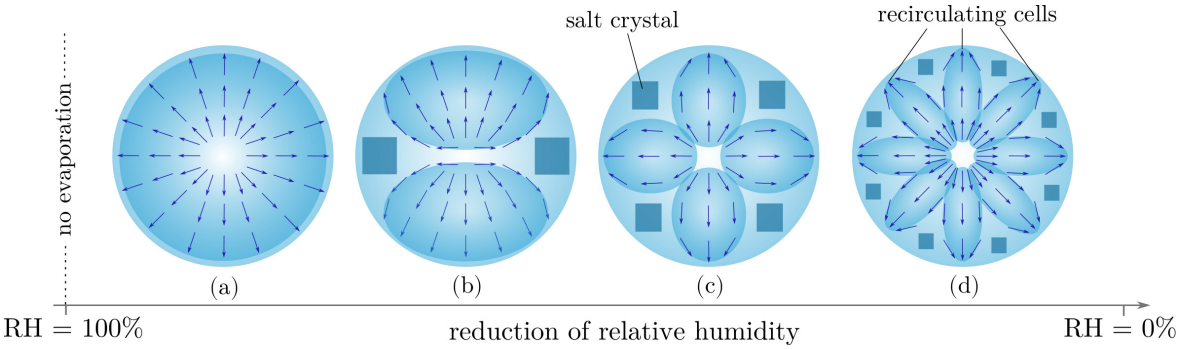

Fig. 5.24 – Instability modes that develop inside the droplet depending on the relative humidity. The number of cells decreases when the humidity increases. The recirculating cells determines the position of the salt crystals.

5 Evaporation cycles

In marine environments, sea spray carries droplets of salt water. These droplets will be deposited on the surrounding infrastructures and form sessile droplets. Depending on atmospheric conditions, such as temperature and relative humidity, the droplets will evaporate over time. The salt and non-volatile pollutants they contained will remain on the surface and form a salt deposit. Along the coast, the sea spray will repeatedly deposit droplets on the infrastructures. These infrastructures are therefore particularly exposed to sea spray and, depending on the materials they are made of, atmospheric corrosion phenomena can be observed and damage the materials. We suppose that the droplets tend to deposit at the level of a previous salt deposit. The succession of drop deposition constitute a cycle that repeats itself over time. In this part, we are interested in modeling and reproducing experimentally these cycles, contrary to the experiments carried out until now where we were only interested in a single droplet.

This study is still in progress since it is the subject of the research internship carried out by Vu Hai La and Ilyass Rhani, undergraduate students at Sorbonne University (2021/2022).

5.1 Evolution of the evaporation dynamics and the deposit pattern along a cycle

Experimental protocol

The cycles can be characterized by a repetition of a droplet deposit on the same substrate. We try to reproduce these cycles experimentally with the device used for the study of a saline droplet, which was presented at the beginning of this chapter (see 1.1). We consider **successive evaporation phases**. We are interested in the dynamics of the evaporation phase and the morphology of the salt deposits after each phase. We use the same experimental device as before, the pipette is simply fixed so that the deposition of the different droplets is always done at the same place (Fig. 5.25).

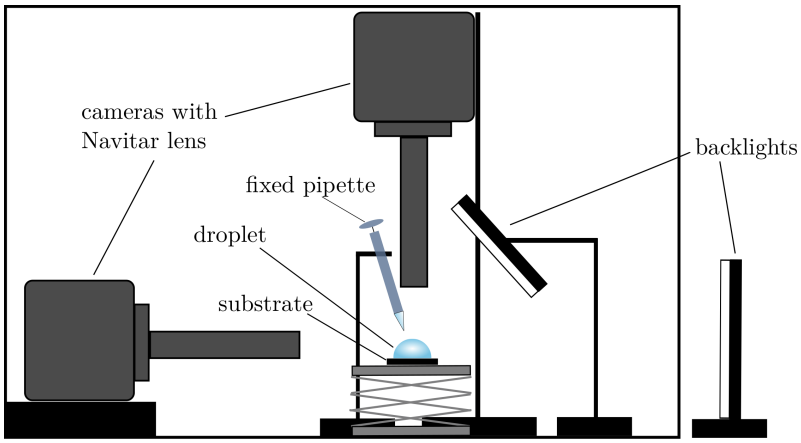

Fig. 5.25 – Schematic illustration of the experimental set-up for the study of the evaporation cycles with saline sessile droplets. The micropipette is fixed.

At the initial moment, we deposit a droplet of known volume $V_0 = 10\,\mu$L and concentration of sodium chloride c_0. The solutions are those prepared previously in the framework of the evaporations of a single salted droplet and the substrate also remains unchanged, i.e. silicon wafer (see 1.1). After complete evaporation of this first drop, a drop identical to the first one is

deposited at the exact location where the first drop was left. The micropipette is fixed on top of the substrate which allows to control precisely where the drops are deposited. This can be repeated as many times as desired. In this study, three droplets evaporate successively at the same location. The succession of identical droplets that are deposited and then evaporated is called a "cycle" (Fig. 5.26). Side and top photos are taken during each phase. This allows to measure the height, the angle and the radius of the droplet along each evaporation phase.

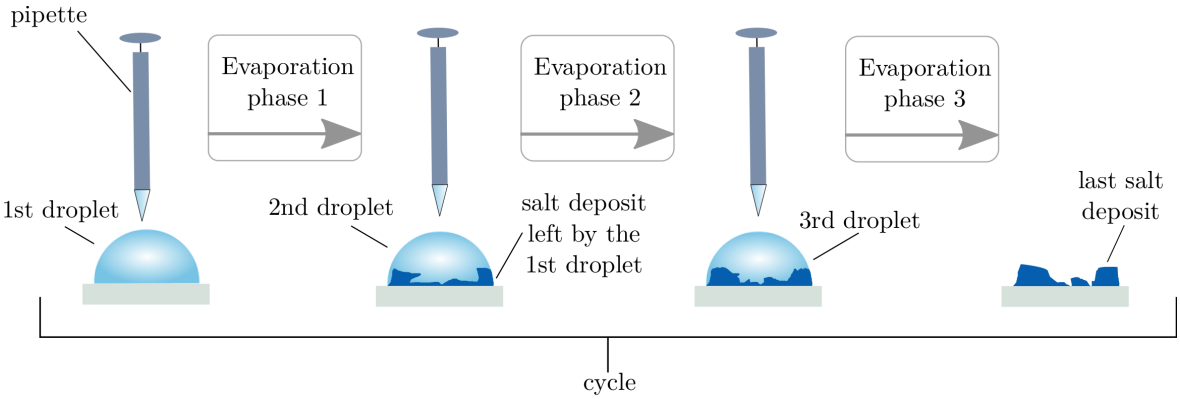

Fig. 5.26 – Schematic illustration of an evaporation cycle. The droplets are sequentially deposited at the exact same spot on the solid substrate.

First we are interested in a cycle where three droplets of initial volume $V_0 = 10\,\mu$L and initial concentration $c_0 = 1\,\text{mol.L}^{-1}$ are deposited sequentially. The relative humidity is 20% and the temperature is room temperature.
The first droplet is deposited on the substrate at the initial time. The shape is spherical (Fig. 5.27a-I). At the end of the first evaporation phase, a salt deposit is obtained (Fig. 5.29b-I). It presents large crystals, distributed on the perimeter of the droplet, forming a circular ring. The second droplet is deposited on this deposit. The presence of the deposit on the substrate modifies the surface condition and disturbs the contact between the droplet and the substrate. The droplet is deformed by the presence of the crystals and is no longer perfectly spherical (Fig. 5.27a-II). Air bubbles are also present inside the droplet just after deposition. The salt crystals may be hollow and thus trap air as they are coated. These bubbles then rise to the droplet surface during evaporation.
At the end of the second evaporation phase, the resulting salt deposit has been modified from the first deposit (Fig. 5.29b-II). The shape follows the shape of the second droplet so the deposit is not spherical, but rather oval. The crystals have grown and several crystals have gathered to form a single structure.
Finally, a third and last droplet is deposited on the second deposit. As the crystals are large, they will deform the droplet even more. This one is then not all spherical anymore (Fig. 5.27a-III). The presence of crystals at the place where the droplet is deposited forces the droplet to spread out even more. Indeed, the salt crystals occupy a certain volume, which leads the droplet to "overflow" outside the previous deposit. At the end of this third and last phase of evaporation, the crystalline structures obtained are quite different from what we could observe until now (Fig. 5.29b-III). There are crystals as in the previous deposits but there are also areas where the salt has deposited on the surface without forming cubic shaped crystals. In these areas, the deposit seems to consist of dendrites that propagate towards the outside of the deposit, which leads to a very asymmetric pattern. The crystal structures are even larger than in the previous deposit.

From the side view photos, the height of the three droplets is plotted over time (Fig. 5.28).

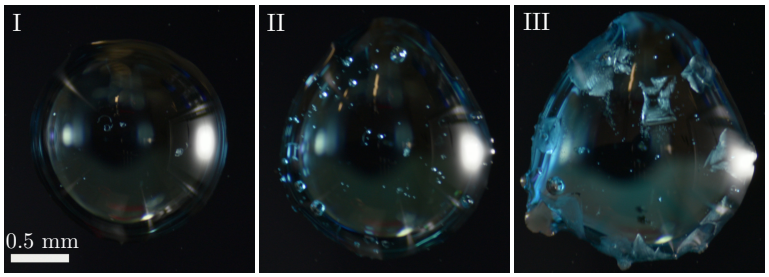

1st droplet 2nd droplet 3rd droplet

(a)

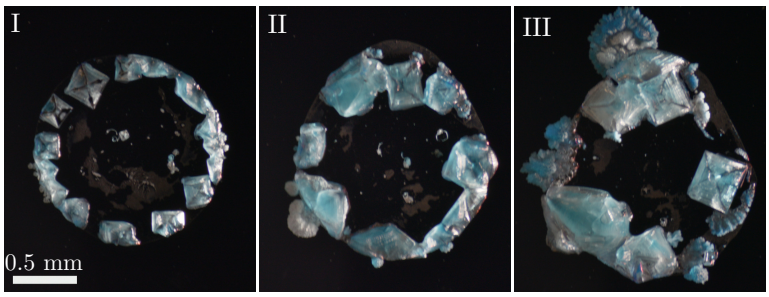

1st deposit 2nd deposit 3rd deposit

(b)

Fig. 5.27 – (a) Top views of the droplet just after the deposit at the beginning of each evaporation phase. (b) Top views of the salt deposits obtained at the end of each evaporation phase. ($V_0 = 10\,\mu$L and $RH = 20\%$)

The initial height varies slightly over the cycle, with the third droplet having a lower height. This may be related to the spreading of the droplet observed at the beginning of the third phase (Fig. 5.27a-III). The dynamics of the three droplets is identical, the height decreases linearly with time (Fig. 5.28a). To compare the evaporation rate of each droplet, the height is scaled by the initial height of each droplet (Fig. 5.28b). As the evaporation cycle progresses, the droplet evaporates more slowly.
As before, from a certain point, the maximum height of the droplet is exceeded by the height of the crystals that form. This is why we have no data for the height of the droplet below a certain height. For each droplet in the cycle, the moment when the crystals exceed the interface of the droplet is different. Indeed, the height of the crystals increases during the cycle, the crystalline structures are bigger and bigger, each new droplet constituting an additional salt contribution.
The minimum droplet heights measured are:

- 0.183 mm for the first droplet
- 0.290 mm for the second droplet
- 0.443 mm for the third droplet

The maximum heights recorded for the crystals at the end on each phase are:

- 0.300 mm for the first deposit
- 0.385 mm for the second deposit
- 0.534 mm for the third deposit

To summarize, during a cycle, the evaporation dynamics of each droplet follows a linear behavior. However, the evaporation rate is modified as the droplet takes more and more time to evaporate with each deposition. The deposited droplets are more and more deformed by the salt deposit left by the previous droplet. The pattern of the deposit evolves during the cycle and the crystalline structures are bigger and bigger and eventually spread out of the initial contact area between the droplet and the substrate.

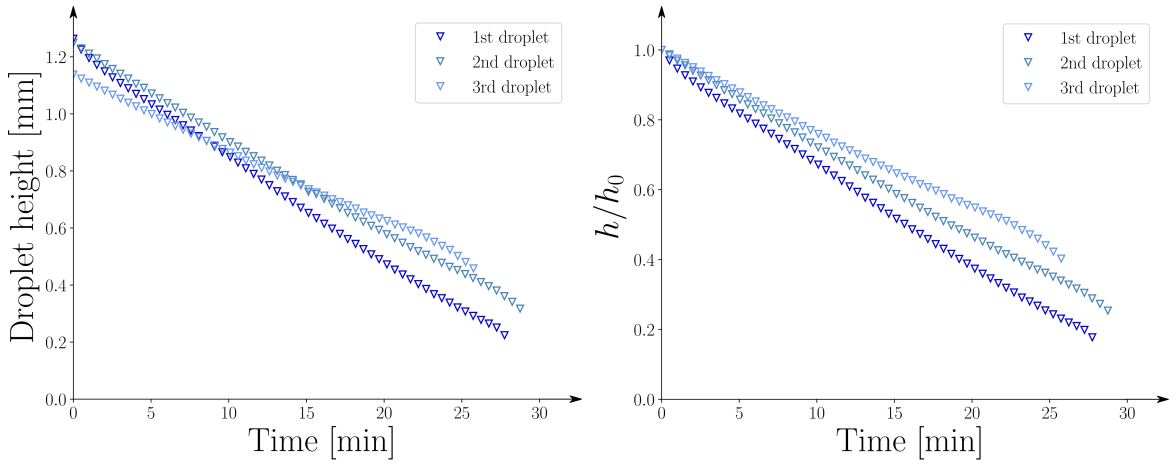

(a) (b)

Fig. 5.28 – (a) Height of each droplet along the evaporation cycle as function of time. (b) Height scaled by the initial height h_0 for each droplet along the evaporation cycle as function of time. ($V_0 = 10\,\mu$L and $RH = 20\%$)

5.2 Influence of the initial salt concentration

This last part present a parametric study where the initial salt concentration is varied from one cycle to another. However, the droplets within the same cycle all keep the same base concentration. Three different concentrations are tested: 0.5, 1 and 1.5 mol.L^{-1}. The salt deposits of the different cycles, obtained after each evaporation phase, are compared (Fig. 5.29c).

For the three concentrations, the deposition pattern evolves during the cycle. The higher the initial concentration, the greater the change in morphology.
For an initial concentration $c_0 = 0.5\,$mol.L^{-1}, the deposit keeps a circular shape during the cycle (Fig. 5.29a). However, the characteristic diameter of the deposit increases with the cycle. However, for higher initial concentrations, the shape of the deposit is less and less circular (Fig. 5.29b-II, Fig. 5.29b-III and Fig. 5.29c-III). The volume occupied by the crystals becomes large compared to the initial volume of the droplet and disturbs the shape adopted by the droplets which is normally only determined by a competition between surface tension and gravity.
In each of the first deposits, the salt crystals are distributed rather uniformly along the contact line as already observed previously in this concentration range (Fig. 5.29a-I, Fig. 5.29b-I and Fig. 5.29c-I).
As the initial concentration increases, the surface area of the substrate covered by the salt becomes larger. The crystals are larger and grow horizontally. The crystals also grow vertically but their maximum height is limited by the initial droplet height. Moreover, a different salt structure never observed until now in our experiments appears on the last deposits, in particular for the largest concentrations (Fig. 5.29b-III and Fig. 5.29c-III). These structures

appear at the very end of evaporation and propagate away from the initial contact surface between the droplet and the substrate. The fast propagation shows some dendritic patterns.

To conclude, during a cycle, we observe a modification of the basic pattern with the appearance of larger crystals and also of new dendritic structures. Even if the droplet is reformed on a previous salt deposit, the surface of the substrate covered by salt at the end of a cycle is more important than when considering a single droplet. This can eventually lead to a degradation of a larger surface of the material depending on its characteristics and its resistance to sodium chloride.

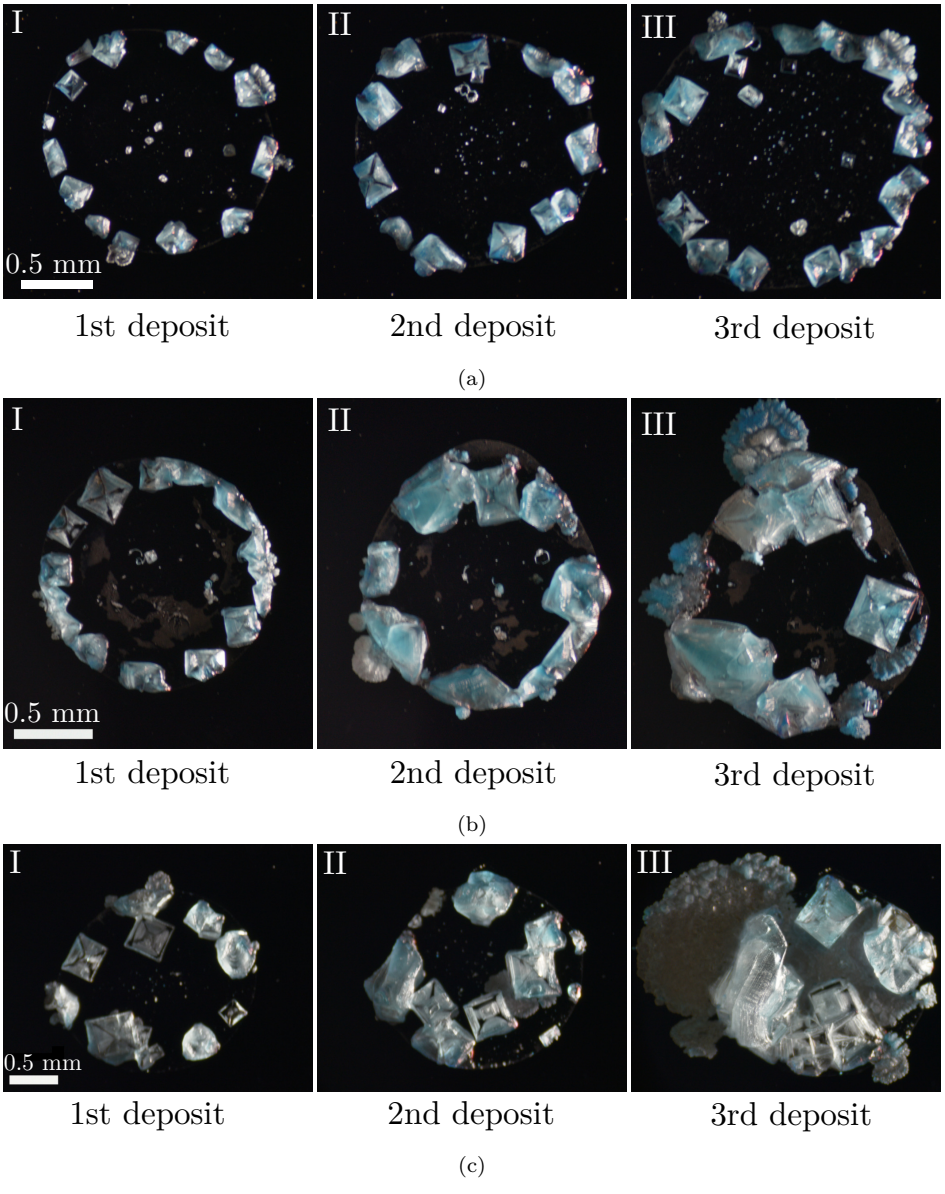

Fig. 5.29 – Top views of salt deposits obtained along evaporation cycles for three different initial salt concentrations ($V_0 = 10\,\mu$L and $RH = 20\%$). (a) $c_0 = 0.5\,\text{mol.L}^{-1}$, (b) $c_0 = 1\,\text{mol.L}^{-1}$ and (c) $c_0 = 1.5\,\text{mol.L}^{-1}$.

What to remember ?

The evaporation of salty droplets involves many physical phenomena, which makes its study both complex and interesting. The presence of salt affects the interfacial properties of the droplet, the hydrodynamics of the internal flows and also the evaporation dynamics. The higher the initial salt concentration, the slower the evaporation. The impact of salt on the equilibrium condition of the vapor concentration leads to a decrease of the vapor concentration gradient, which is the driving force of evaporation. The formation of salt crystals at the triple line can lead to a hindrance that would also limit the evaporation of the solvent.
The salt, here sodium chloride which is a non-volatile compound, leads to the formation of a deposit on the substrate after the complete evaporation of the solvent. This deposit presents different patterns which evolve according to the initial concentration and the relative humidity. The transition between the different morphologies observed (coffee-ring, uniform deposit, crystals pattern) can be related to salt concentration limits which lead to surface tension gradients. This will lead to Marangoni flows. Salt patterns are the result of hydrodynamics taking place inside the droplet during evaporation.
The influence of relative humidity is observed in a range of salt concentration where an effect of salt on surface tension is important. The evolution of the number of crystals, their arrangement and shape leads us to propose a scenario to explain the patterns. The hydrodynamic and crystallisation mechanisms combine and suggest an instability mechanism that defines the morphology as a function of humidity. Many questions remain open, however, and call for further observations.
The study of the evaporation cycles allows us to get closer to the repetitive droplet deposition by the sea spray for instance, although their modeling is still very simplified in these experiments. The successive deposition of salty droplets modifies the morphology of the saline deposit in the course of time. New structures appear and the symmetry of the pattern observed for a single droplet disappears. The increase of the initial salt concentration reinforces these modifications.

6 Towards numerical simulations of evaporating saline droplets

After having built and tested a numerical model allowing to simulate the evaporation of sessile droplets of pure liquid, we are interested in the saline droplets which constitute a binary mixture.
The presence of salt in the droplet makes the system more complex since salt is a non-volatile compound which will locally modify the properties of the solution. In the first section, the differences between the evaporation of a binary mixture and a pure liquid are presented. These differences must be taken into account in the numerical model and therefore new numerical implementations are needed. Some implementations have already been done in Basilisk, we will some of them. One of the major differences with the presence of salt is the consideration of Marangoni stresses due to surface tension gradients. As the method developed so far does not allow to study all contact angles, a new approach is proposed in the second section.
Finally in the last section, a test case illustrating the results of the method is presented, with a surface tension gradient along the interface.

Contents

1 Evaporation of binary mixtures

Salt solution droplets are considered as binary mixtures where an initial concentration of solute, salt, is dissolved in a solvent, water. The presence of salt modifies the properties of the solution and the evaporation dynamics compared to the case of the pure water droplet. This leads to several differences that will have to be taken into account in the numerical model to simulate the behavior of saline droplets during evaporation.

1.1 Differences with the evaporation of a pure liquid

Non-volatile solute

The salt dissolved in the droplet, sodium chloride in this study, is a non-volatile compound. It will not evaporate unlike the water in the solvent and will therefore remain in the droplet. The amount of salt is fixed at the beginning of evaporation and will not change over time, it remains constant. This initial quantity determines the initial salt concentration c_0 in relation to the initial volume of the droplet.

Salt concentration

At the initial time, the concentration of salt is uniform in the droplet and has a known initial concentration c_0. However, during evaporation the volume of the droplet will decrease since the solvent is volatile. Since the amount of salt remains constant, the concentration of salt c increases during the evaporation process. The concentration is therefore a time-dependent quantity.

Heterogenous salt concentration

If the sessile droplet forms a contact angle θ between 0 and 90°, then the evaporation flux is non-homogeneous along the droplet interface. The evaporation flux will be greater at the triple line than at the top of the droplet. To compensate for this higher flow at the edge of the droplet, a capillary flow is set up from the center of the droplet to the periphery. This flow will then transport the salt present in the solution (represented with red dots) towards the triple line. This results in the creation of heterogeneous concentration zones within the droplet: the edge will be highly concentrated in salt while the center and the top of the droplet will be low concentrated in salt (Fig. 6.1). These zones are set up during evaporation and are dependent on the flows present in the droplet, which are responsible for mixing the solution. The concentration is therefore a quantity that evolves in time and space. There are therefore concentration gradients within the droplet that develop during evaporation.

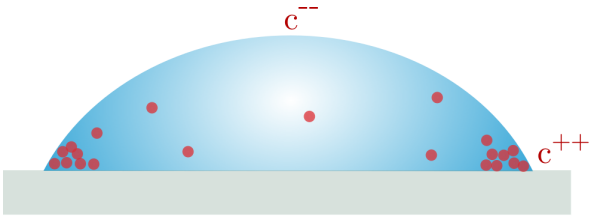

Fig. 6.1 – Heterogenous salt concentration inside the droplet along the evaporation. The salt concentration is higher at the triple contact line c^{++} than at the apex of the droplet c^{--}.

Impact on the evaporation dynamics

The salt concentration influences the evaporation dynamics. Indeed, the higher the salt concentration, the lower the evaporation rate. This is due to two effects:

- the presence of a solute changes the composition of the liquid. According to Raoult's law [115], the saturation concentration varies linearly with the fraction of solvent in the liquid. The more solute is added, the more the solution is concentrated, the more the solvent fraction decreases and therefore the saturation concentration decreases (Fig. 5.8). This leads to lower concentration gradients which slows down the evaporation since these gradients are the driving force of the phase change process.
- The accumulation of salt at the contact line can create a barrier and therefore to a slowing down of the evaporation since the evaporation flow is locally strong there. Moreover, if salt crystals form then they constitute solid structures which can have an effect on the evaporation of the solvent at the droplet edge.

Impact on the surface tension

The presence of salt in the solution locally modifies the surface tension γ (Eq. 1.2). Indeed, the salt acts as a surfactant and disturbs the value of the surface tension. The surface tension increases with the salt concentration (Fig. 1.4). However, the salt concentration is not necessarily homogeneous within the droplet. This will lead to local variations of the surface tension. At the edge of the droplet, the concentration is generally high which induces a higher surface tension than at the top of the droplet, where the concentration is lower. Salt concentration gradients give surface tension gradients. These surface tension gradients drive the Marangoni flow (Fig. 6.2). This additional flow inside the droplet will also participate in the mixing of the surface and the distribution of the salt concentration. Indeed, it is a flow directed from the low concentration areas to the high concentration areas: it will therefore be self-sustaining by transporting salt towards the triple line and will reinforce the heterogeneity of the concentration field within the droplet. The salt concentration influences the evaporation dynamics. Indeed, the higher the salt concentration, the lower the evaporation rate.

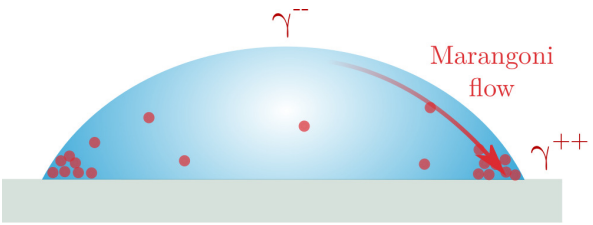

Fig. 6.2 – Heterogenuous salt concentration that leads to surface tension gradients. The surface tension is higher at the triple contact line γ^{++} than at the apex of the droplet γ^{--}.

Salt deposit

At the end of the evaporation, when all the solvent has evaporated, only the salt remains on the substrate. Depending on the evaporation conditions and the initial salt concentration, different patterns will form (Fig. 5.14). At the beginning of the evaporation, the salt is dissolved in the solution. However, as the evaporation proceeds, the salt concentration increases. If it reaches a critical value of supersaturation, then the phenomenon of crystallization can take place. The formation of nuclei is then possible and will eventually grow and give salt crystals.

1.2 Numerical implementations to add to the pure liquid model

All the differences found with the case of evaporation of a pure liquid must be taken into account in the model of evaporation of a mixture. The numerical model developed under Basilisk used until now must therefore be modified. The most important part concerns the

calculation of the surface tension and the Marangoni constraints. Several numerical implementations have already been carried out by Magdelaine who was interested in the simulation of the Marangoni instability in a film [34]. We will briefly describe the principle of the main implementations and in particular the method of calculating the Marangoni stresses. The latter has limitations and we propose in the following a new method.

Conservation of the solute in the liquid phase

One of the important requirements for the evaporation of a salt solution is the non-volatile nature of the salt. It is important to guarantee the conservation of the solute in the liquid phase throughout the evaporation process. The interface then behaves as a wall impermeable to the passage of salt. The interface is in motion due to evaporation and collects solute in its path. The zones close to the interface are concentrated in solute since the solvent evaporates there. From a numerical point of view, there are two steps:

- in a first step, the solute diffuses inside the droplet. The interface is considered as immobile and impermeable so that the solute diffuses only in the liquid phase (Fig. 6.3). This is done by cancelling the diffusion coefficient of the solute on the interface.
- in a second step, we consider the advection of the solute. When evaporation takes place, some cells will become dry, all the solvent evaporates and only the solute remains in these cells. In this case, the solute must be advected and distributed in the cells near the interface (Fig. 6.3). The interface is mobile but the movement of the interface does not correspond to a flow that transports the solute. If the solute is advected with the velocity of the interface then it is not necessarily the cells near the interface that will concentrate, which is not physical. Magdelaine illustrates this phenomenon by making the analogy with a net that collects salt on its way [34].

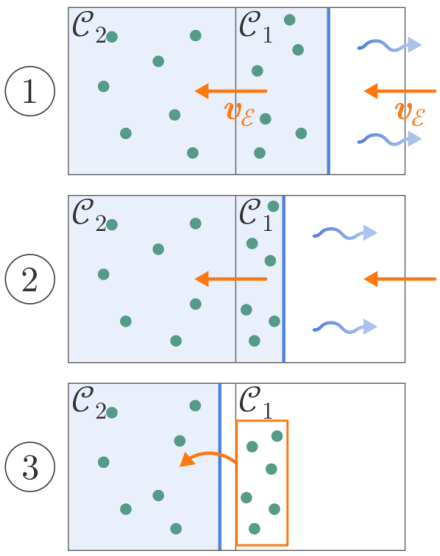

Fig. 6.3 – Analogy with a net. (1) The solvent evaporates, with induces an interface velocity v_e, this velocity is not used to advect the solute as it is not a flow velocity. (2) The interface retreats and as the solute is not advected yet, it accumulates in the cells near the interface. The cells near the interface are the most concentrated. (3) Finally, if the cell becomes totally dry, the solute has to be advected and distributed to the neighbouring cells as it has to stay inside the solution. (Figure reproduced from [34])

Marangoni stresses

In Chapter 2, the following expression for the resultant force of the surface tension $\mathbf{f}_\gamma$ was introduced

$$\mathbf{f}_\gamma \delta_I = \gamma \kappa \mathbf{n} \delta_I + \overline{\nabla}_S \gamma \delta_I \tag{6.1}$$

where δ_I is a dirac distribution at the interface, κ is the interface curvature, $\mathbf{n}$ is normal at the interface and ∇_S, the surface gradient.
The first term translates the curvature of the interface and is called the **Laplace pressure** [26]. The second term is a tangential stress at the interface induced by a composition or temperature gradient which is called the **Marangoni contribution** [80]. The normal resultant of the surface tension, i.e. the Laplace pressure, is already implemented in Basilisk. However, the tangential resultant, i.e. the Marangoni stress, is not taken into account. In the case of evaporation of droplets of saline solution, surface tension gradients will appear. The implementation of the Marangoni resultant must therefore be performed.

There are already codes including Marangoni constraints. They have been implemented in Gerris, the predecessor of Basilisk, by Seric et al [135]. The implementation is applicable to both temperature and concentration dependent surface tension coefficient. The implementation of most of the existing codes is based on the continuous surface tension formulation. Magdelaine proposed a method based on the integral formulation to take into account the Marangoni constraints in Basilisk [34]. Indeed, as the interface is defined indirectly in Basilisk (through the VOF method), the calculation of the surface gradient necessary for the continuous formulation was complicated. This integral method allows to reproduce the Marangoni instability in a satisfactory way. However, there are several limitations that make it necessary to try another approach, in particular the limitation with respect to the contact angle. When the contact angle exceeds 45°, the method is no longer relevant because only the vertical height function of Basilisk is used. In the case of the sessile droplet, the contact angles considered can go up to 90°. We therefore propose a new method to treat a wider range of contact angles.

2 Numerical method for the Marangoni stresses

We adopt a continuous approach in 2D that can be extended easily to 3D. The continuous approach requires to calculate the surface gradient of the surface tension force and to have the tangential vector in each point of the interface.
In Basilisk, there are two methods for determining the position of the interface: the VOF method and the method with height functions. The height functions, both vertical and horizontal, calculate the distance to the interface by integrating the volume fraction f in the liquid, or $1-f$ in the air. This description of the interface allows a better accuracy, especially for calculating the curvature [73, 78]. We therefore use the height functions to calculate the normal and the tangent to the interface. This calculation is done in a more precise way than if we used the normal and the tangent from the VOF method.
In a work cell containing the interface, we need to determine the local normal and tangent vectors to this piece of interface. Finding the tangent is equivalent to defining the slope of the interface which is noted m. To do this, we use the height functions in the left and right cells and interpolate to order two the interface in the middle cell of interest (Fig. 6.4).

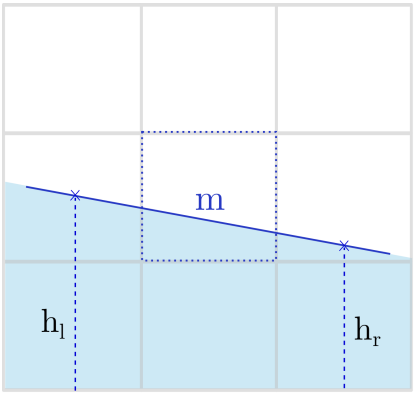

Fig. 6.4 – Calculation of the droplet interface slope m with the vertical height functions. We use the height functions in the left and right cells h_l and h_r regarding the cell of interest to compute the interface slope at order two.

In each cell, a local reference frame centered with respect to the cell is defined (Fig. 6.5). The tangential vector is to be defined in this local frame as

$$y = mx + y_0 \tag{6.2}$$

where y_0 is the distance between the interface and the center of the cell. From here, the normal vector is deduced.
The points where the interface crosses the sides of the cell are denoted (x_l, y_l) and (x_r, y_r) and identified in the reference frame. The distance between these two points δ can then be calculated precisely and the value of the surface tension in these points can also be calculated. Finally, the surface tension gradient is deduced

$$\frac{\partial \gamma}{\partial S} = \frac{\Delta \gamma}{\delta} = \frac{\gamma(x_r, y_r) - \gamma(x_l, y_l)}{\delta} \tag{6.3}$$

where S is the interface surface where the surface tension gradient is evaluated.
Knowing the exact coordinates of the points (x_l, y_l) and (x_r, y_r) allows to calculate the exact distance δ where the surface tension gradient has to be evaluated. Previous methods used

the mesh size to approximate δ which induces uncertainty in the evaluation of the surface gradient.
Surface tension is a source term in the right-hand-side of the evolution equation for the velocity of the centered Navier–Stokes solver i.e. it is an acceleration. Finally, for each interface for which γ is non-zero, we compute the surface tension acceleration using the height functions. This way the surface tension can vary along the interface as function of the local salt concentration. This method is tested in the next section to see if the surface tension gradient is computed correctly to result in a Marangoni flow.

Fig. 6.5 – Local reference frame centered in an interfacial cell. The slope of the interface m was calculated with the height functions and can be used to deduce the tangent vector in the local reference frame. The center of the cell is at a distance y_0 of the interface. The points (x_l, y_l) and (x_r, y_r) are identified and will be used to evaluate the surface tension gradient.

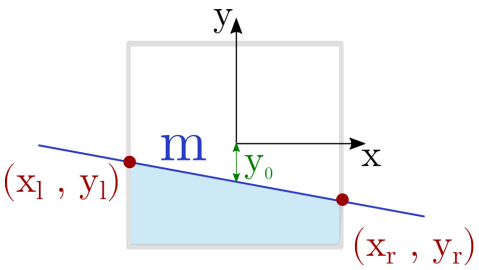

For each case, the vertical functions are used in the first attempt to localize the interface. When the vertical functions do not allow to find the interface (i.e. when the contact angle becomes too large) we switch to the horizontal functions (Fig. 6.6). The slope is calculated and inverted to obtain a formulation equivalent to that obtained with the vertical functions.

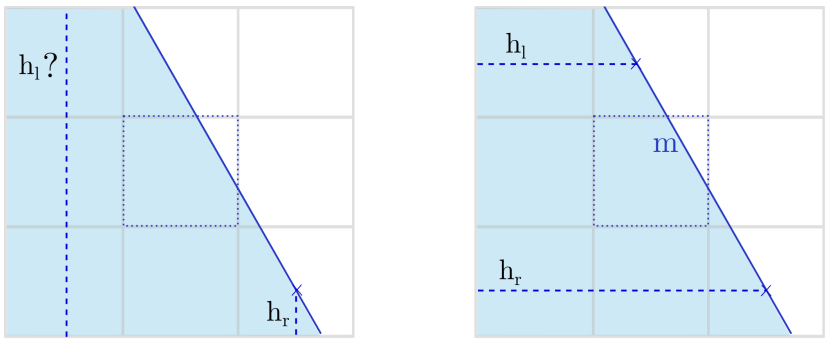

Fig. 6.6 – Use of the height functions to localize the interface. (a) For large contact angles, the vertical height functions are not able to determine the position of the interface. (b) If the vertical height functions do not give any result, we switch to the horizontal height functions to recover the position of the interface.

To confirm that this approach is accurate and efficient, we compare the normals computed using the height function method and the VOF method with the theoretically computed normals (Fig. 6.7). The normals are computed at the center of each cell containing the interface, which explains why they are not located exactly on the interface. We can notice that the normals from the height functions are much closer to the theoretical normals than the normals from VOF. Moreover, we have to specify that the resolution chosen for this test case was coarse, there are few meshes to describe the interface. However, we note that the height function method does not seem to be affected and still allows to obtain reliable results.

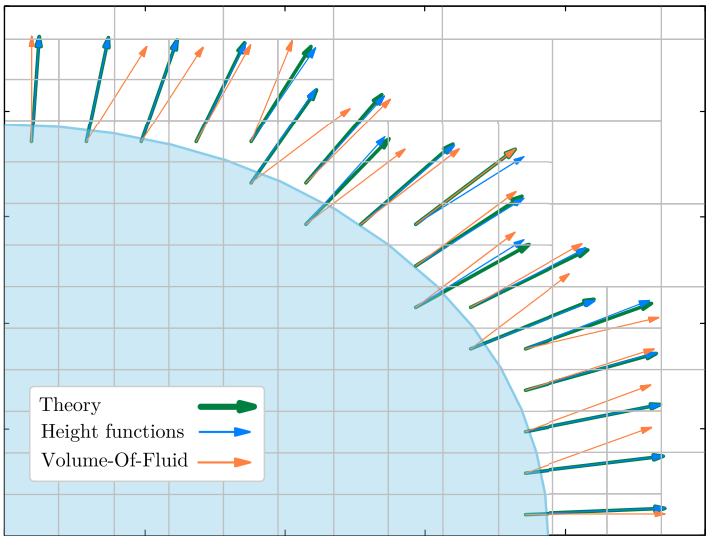

Fig. 6.7 – Comparison of the normals at the droplet interface calculated with different numerical approaches. The normals from the height functions appears closer to the theoretical ones compared to the normals obtained with the Volume-Of-Fluid (VOF) method. The interface normals are first calculated at the center of the cells containing the interface therefore they does not appear exactly on the interface.

3 Results

To test the numerical implementation described previously for the Marangoni stresses, a test simulation is performed. Evaporation is not taken into account to simplify the dynamics, the droplet is at equilibrium on a substrate. The surface tension is artificially modified along the droplet interface. For simplicity, we consider that the surface tension gradient is constant along the interface. No solute concentration is considered in this test case, the aim is to verify the numerical implementation of the Marangoni stresses and to see if a Marangoni flow is induced.

As shown on Fig. 6.8, a flow appears along the interface of the droplet, going from the top to the edge of the droplet. This is a Marangoni flow driven by the surface tension gradient imposed at the interface. The surface tension gradient is the only flow driver present in the system as evaporation is not taken into account. The Marangoni flow creates a recirculation cell inside the droplet. The numerical implementation proposed for the Marangoni stresses is thus efficient and induces the expected hydrodynamics.

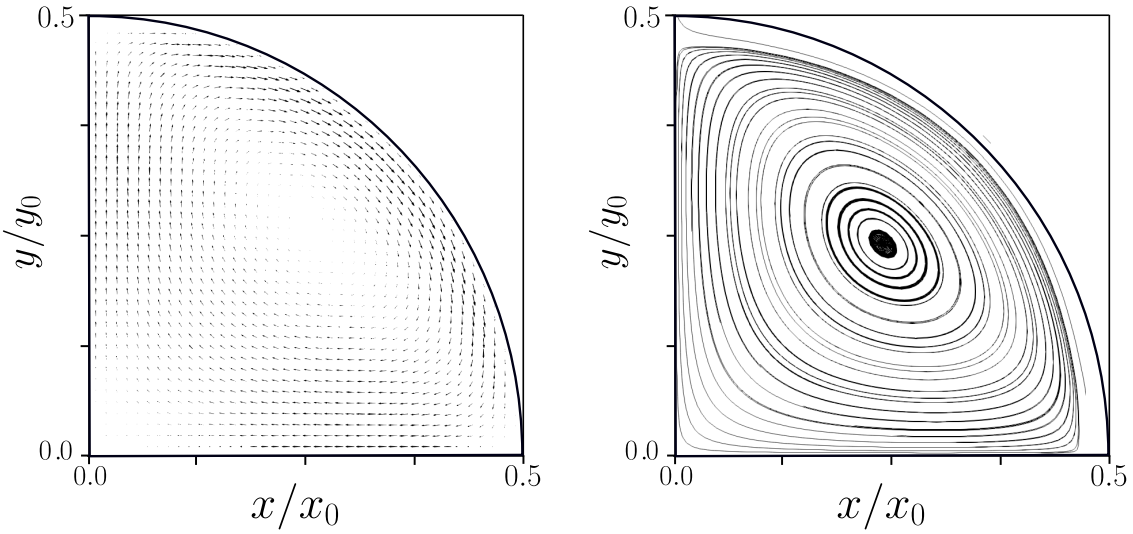

Fig. 6.8 – Marangoni flow induced by the surface tension gradient along the interface. (a) Velocity vector field where the vector length sizes for the velocity norm. (b) Velocity streamlines inside the sessile droplet.

This only consists in a test case for the computation of the Marangoni stresses. As explained before, the surface tension gradient is due to the heterogenous salt concentration along the droplet interface. This is not taken into account in this first simulation. In order to reproduce the dynamics inside an evaporating saline droplet, the Marangoni contribution has to be coupled with the evaporation solver and the relation between surface tension and salt concentration has to be implemented.

What to remember ?

Salt solution droplets are more complex systems than pure liquids since the different compounds do not behave in the same way during evaporation. A major difference is the non-volatility of the salt, which will therefore remain in the droplet during evaporation and become concentrated as the solvent evaporates. The salt concentration within the droplet evolves over time and becomes more and more heterogeneous due to hydrodynamics. This leads to stress gradients that must be taken into account in the numerical model since they are responsible for the Marangoni flows. A method for the calculation of Marangoni stresses based on height functions is presented in this chapter. This method allows an accurate calculation of the normal and tangent vectors at any point of the interface and a reliable estimation of the surface tension gradient. The results of the first test cases performed without evaporation show that the Marangoni flow is well reproduced. This numerical implementation opens many perspectives, such as coupling with evaporation and moving to 3D to numerically simulate the evaporation experiments of saline sessile droplets presented in Chapter 5.

Conclusion

Summary of the work

In this work, the evaporation dynamics of sessile droplets is investigated, for droplets composed of pure water and a mixture of water and salt. This subject is of particular interest in different scientific communities and for many industrial applications. We have worked both numerically and experimentally.

A numerical model is built with the Basilisk software, which is an efficient numerical tool adapted for the simulation of two-phase flows. Three major implementations have been done

- First of all, the mass jump at the interface during the phase change has been taken into account in order to describe the dynamics of the system as accurately as possible. This induces a velocity jump at the interface which results in a convective motion in the gas and an additional pressure in the liquid. The method we propose is based on the numerical tools available in Basilisk, in particular the volume fraction.
- The modeling of a contact line pinned during the whole evaporation process has allowed to reproduce the pinned evaporation mode that can be adopted by a sessile droplet. The use of height functions allowed to impose a defined contact angle. This anchoring condition proved to be efficient and gave results consistent with the experiments.
- Finally, the calculation of Marangoni stresses was done to simulate cases where the surface tension varies along the interface. The height functions were used to improve the calculation of the normal and tangent vectors at the interface compared to other previously established methods. In particular, this work allowed the reproduction of the Marangoni flow induced by a surface tension gradient.

In addition to the numerical work, an experimental study was conducted on the evaporation of sessile droplets. Several experimental set-ups have been set up and data processing methods have been built in order to treat different configurations, depending on the experimental conditions chosen.

- The analysis of the evaporation dynamics of pure water droplets according to the pinned mode allowed to have experimental data to validate the numerical model and in particular with the implementation of the anchoring condition of the triple line.
- The analysis of the salt deposits and the study of the different morphologies obtained as a function of the control parameters (initial salt concentration and relative humidity) revealed particular patterns. The observation of the arrangement of sodium chloride crystals in a micro metric sessile droplet under the effect of relative humidity reveals a complex and unstable hydrodynamic mechanism.
- The opening towards the study of evaporation cycles shows the evolution of the morphology of the deposits towards varied structures still complicated to characterize.

Future work

The work proposed here opens many perspectives, of continuation and improvement. All the building blocks of a numerical model allowing the study of the evaporation dynamics of a saline droplet are in place and can now be coupled to reproduce the complete hydrodynamics of the system. The numerical implementations developed, in particular on the Marangoni constraints, have the advantage of facilitating the transition to 3D simulations. This would allow to reproduce the experimentally tested cases and to highlight the flows that lead to a particular distribution of the salt concentration. The treatment of salt supersaturated zones requires the implementation of a special numerical condition in order to reproduce the crystallization phenomena and the formation of salt crystals that appear during evaporation. By adding the reaction equations between the substrate and the salt solution, we could move towards a complete model of evaporation and corrosion under droplet allowing in particular to characterize the phenomena of atmospheric corrosion.

Bibliography

[1] D. Brutin, B. Sobac, B. Loquet, and J. Sampol, "Pattern formation in drying drops of blood," *Journal of fluid mechanics*, vol. 667, pp. 85–95, 2011.

[2] L. Bahmani, M. Neysari, and M. Maleki, "The study of drying and pattern formation of whole human blood drops and the effect of thalassaemia and neonatal jaundice on the patterns," *Colloids and Surfaces A: Physicochemical and Engineering Aspects*, vol. 513, pp. 66–75, 2017.

[3] A. Frohn and N. Roth, *Dynamics of droplets*. Springer Science & Business Media, 2000.

[4] D. Zang, S. Tarafdar, Y. Y. Tarasevich, M. D. Choudhury, and T. Dutta, "Evaporation of a droplet: From physics to applications," *Physics Reports*, vol. 804, pp. 1–56, 2019.

[5] M. Kuang, L. Wang, and Y. Song, "Controllable printing droplets for high-resolution patterns," *Advanced materials*, vol. 26, no. 40, pp. 6950–6958, 2014.

[6] J. Park and J. Moon, "Control of colloidal particle deposit patterns within picoliter droplets ejected by ink-jet printing," *Langmuir*, vol. 22, no. 8, pp. 3506–3513, 2006.

[7] H. Kim, F. Boulogne, E. Um, I. Jacobi, E. Button, and H. A. Stone, "Controlled uniform coating from the interplay of marangoni flows and surface-adsorbed macromolecules," *Physical review letters*, vol. 116, no. 12, p. 124501, 2016.

[8] P. Rengasamy and K. Olsson, "Sodicity and soil structure," *Soil Research*, vol. 29, no. 6, pp. 935–952, 1991.

[9] V. N. Wong, R. C. Dalal, and R. S. Greene, "Salinity and sodicity effects on respiration and microbial biomass of soil," *Biology and fertility of soils*, vol. 44, no. 7, pp. 943–953, 2008.

[10] R. Cooke and I. Smalley, "Salt weathering in deserts," *Nature*, vol. 220, no. 5173, pp. 1226–1227, 1968.

[11] H. M. Gorr, J. M. Zueger, D. R. McAdams, and J. A. Barnard, "Salt-induced pattern formation in evaporating droplets of lysozyme solutions," *Colloids and Surfaces B: Biointerfaces*, vol. 103, pp. 59–66, 2013.

[12] A. Bender, P. Stephan, and T. Gambaryan-Roisman, "A fully coupled numerical model for deposit formation from evaporating urea-water drops," *International Journal of Heat and Mass Transfer*, vol. 159, p. 120069, 2020.

[13] A. Marin, S. G. Huisman, and M. Mikkers, "The morphology of parched tears," in *APS Division of Fluid Dynamics Meeting Abstracts*, pp. H30–004, 2019.

[14] B. Zheng, L. S. Roach, and R. F. Ismagilov, "Screening of protein crystallization conditions on a microfluidic chip using nanoliter-size droplets," *Journal of the American chemical society*, vol. 125, no. 37, pp. 11170–11171, 2003.

[15] J. Li, R. Wu, Z. Jing, L. Yan, F. Zha, and Z. Lei, "One-step spray-coating process for the fabrication of colorful superhydrophobic coatings with excellent corrosion resistance," *Langmuir*, vol. 31, no. 39, pp. 10702–10707, 2015.

[16] V. Soulié, S. Karpitschka, F. Lequien, P. Prené, T. Zemb, H. Moehwald, and H. Riegler, "The evaporation behavior of sessile droplets from aqueous saline solutions," *Physical Chemistry Chemical Physics*, vol. 17, no. 34, pp. 22296–22303, 2015.

[17] F. Lequien, V. Soulié, G. Moine, A. Lequien, D. Feron, P. Prene, H. Moehwald, H. Riegler, and T. Zemb, "Corrosion influence on the evaporation of sessile droplet," *Colloids and Surfaces A: Physicochemical and Engineering Aspects*, vol. 546, pp. 59–66, 2018.

[18] J. Li, B. Maier, and G. Frankel, "Corrosion of an Al-Mg-Si alloy under MgCl2 solution droplets," *Corrosion Science*, vol. 53, no. 6, pp. 2142–2151, 2011.

[19] S. Morton and G. Frankel, "Atmospheric pitting corrosion of AA7075-T6 under evaporating droplets with and without inhibitors," *Materials and Corrosion*, vol. 65, no. 4, pp. 351–361, 2014.

[20] S. Misyura, "The dependence of drop evaporation rate and wettability on corrosion kinetics," *Colloids and Surfaces A: Physicochemical and Engineering Aspects*, vol. 610, p. 125735, 2021.

[21] B. G. Koushik, N. Van den Steen, M. H. Mamme, Y. Van Ingelgem, and H. Terryn, "Review on modelling of corrosion under droplet electrolyte for predicting atmospheric corrosion rate," *Journal of Materials Science & Technology*, vol. 62, pp. 254–267, 2021.

[22] C. Hansson, "The impact of corrosion on society," *Metallurgical and Materials Transactions A*, vol. 42, no. 10, pp. 2952–2962, 2011.

[23] J. Dong, E. Han, and W. Ke, "Introduction to atmospheric corrosion research in china," *Science and Technology of Advanced Materials*, vol. 8, no. 7-8, pp. 559–565, 2007.

[24] N. Van den Steen, H. Simillion, O. Dolgikh, H. Terryn, and J. Deconinck, "An integrated modeling approach for atmospheric corrosion in presence of a varying electrolyte film," *Electrochimica Acta*, vol. 187, pp. 714–723, 2016.

[25] M. Baklouti, N. Midoux, F. Mazaudier, and D. Féron, "Estimation of the atmospheric corrosion on metal containers in industrial waste disposal," *Journal of hazardous materials*, vol. 85, no. 3, pp. 273–290, 2001.

[26] P.-G. De Gennes and F. Brochard-Wyart, *Gouttes, bulles, perles et ondes*. Belin Éducation, 2015.

[27] J. A. F. Plateau, *Statique expérimentale et théorique des liquides soumis aux seules forces moléculaires*, vol. 2. Gauthier-Villars, 1873.

[28] L. Rayleigh, "Xvi. on the instability of a cylinder of viscous liquid under capillary force," *The London, Edinburgh, and Dublin Philosophical Magazine and Journal of Science*, vol. 34, no. 207, pp. 145–154, 1892.

[29] C. Duprat, *Instabilités d'un film liquide en écoulement sur une fibre verticale.* PhD thesis, Université Pierre et Marie Curie-Paris VI, 2009.

[30] W. V. Kayser, "Temperature dependence of the surface tension of water in contact with its saturated vapor," *Journal of Colloid and Interface Science*, vol. 56, no. 3, pp. 622–627, 1976.

[31] S. Palmer, "The effect of temperature on surface tension," *Physics Education*, vol. 11, no. 2, p. 119, 1976.

[32] J. Pearson, "On convection cells induced by surface tension," *Journal of fluid mechanics*, vol. 4, no. 5, pp. 489–500, 1958.

[33] M. Gugliotti, M. S. Baptista, and M. J. Politi, "Surface tension gradients induced by temperature: The thermal marangoni effect," *Journal of chemical education*, vol. 81, no. 6, p. 824, 2004.

[34] Q. Magdelaine-Guillot de Suduiraut, *Hydrodynamique des films liquides hétérogènes.* PhD thesis, Sorbonne université, 2019.

[35] J. Eastoe and J. Dalton, "Dynamic surface tension and adsorption mechanisms of surfactants at the air–water interface," *Advances in colloid and interface science*, vol. 85, no. 2-3, pp. 103–144, 2000.

[36] Y. Marcus, "Surface tension of aqueous electrolytes and ions," *Journal of Chemical & Engineering Data*, vol. 55, no. 9, pp. 3641–3644, 2010.

[37] V. Soulié, *Sessile Droplets of Salt Solutions on Inert and Metallic Surfaces: Influence of Salt Concentration Gradients on Evaporation and Corrosion Behaviour.* PhD thesis, 2015.

[38] L. Tanner, "The spreading of silicone oil drops on horizontal surfaces," *Journal of Physics D: Applied Physics*, vol. 12, no. 9, p. 1473, 1979.

[39] D. Bonn, J. Eggers, J. Indekeu, J. Meunier, and E. Rolley, "Wetting and spreading," *Reviews of modern physics*, vol. 81, no. 2, p. 739, 2009.

[40] D. Brutin, *Droplet wetting and evaporation: from pure to complex fluids.* Academic Press, 2015.

[41] P.-G. De Gennes, "Wetting: statics and dynamics," *Reviews of modern physics*, vol. 57, no. 3, p. 827, 1985.

[42] W. Wirth, S. Storp, and W. Jacobsen, "Mechanisms controlling leaf retention of agricultural spray solutions," *Pesticide science*, vol. 33, no. 4, pp. 411–420, 1991.

[43] V. Bergeron, D. Bonn, J. Y. Martin, and L. Vovelle, "Controlling droplet deposition with polymer additives," *Nature*, vol. 405, no. 6788, pp. 772–775, 2000.

[44] H. Yoo and C. Kim, "Experimental studies on formation, spreading and drying of inkjet drop of colloidal suspensions," *Colloids and Surfaces A: Physicochemical and Engineering Aspects*, vol. 468, pp. 234–245, 2015.

[45] P. Kyaw Hla and S. Hogekamp, "Wetting behaviour of instantized cocoa beverage powders," *International journal of food science & technology*, vol. 34, no. 4, pp. 335–342, 1999.

[46] L. Forny, A. Marabi, and S. Palzer, "Wetting, disintegration and dissolution of agglomerated water soluble powders," *Powder technology*, vol. 206, no. 1-2, pp. 72–78, 2011.

[47] P. de Gennes, "Wetting: Statics and dynamics," *Simple Views on Condensed Matter*, pp. 357–394, 2003.

[48] C. Diddens, H. Tan, P. Lv, M. Versluis, J. Kuerten, X. Zhang, and D. Lohse, "Evaporating pure, binary and ternary droplets: thermal effects and axial symmetry breaking," *Journal of fluid mechanics*, vol. 823, pp. 470–497, 2017.

[49] T. Young, "Tr, an assay on the cohesion of fluids, philos," in *Soc. Lond*, vol. 95, pp. 65–87, 1805.

[50] R. Picknett and R. Bexon, "The evaporation of sessile or pendant drops in still air," *Journal of Colloid and Interface Science*, vol. 61, no. 2, pp. 336–350, 1977.

[51] A. Amini and G. Homsy, "Evaporation of liquid droplets on solid substrates. i. flat substrate with pinned or moving contact line," *Physical Review Fluids*, vol. 2, no. 4, p. 043603, 2017.

[52] J. M. Stauber, S. K. Wilson, B. R. Duffy, and K. Sefiane, "On the lifetimes of evaporating droplets with related initial and receding contact angles," *Physics of fluids*, vol. 27, no. 12, p. 122101, 2015.

[53] H. Y. Erbil, "Evaporation of pure liquid sessile and spherical suspended drops: A review," *Advances in colloid and interface science*, vol. 170, no. 1-2, pp. 67–86, 2012.

[54] A. J. D. Shaikeea, S. Basu, A. Tyagi, S. Sharma, R. Hans, and L. Bansal, "Universal representations of evaporation modes in sessile droplets," *PloS one*, vol. 12, no. 9, p. e0184997, 2017.

[55] S. Dash and S. V. Garimella, "Droplet evaporation on heated hydrophobic and superhydrophobic surfaces," *Physical Review E*, vol. 89, no. 4, p. 042402, 2014.

[56] H. Gelderblom, A. G. Marin, H. Nair, A. Van Houselt, L. Lefferts, J. H. Snoeijer, and D. Lohse, "How water droplets evaporate on a superhydrophobic substrate," *Physical Review E*, vol. 83, no. 2, p. 026306, 2011.

[57] K. Birdi and D. Vu, "Wettability and the evaporation rates of fluids from solid surfaces," *Journal of Adhesion Science and Technology*, vol. 7, pp. 485–493, Jan. 1993.

[58] C. Poulard, G. Guéna, and A. Cazabat, "Diffusion-driven evaporation of sessile drops," *Journal of Physics: Condensed Matter*, vol. 17, no. 49, p. S4213, 2005.

[59] J. F. Young, "Humidity control in the laboratory using salt solutions—a review," *Journal of Applied Chemistry*, vol. 17, no. 9, pp. 241–245, 1967.

[60] A. Fick, "Über diffusion ann," *Phys., Lpz*, vol. 23, p. 59, 1855.

[61] J. C. Maxwell, *Collected Scientific Papers. Vol. 2.* CUP, 1890.

[62] I. Langmuir, "The evaporation of small spheres," *Physical review*, vol. 12, no. 5, p. 368, 1918.

[63] F. Carle, *Flow motion in sessile droplets: evaporation and nanoparticles assembly.* PhD thesis, Aix-Marseille, 2014.

[64] H. Hu and R. G. Larson, "Analysis of the microfluid flow in an evaporating sessile droplet," *Langmuir*, vol. 21, no. 9, pp. 3963–3971, 2005.

[65] E. Widjaja and M. T. Harris, "Numerical study of vapor phase-diffusion driven sessile drop evaporation," *Computers & Chemical Engineering*, vol. 32, no. 10, pp. 2169–2178, 2008.

[66] D. B. Spalding, "Combustion of liquid fuels," *Nature*, vol. 165, no. 4187, pp. 160–160, 1950.

[67] M. Parsa, S. Harmand, and K. Sefiane, "Mechanisms of pattern formation from dried sessile drops," *Advances in colloid and interface science*, vol. 254, pp. 22–47, 2018.

[68] R. D. Deegan, O. Bakajin, T. F. Dupont, G. Huber, S. R. Nagel, and T. A. Witten, "Capillary flow as the cause of ring stains from dried liquid drops," *Nature*, vol. 389, no. 6653, pp. 827–829, 1997.

[69] J. Desarnaud, H. Derluyn, J. Carmeliet, D. Bonn, and N. Shahidzadeh, "Metastability limit for the nucleation of nacl crystals in confinement," *The journal of physical chemistry letters*, vol. 5, no. 5, pp. 890–895, 2014.

[70] R. M. Ginde and A. S. Myerson, "Effect of impurities on cluster growth and nucleation," *Journal of crystal growth*, vol. 126, no. 2-3, pp. 216–222, 1993.

[71] S. Popinet, "Gerris: a tree-based adaptive solver for the incompressible euler equations in complex geometries," *Journal of computational physics*, vol. 190, no. 2, pp. 572–600, 2003.

[72] R. Eymard, T. Gallouët, and R. Herbin, "Finite volume methods," *Handbook of numerical analysis*, vol. 7, pp. 713–1018, 2000.

[73] S. Popinet, "An accurate adaptive solver for surface-tension-driven interfacial flows," *Journal of Computational Physics*, vol. 228, no. 16, pp. 5838–5866, 2009.

[74] G. Tryggvason, R. Scardovelli, and S. Zaleski, *Direct numerical simulations of gas–liquid multiphase flows.* Cambridge University Press, 2011.

[75] https://www.comsol.fr/.

[76] N. D. Katopodes, "Chapter 13 - level set method," in *Free-Surface Flow* (N. D. Katopodes, ed.), pp. 804–828, Butterworth-Heinemann, 2019.

[77] R. Scardovelli and S. Zaleski, "Direct numerical simulation of free-surface and interfacial flow," *Annual review of fluid mechanics*, vol. 31, no. 1, pp. 567–603, 1999.

[78] S. Popinet, "Numerical models of surface tension," *Annual Review of Fluid Mechanics*, vol. 50, pp. 49–75, 2018.

[79] A. Berny, *Etude numérique de l'éclatement d'une bulle à la surface de différents liquides.* PhD thesis, Sorbonne Université, 2020.

[80] L. Scriven and C. Sternling, "The marangoni effects," *Nature*, vol. 187, no. 4733, pp. 186–188, 1960.

[81] N. A. Fuchs, *Evaporation and droplet growth in gaseous media*. Elsevier, 2013.

[82] L. Malan, "Direct numerical simulation of free-surface and interfacial flow using the vof method: cavitating bubble clouds and phase change," 2018.

[83] A. J. Chorin, "Numerical solution of the navier-stokes equations," *Mathematics of computation*, vol. 22, no. 104, pp. 745–762, 1968.

[84] J. B. Bell, P. Colella, and H. M. Glaz, "A second-order projection method for the incompressible navier-stokes equations," *Journal of computational physics*, vol. 85, no. 2, pp. 257–283, 1989.

[85] http://basilisk.fr/.

[86] Y. A. Çengel and J. M. Cimbala, *Mécanique des fluides*. De Boeck supérieur, 2017.

[87] https://www.w-tech.fr/fr/.

[88] H. Hu and R. G. Larson, "Evaporation of a sessile droplet on a substrate," *The Journal of Physical Chemistry B*, vol. 106, no. 6, pp. 1334–1344, 2002.

[89] R. D. Deegan, O. Bakajin, T. F. Dupont, G. Huber, S. R. Nagel, and T. A. Witten, "Contact line deposits in an evaporating drop," *Physical review E*, vol. 62, no. 1, p. 756, 2000.

[90] Y. O. Popov, "Evaporative deposition patterns: spatial dimensions of the deposit," *Physical Review E*, vol. 71, no. 3, p. 036313, 2005.

[91] F. Gibou, R. P. Fedkiw, L.-T. Cheng, and M. Kang, "A second-order-accurate symmetric discretization of the poisson equation on irregular domains," *Journal of Computational Physics*, vol. 176, no. 1, pp. 205–227, 2002.

[92] D. Q. Nguyen, R. P. Fedkiw, and M. Kang, "A boundary condition capturing method for incompressible flame discontinuities," *Journal of Computational Physics*, vol. 172, no. 1, pp. 71–98, 2001.

[93] M. Sagan, *Simulation numérique directe et étude expérimentale de l'ébullition nucléée en microgravité: application aux réservoirs des moteurs d'Ariane V*. PhD thesis, 2013.

[94] Y. Sato and B. Ničeno, "A sharp-interface phase change model for a mass-conservative interface tracking method," *Journal of Computational Physics*, vol. 249, pp. 127–161, 2013.

[95] G. Son and V. K. Dhir, "Numerical simulation of film boiling near critical pressures with a level set method," 1998.

[96] M. Sussman, P. Smereka, and S. Osher, "A level set approach for computing solutions to incompressible two-phase flow," *Journal of Computational physics*, vol. 114, no. 1, pp. 146–159, 1994.

[97] S. O. Unverdi and G. Tryggvason, "A front-tracking method for viscous, incompressible, multi-fluid flows," *Journal of computational physics*, vol. 100, no. 1, pp. 25–37, 1992.

[98] J. Schlottke and B. Weigand, "Direct numerical simulation of evaporating droplets," *Journal of Computational Physics*, vol. 227, no. 10, pp. 5215–5237, 2008.

[99] S. W. Welch and T. Rachidi, "Numerical computation of film boiling including conjugate heat transfer," *Numerical Heat Transfer: Part B: Fundamentals*, vol. 42, no. 1, pp. 35–53, 2002.

[100] S. W. Welch and J. Wilson, "A volume of fluid based method for fluid flows with phase change," *Journal of computational physics*, vol. 160, no. 2, pp. 662–682, 2000.

[101] C. Lalanne, Q. Magdelaine, F. Lequien, and J.-M. Fullana, "Numerical model using a volume-of-fluid method for the study of evaporating sessile droplets in both unpinned and pinned modes," *European Journal of Mechanics-B/Fluids*, 2021.

[102] S. Afkhami and M. Bussmann, "Height functions for applying contact angles to 2d vof simulations," *International journal for numerical methods in fluids*, vol. 57, no. 4, pp. 453–472, 2008.

[103] C. Poulard, *Dynamiques de gouttelettes mouillantes.* PhD thesis, Université Pierre et Marie Curie-Paris VI, 2005.

[104] N. Shahidzadeh-Bonn, S. Rafai, A. Azouni, and D. Bonn, "Evaporating droplets," *Journal of Fluid Mechanics*, vol. 549, pp. 307–313, 2006.

[105] H. Y. Erbil, G. McHale, and M. Newton, "Drop evaporation on solid surfaces: constant contact angle mode," *Langmuir*, vol. 18, no. 7, pp. 2636–2641, 2002.

[106] T. A. Nguyen, A. V. Nguyen, M. A. Hampton, Z. P. Xu, L. Huang, and V. Rudolph, "Theoretical and experimental analysis of droplet evaporation on solid surfaces," *Chemical engineering science*, vol. 69, no. 1, pp. 522–529, 2012.

[107] T. Lim, J. Yang, S. Lee, J. Chung, and D. Hong, "Deposit pattern of inkjet printed pico-liter droplet," *International Journal of Precision Engineering and Manufacturing*, vol. 13, no. 6, pp. 827–833, 2012.

[108] C. Bourges-Monnier and M. Shanahan, "Influence of evaporation on contact angle," *Langmuir*, vol. 11, no. 7, pp. 2820–2829, 1995.

[109] R. W. Coutant and E. C. Penski, "Experimental evaluation of mass transfer from sessile drops," *Industrial & Engineering Chemistry Fundamentals*, vol. 21, no. 3, pp. 250–254, 1982.

[110] S. M. Rowan, M. Newton, and G. McHale, "Evaporation of microdroplets and the wetting of solid surfaces," *The journal of physical chemistry*, vol. 99, no. 35, pp. 13268–13271, 1995.

[111] B. J. Fischer, "Particle convection in an evaporating colloidal droplet," *Langmuir*, vol. 18, no. 1, pp. 60–67, 2002.

[112] Y. Y. Tarasevich, "Simple analytical model of capillary flow in an evaporating sessile drop," *Physical Review E*, vol. 71, no. 2, p. 027301, 2005.

[113] C. Bouchenna, M. A. Saada, S. Chikh, and L. Tadrist, "Generalized formulation for evaporation rate and flow pattern prediction inside an evaporating pinned sessile drop," *International Journal of Heat and Mass Transfer*, vol. 109, pp. 482–500, 2017.

[114] N. Shahidzadeh, M. F. Schut, J. Desarnaud, M. Prat, and D. Bonn, "Salt stains from evaporating droplets," *Scientific reports*, vol. 5, no. 1, pp. 1–9, 2015.

[115] E. Guggenheim, "The theoretical basis of raoult's law," *Transactions of the Faraday Society*, vol. 33, pp. 151–156, 1937.

[116] S. A. McBride, S. Dash, and K. K. Varanasi, "Evaporative crystallization in drops on superhydrophobic and liquid-impregnated surfaces," *Langmuir*, vol. 34, no. 41, pp. 12350–12358, 2018.

[117] R. Gimenez, G. J. Soler-Illia, C. L. A. Berli, and M. G. Bellino, "Nanopore-enhanced drop evaporation: When cooler or more saline water droplets evaporate faster," *ACS nano*, vol. 14, no. 3, pp. 2702–2708, 2020.

[118] S. A. McBride, R. Skye, and K. K. Varanasi, "Differences between colloidal and crystalline evaporative deposits," *Langmuir*, vol. 36, no. 40, pp. 11732–11741, 2020.

[119] R. Van Hameren, P. Schön, A. M. Van Buul, J. Hoogboom, S. V. Lazarenko, J. W. Gerritsen, H. Engelkamp, P. C. Christianen, H. A. Heus, J. C. Maan, *et al.*, "Macroscopic hierarchical surface patterning of porphyrin trimers via self-assembly and dewetting," *Science*, vol. 314, no. 5804, pp. 1433–1436, 2006.

[120] N. Radacsi, R. Ambrus, T. Szunyogh, P. Szabo-Revesz, A. Stankiewicz, A. van der Heijden, and J. H. ter Horst, "Electrospray crystallization for nanosized pharmaceuticals with improved properties," *Crystal growth & design*, vol. 12, no. 7, pp. 3514–3520, 2012.

[121] Y. Tsutsumi, A. Nishikata, and T. Tsuru, "Initial stage of pitting corrosion of type 304 stainless steel under thin electrolyte layers containing chloride ions," *Journal of the Electrochemical Society*, vol. 152, no. 9, p. B358, 2005.

[122] H.-H. Strehblow, "Nucleation and repassivation of corrosion pits for pitting on iron and nickel," *Materials and Corrosion*, vol. 27, no. 11, pp. 792–799, 1976.

[123] R. D. Deegan, "Pattern formation in drying drops," *Physical review E*, vol. 61, no. 1, p. 475, 2000.

[124] M. Efstratiou, J. Christy, and K. Sefiane, "Crystallization-driven flows within evaporating aqueous saline droplets," *Langmuir*, vol. 36, no. 18, pp. 4995–5002, 2020.

[125] P. Takhistov and H.-C. Chang, "Complex stain morphologies," *Industrial & engineering chemistry research*, vol. 41, no. 25, pp. 6256–6269, 2002.

[126] R. M. Tona, T. A. McDonald, N. Akhavein, J. D. Larkin, and D. Lai, "Microfluidic droplet liquid reactors for active pharmaceutical ingredient crystallization by diffusion controlled solvent extraction," *Lab on a Chip*, vol. 19, no. 12, pp. 2127–2137, 2019.

[127] J. W. Mullin, *Crystallization*. Elsevier, 2001.

[128] Z. Wang, S. M. King, E. Freney, T. Rosenoern, M. L. Smith, Q. Chen, M. Kuwata, E. R. Lewis, U. Pöschl, W. Wang, *et al.*, "The dynamic shape factor of sodium chloride nanoparticles as regulated by drying rate," *Aerosol Science and Technology*, vol. 44, no. 11, pp. 939–953, 2010.

[129] A. G. Marin, H. Gelderblom, D. Lohse, and J. H. Snoeijer, "Order-to-disorder transition in ring-shaped colloidal stains," *Physical review letters*, vol. 107, no. 8, p. 085502, 2011.

[130] A. Darras, N. Vandewalle, and G. Lumay, "Transitional bulk-solutal marangoni instability in sessile drops," *Physical Review E*, vol. 98, no. 6, p. 062609, 2018.

[131] R. Bennacer and K. Sefiane, "Vortices, dissipation and flow transition in volatile binary drops," *Journal of fluid mechanics*, vol. 749, pp. 649–665, 2014.

[132] H. Hu and R. G. Larson, "Marangoni effect reverses coffee-ring depositions," *The Journal of Physical Chemistry B*, vol. 110, no. 14, pp. 7090–7094, 2006.

[133] V. Vitagliano and P. A. Lyons, "Diffusion coefficients for aqueous solutions of sodium chloride and barium chloride," *Journal of the American Chemical Society*, vol. 78, no. 8, pp. 1549–1552, 1956.

[134] J. Ren, X. Zhong, L. Shen, and F. Duan, "Hydrodynamic pattern in drying saline droplet with suspended nanoparticles," *Journal of Bionic Engineering*, vol. 17, no. 4, pp. 802–808, 2020.

[135] I. Seric, S. Afkhami, and L. Kondic, "Direct numerical simulation of variable surface tension flows using a volume-of-fluid method," *Journal of Computational Physics*, vol. 352, pp. 615–636, 2018.